Concentration Fluctuations and Phase Separations in Lipid Bilayers

Yuichi Hirose

A Thesis
for the Degree of Doctorate of Philosophy
Department of Chemistry
Tokyo Metropolitan University

2011

Abstract

In this thesis, we proposed a model for lipid bilayers, and discussed the mechanism of the finite-sized domain formation together with the effects of coupling of the two monolayers.

A lipid monolayer consisting of saturated lipid, hybrid lipid and cholesterol was considered. We proposed a phenomenological Ginzburg-Landau model in which the coupling of the lipid composition and chain orientational vector field is considered. This coupling arises from the liquid crystalline nature of the hybrid lipid which adjusts its orientational order in the tails to reduce the line tension. As a result, finite-sized domains can be formed. The minimization of the free energy with respect to the vector field yields an effective free energy which is analogous to that of 3D microemulsions (above the transition temperature) and modulated structures (below the transition temperature).

Then we considered the model for lipid bilayers comprised of two modulated monolayers which are coupled via interleaflet interactions. The structure and the dynamics of the coupled modulated bilayer are investigated theoretically.

We first studied concentration fluctuations in bilayers occurring above the transition temperature. We have calculated the static structure factors, and obtained the bilayer phase diagrams close to the critical temperature. In both monolayers, fluctuations are induced due to the coupling, and the spectrum of the induced fluctuations is determined by the cross correlation of the structure factor. When the two monolayers having different preferred wavenumbers are coupled, the peak height at smaller wavenumber becomes larger, whereas that at a larger wavenumber remains the same. We studied the dynam-

ics of concentration fluctuations by using the coupled time dependent Ginzburg-Landau equations, and calculated the intermediate structure factors of the bilayer. In general, concentration fluctuations exhibit a double-exponential decay. Due to the coupling, the time for the cross over of the two concentration fluctuations appears when the characteristic length scale of each monolayer is different.

Then we discussed the phase separation of the coupled modulated bilayers. Within the mean field approximation, we constructed phase diagrams of the bilayer when the two monolayers have the same wavenumber of the modulations. The phase behavior of the bilayers is described by the combinations of the stripe and the hexagonal morphologies. Due to the coupling effect, one of the monolayers induces micro-phase separation in the other monolayer. As the coupling strength increases, the asymmetric phases tend to disappear. By performing numerical simulations, we obtained various phase separated patterns when the two monolayers have different modulations. The obtained patterns are approximately classified into "independent", "intermediate" and "coincident" cases. The degree of the overlap between the two monolayers is characterized by the inter-leaflet correlation of the local compositions. We showed that the initial growth rates of the most unstable mode are essentially identical to the decay rates of the concentration fluctuations. We showed that the formation of the intermediate structures is related to the stability of the concentration fluctuations occurring above the transition temperature.

Using the mechanism of finite-sized domain formation proposed above, we shall also discuss its relation to the biologically relevant context of lipid rafts.

Contents

Chapter 1

Introduction

An amphiphilic molecule possesses both hydrophilic and hydrophobic moieties in a single molecule. The typical examples are surfactants, lipids and block copolymers. Due to hydrophobic interactions between the hydrocarbon chain and water molecules, these molecules self-assemble to form supermolecular structures in aqueous solutions as shown in Fig. 1.1. As the surfactant concentration is increased, micelles, bilayer vesicles, hexagonally packed cylinders, lamellae (which consist of stack of bilayers) and more complex cubic structures emerge due to the competition between entropy and intermolecular interactions [1].

The characteristic length scale of these mesoscopic structures is much larger than the molecular size and is typically $10 \sim 1000$ nm. The mesoscopic structures that are formed can be easily deformed upon the application of an external force. This is why amphiphilic systems are considered to be good examples of soft matter. The entropic modulus of a soft material is typically given by $G \sim k_{\mathrm{B}}T/d^3$, where k_{B} is the Boltzmann constant, T is the temperature and d is the characteristic length scale of the internal structure. Living matter is essentially soft matter in terms of its softness because the typical cell size is on the order of micron. Many researchers have been trying to clarify the border between living matter and soft matter. For example, the mechanics of the cell and its relations with the biochemical properties has attracted attention [2].

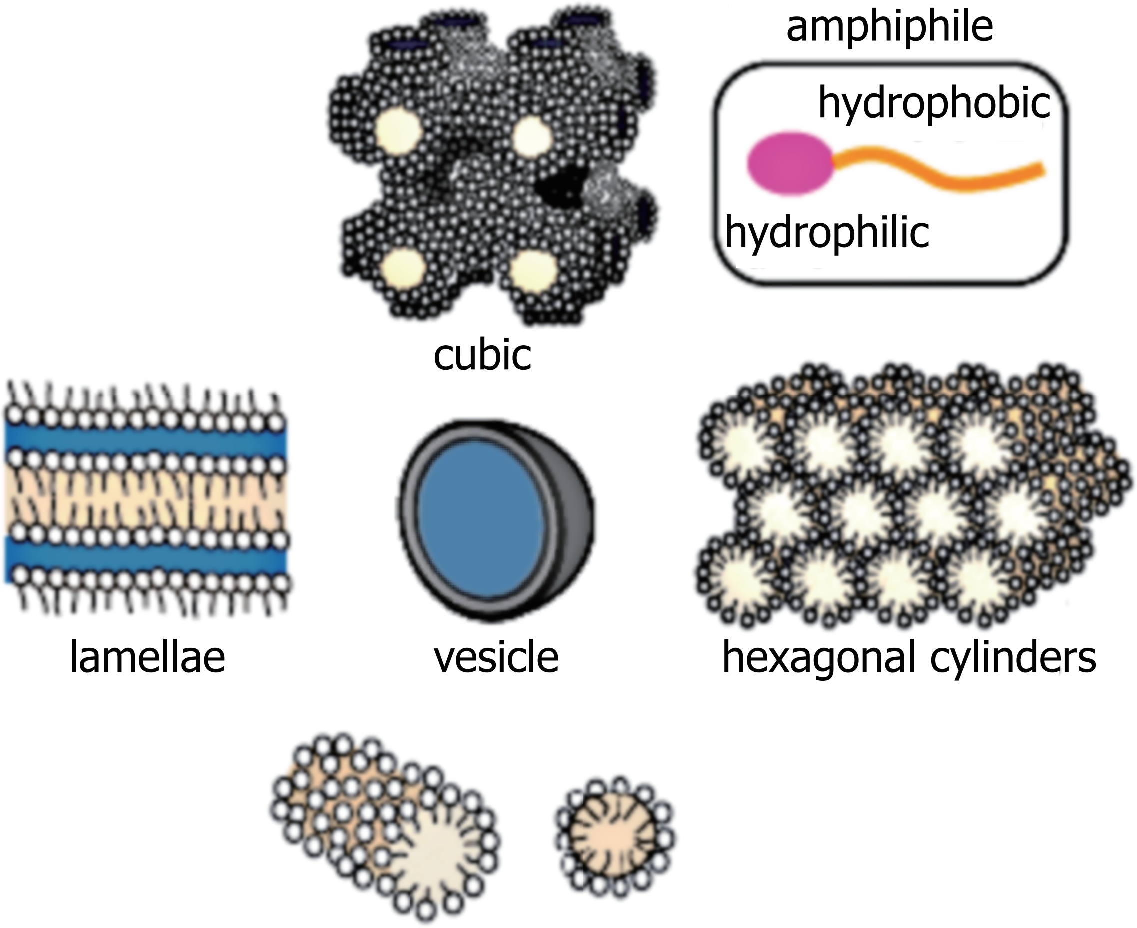

Figure 1.1: A schematic representation of an amphiphilic molecule and their organized structures in water solvent.

Biomembranes consist of thousands of lipid species forming bilayers and membrane proteins. As presented in Fig. 1.2(a), they separate inner and outer environment of the organelles in the cell. Membrane proteins are known to play essential roles for the biological functions. For example, they transduce external stimulation into chemical substances which are transmitted to internal environment of the cell. Such a process is called as signal transduction. Singer and Nicolson proposed the "fluid mosaic" model for biomembranes [3]. In this picture, membrane proteins are floating on the sea of lipids as schematically depicted in Fig. 1.2(b). Later, Simons and Ikonen proposed the "lipid raft" hypothesis in which some of the lipid components and/or proteins are incorporated into finite sized domains as shown in Fig. 1.2(c) [4]. Raft domains are expected to play important roles for the signal transduction processes by providing a field for the specific proteins to interact each other and increasing their efficiency.

Numerous studies have been conducted to identify the raft domains in biological membranes. For instance, detergent extraction of the membrane components from the cells was performed [5]. Although the detergent resistant membrane (DRM) fractions are considered as raft components, the extracts are not the representatives of the rafts because of the perturbation by the detergents and the low temperature (4 °C) of the process. Electron microscopic (EM) images of cell membranes were captured by labeling target lipids with gold nano particles of 10 nm size. A typical lipid cluster size was found to be about 10–100 nm [6, 7]. According to the fluorescence resonance energy transfer (FRET) study, the cluster size of GPI-anchored proteins was reported to be 4–5 nm [8]. Although the size and the existence of lipid rafts are still controversial, the former is expected to be in the range of 10–200 nm [9]. The interactions between lipid molecules and proteins are thought to be the driving force for the raft formation.

Among many studies, dynamics of a single lipid molecule in living cell membranes have been tracked using fluorescent microscopy, and the effect of cytoskeleton on the diffusion

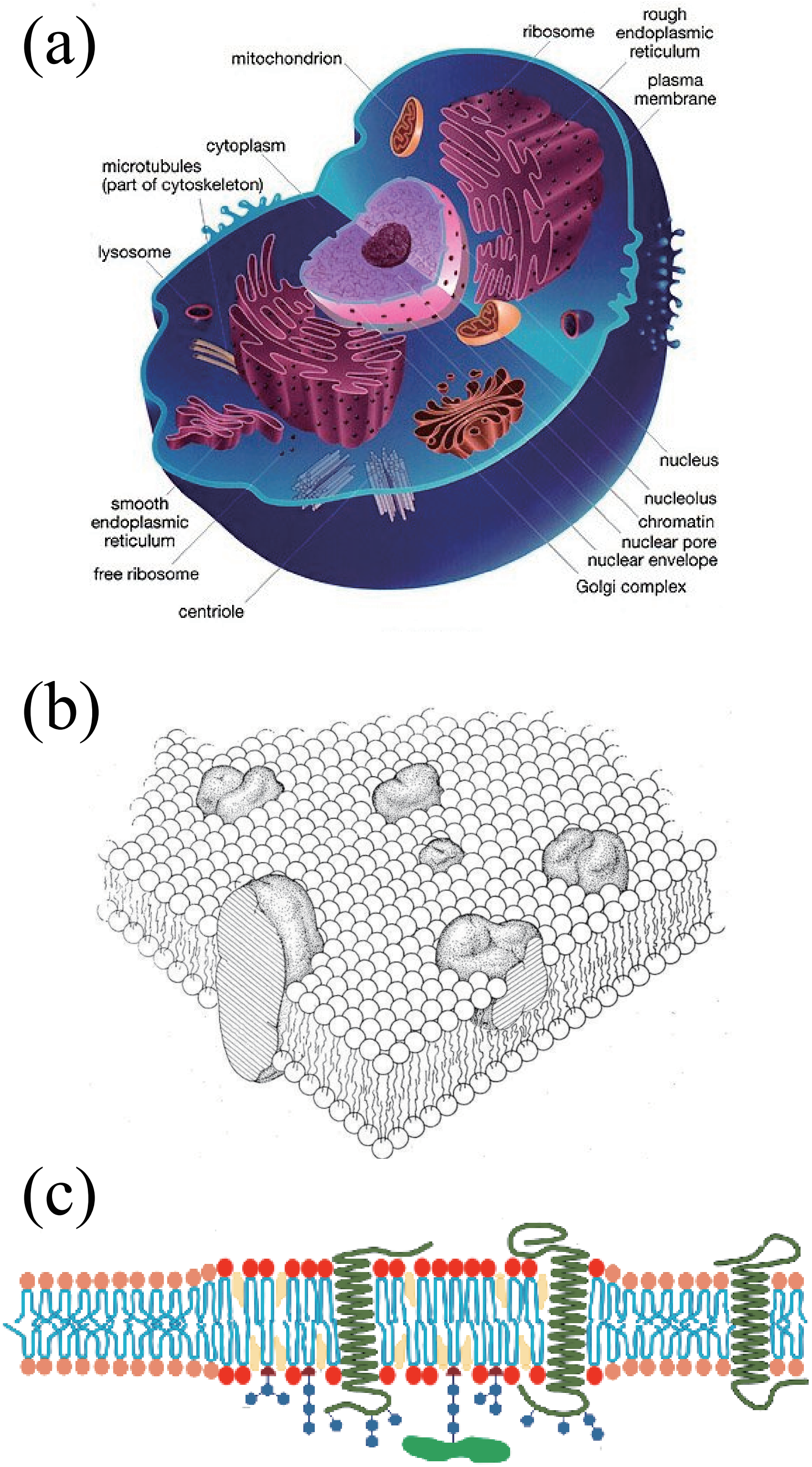

Figure 1.2: (a) A schematic representation of a single cell. There are many biomembranes inside the cell. Each internal organ has its own lipid membrane. (b) Fluid mosaic model of a biomembrane taken form the original paper [3]. The membrane proteins are embedded in the phospholipid bilayers. (c) A biomembrane with raft domains which are rich in certain components of the lipids and proteins.

of lipid molecules has been revealed [10]. Recently, high resolution observation of the lipid dynamics in living cells is achieved using stimulated emission depletion (STED) fluorescent microscopy [11]. They reported that sphingomyeline and membrane proteins are transiently (10-20 ms) trapped in 20 nm diameter areas. These experimental results suggest that lipid rafts are dynamical assemblies of molecules with finite decay time. In the latter study, the entrapment was not observed when the cholesterol is depleted from the membrane by the addition of cyclodextrin, suggesting the specific interactions with proteins or lipids on biomembranes.

In the area of "lipidomics", the main concern is to understand the functional specificity of lipids on various metabolic diseases such as obesity or diabetes [12]. The diversity in the lipid species (about one thousand) is expected to have some biological significance. However, domain formation in artificial membranes requires only three components; (i) saturated lipid having two saturated acyl chains, (ii) unsaturated lipid having one or more double bonds in one or both acyl chains, (iii) cholesterol having four cycloalkanes (see also Fig. 1.3). For both saturated and unsaturated lipids, the acyl chains are frozen in the low temperature (the gel phase denoted as S_{o} phase), and they are melted in the high temperature (the fluid phase denoted as L_{d} phase). This phase transition is called as the "main transition". The transition temperature of unsaturated lipids is generally lower than that of saturated lipids. This is because the double bonds introduce geometrical frustrations and act against the crystallization of the chains. Cholesterol interacts more favorably with saturated lipids than unsaturated lipids since the rigid structure of cholesterol fits well with saturated chains. The phase behavior of the membranes composed of these lipids is complex because of the interactions among them.

Many researches have been conducted to reveal the domain structures on artificial lipid membrane vesicles consisting of saturated lipid, unsaturated lipid and cholesterol (Fig. 1.3) [13, 14, 15, 16, 17]. When the membranes are below the transition temperature, micron sized domains can be observed using fluorescent microscopy. Domain formation is a consequence of the phase separation between the liquid ordered (L_{o}) phase and the liquid disordered (L_{d}) phase. The acyl chains are more ordered in the L_{o}-phase than in the L_{d}-phase, while the lateral mobility is much higher in the both phases compared to the S_{o}-phase. Such a demixing of lipids is caused by the difference in the packing nature of hydrophobic chains of saturated and unsaturated lipids. Without cholesterol, the phase separation between the S_{o}-phase and the L_{d}-phase is observed. The preferential affinity of cholesterol to the saturated lipids introduces more fluidity in the L_{o} phase. The effects of cholesterol on the phase behavior of lipid mixtures have been investigated theoretically such as using a phenomenological model [18], a microscopic model [19], or coarse grained simulations [20]. Typical size of the phase separated domains on artificial membranes is micron, and the domain growth continues until it reaches the size of the vesicle. In contrast to this, phase separated domains with distinct size (micron order) have been observed in artificial membranes [21, 22, 23, 24]. Although the characteristic size of the phase separated domains is different from that of the biomembranes, it is worthwhile to consider the formation mechanism of the finite sized domains on biomembranes in relation to the artificial membranes.

Another interesting research direction is to probe concentration fluctuations above the transition temperature in ternary lipid mixtures, as shown in Fig. 1.4 [25]. Analyzing fluorescent microscope images, the correlation length of critical concentration fluctuations in model membranes was measured [26, 27]. The obtained critical exponent characterizing the critical behavior of the correlation length suggests that these lipid mixtures belong to the universality class of 2D Ising model. Critical concentration fluctuations were also observed in membranes extracted from living cells [28]. It is rather surprising that plasma membranes may be naturally at their critical compositions considering the fact that they consist of thousands of different species of lipids and proteins.

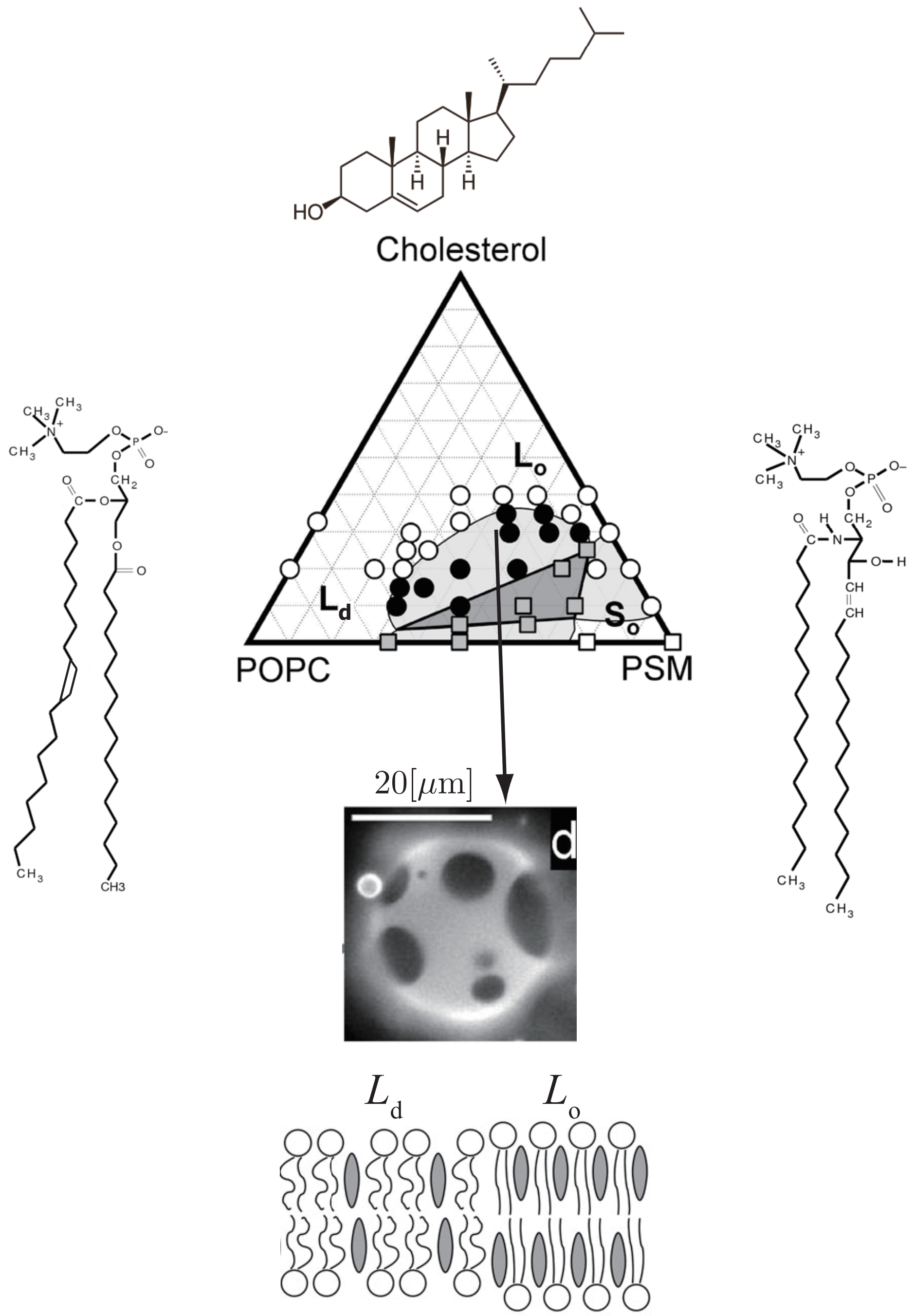

Figure 1.3: The phase diagram of the model membrane consisting of POPC (palmitoyloleoylphosphatidylcholine, unsaturated lipid), PSM (palmitoylsphingomyeline, saturated lipid) and cholesterol. The chemical structures of these molecules are illustrated. Phase separations occur in the light gray regions of the phase diagram with a typical microscope image of the phase separated structure. (The microscope picture is taken from the bilayer of DOPC/PSM/cholesterol.) Dark and bright domains in the micrograph are the liquid ordered (L_o) phase and the liquid disordered (L_d) phase, respectively. Cholesterol is preferentially partitioned in the L_o-phase than the L_d-phase. Figures are taken from Refs. [14, 38, 56].

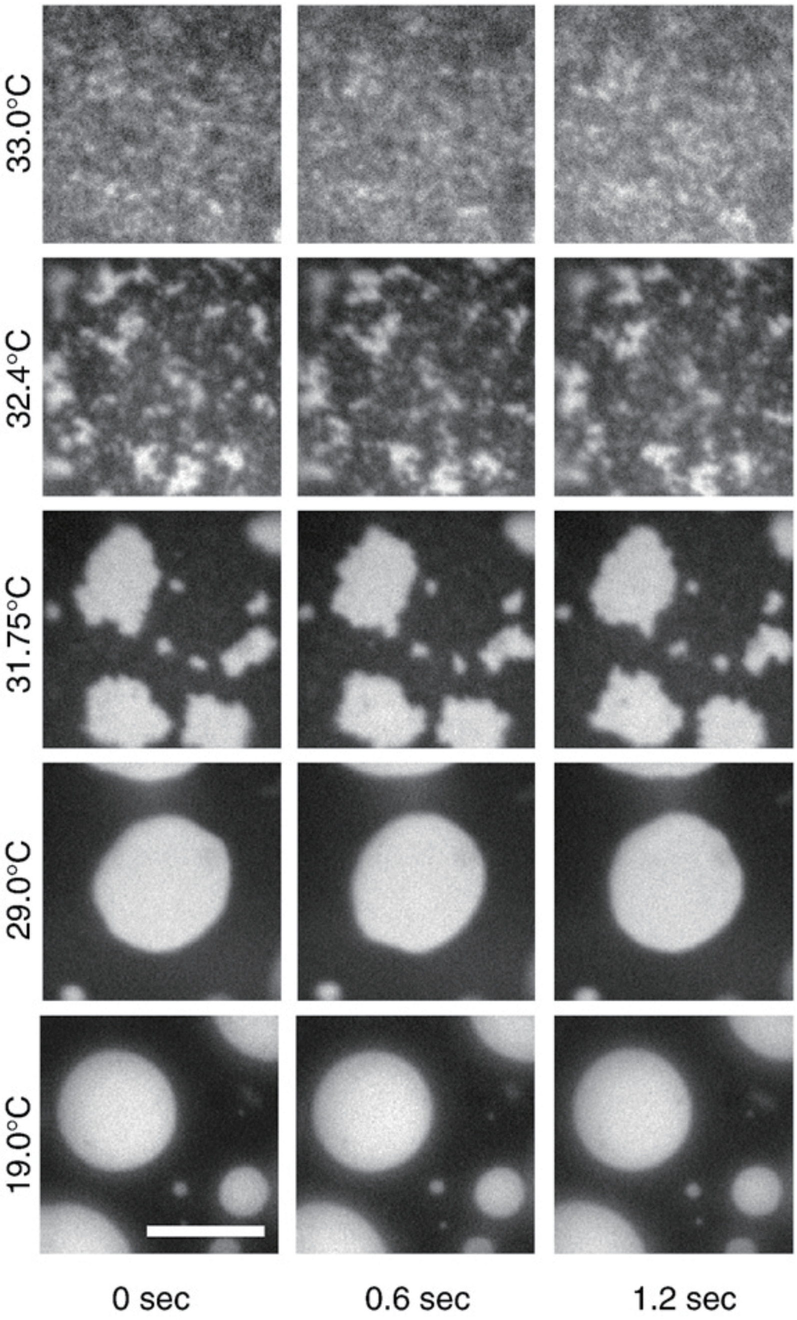

Figure 1.4: Fluorescent microscope images of the surface of a single giant unilamellar vesicle for different times [25]. The transition temperature is $T_c = 31.9$ °C. Concentration fluctuations can be observed when the temperature is higher than T_c. The vesicle is composed of 25:20:55 mol% of diphytanoylphosphatidylcholine (DiPhyPC), dipalmitoylphosphatidylcholine (DPPC) and cholesterol. The scale bar is $20\ \mu$m.

The key issue related to lipid rafts is to understand the existence of finite sized domains (clusters) rather than macroscopically phase separated domains. This question is primarily concerned with the question whether biomembranes are above or below the miscibility transition temperature. Suppose biomembranes are above the transition temperature, the correlation length characterizing the concentration fluctuations is the only length scale which diverges at the critical point. If biomembranes are below the transition temperature, there should be a mechanism to suppress the coarsening of domains. In this case, lipid membranes may undergo micro-phase separation similar to block copolymers. This naturally explains the typical length scale below the transition temperature in equilibrium.

One possibility to account for the finite sized domains in lipid membranes both above and below the transition temperature is the existence of “hybrid lipids” which have one saturated chain and one unsaturated chain [29, 30, 31]. Hybrid lipids are one type of unsaturated lipids, and are abundant in the biological membranes [32, 33]. Such lipids tend to localize at the 2D domain boundaries in order to reduce the frustration of the chain mismatch and act as line active molecules similar to the surfactant. As a result, hybrid lipids can drive the line tension to become negative. Hence a ternary mixture of saturated lipid (having two saturated chains), unsaturated lipid (having two unsaturated chains), and hybrid lipid has a close resemblance to a microemulsion consisting of oil, water, and surfactant [25, 29, 34]. It is known that three-dimensional (3D) microemulsions are thermodynamically stable solutions in which oil and water are isotropically mixed on the scale of 50–100 nm. Although the physical mechanisms for the stabilization of interfaces are different between surfactants and hybrid lipids, the ternary lipid mixtures can be regarded as 2D microemulsions. It was proposed that the hybrid lipid is a more efficient linactant in the mixture of saturated lipid, hybrid lipid, and cholesterol [31]. When the two chains of the hybrid lipid are oriented towards the domain interface, the line tension can become negative. The lipid domains generated in the membrane can then be termed as "2D micelles".

The important feature of biological membranes is that the lipid composition in each monolayer is notably different. For example, it was reported that the distribution of lipid species composing inner and outer leaflets in human red blood cells is asymmetric [35]. More importantly, these asymmetric monolayers are coupled and do not behave independently. The coupling of the domains in monolayers might be important because interleaflet interactions between proteins of outer and inner leaflets may connect the outer environments and inner signaling pathway of the cell. Such a coupling between the two leaflets was experimentally verified by looking at the phase behavior of combined monolayers which have different lipid compositions [36]. It was shown that one of the monolayers either induce or suppress phase separation in the other monolayer. One of the possibilities to account for this inter-monolayer coupling is the lipid chain interdigitation occurring at the mid-plane of the bilayer [37]. The phase behavior of the coupled lipid bilayer was theoretically studied using either the regular solution theory [38] or the Landau theory [39]. These works have been successful in describing the experimentally observed phase behaviors of coupled bilayers below the transition temperature. Later, concentration fluctuations of coupled bilayers above the transition temperature was investigated in Ref. [40].

In this thesis, the statics and dynamics of inhomogeneous structures in lipid bilayers are studied. We propose a model describing the formation of finite sized domains in membranes containing hybrid lipids. Within the Ginzburg-Landau theory, we consider a coupling between the chain orientation and the composition field in lipid monolayers. For both above and below the transition temperature, the characteristic length of the compositional modulations emerges due to the coupling. Such a characteristic length scale might possibly regulate the raft size in biomembranes. Especially, we discuss the concentration fluctuations above the transition temperature and their biological relevance. The decay time of the concentration fluctuations can be interpreted as a life time of dynamical domains. Then the effects of coupling of two modulated monolayers are considered by introducing interleaflet interactions as argued before [36, 38, 39]. We discuss both static and dynamic properties of concentration fluctuations in coupled modulated bilayers. We obtain the static and dynamical structure factors of coupled bilayers above the transition temperature. We construct the phase diagrams of the coupled modulated bilayers, and determine the regions of the ordered phase, the structured-disorder phase and the disorder phase in each monolayer. Due to the coupling between the two leaflets, concentration fluctuations are induced in both the monolayers. We especially focus on the case when the fluctuations in the two monolayers have different characteristic wavelengths. We also discuss the phase separation in the coupled modulated bilayers below the transition temperature. Various kinds of intermediate phase separated structures arise due to the two competing structures of different wavelengths. We show that the formation of the intermediate structures can be explained by the stability of the concentration fluctuations occurring above the transition temperature. Finally we discuss the biological relevance of the suggested model.

This thesis is organized as follows. In Chap. II, the model for modulated monolayers and coupled modulated bilayers are presented. The static and dynamical structure factors of the bilayers are computed in Chap. III. In Chap. IV, the phase behavior of the bilayer below the transition temperature is discussed. Some discussions are given in Chap. V. Finally, we conclude in Chap.VI.

Chapter 2

Model

In this chapter, we present models for a lipid monolayer and a bilayer. Firstly, a mechanism for the finite sized domain formation in lipid monolayers is discussed. The coupling between the concentration field of the lipids and the orientational vector field of lipid chains generates finite sized domain (modulated) structures in monolayers. Then we show a model for coupled bilayers which consist of two modulated monolayers. The physical origin of the inter-leaflet coupling is also discussed.

2.1 Lipid monolayer

As a model for the lipid monolayer, we consider a 2D lattice composed of saturated and hybrid lipids, and these lipids constitute the liquid ordered phase (L_{o}) and the liquid disordered phase (L_{d}), respectively (Fig. 2.1). Hybrid lipids possess both saturated chain

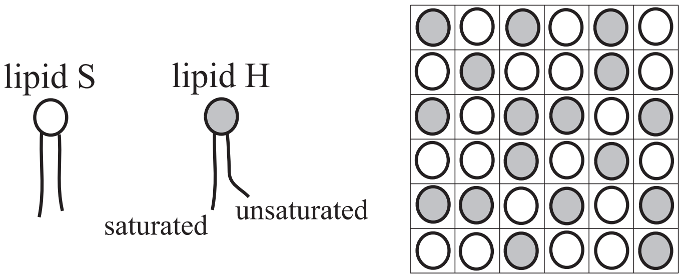

Figure 2.1: 2-dimensional lattice compose of saturated lipids and hybrid lipids. Hybrid lipids possess both saturated acyl chain and unsaturated acyl chain in a single molecule.

and unsaturated chain in a single molecule. We define the number of the lipid species as N_S and N_H. The Flory-Huggins free energy of mixing for the binary lipids per unit area is expressed as

$$\frac{f_0}{k_\mathrm{B}T} = \frac{1}{d^2}[\phi_\mathrm{S}\log\phi_\mathrm{S} + \phi_\mathrm{H}\log\phi_\mathrm{H} + \chi\phi_\mathrm{S}\phi_\mathrm{H}], \tag{2.1}$$

where $\phi_\mathrm{S} = N_\mathrm{S}/(N_\mathrm{S}+N_\mathrm{H})$ and $\phi_\mathrm{H} = N_\mathrm{H}/(N_\mathrm{S}+N_\mathrm{H})$ are the area fraction of each species, χ is the Flory-Huggins parameter, and d is the typical size of the lipid, such as the size of the head group. By defining $\phi = (\phi_\mathrm{S} - \phi_\mathrm{H})/2$ and using the incompressibility condition $\phi_\mathrm{S} + \phi_\mathrm{H} = 1$, Eq. (2.1) is expanded to give

$$\frac{f_0 - f_\mathrm{c}}{k_\mathrm{B}T} = \frac{\bar{\tau}}{2}\phi^2 + \frac{u}{4}\phi^4, \tag{2.2}$$

with

$$\bar{\tau} = \frac{2(2-\chi)}{d^2}, \tag{2.3}$$

and

$$u = \frac{16}{3d^2}. \tag{2.4}$$

Then the free energy is given by

$$F_\mathrm{c}[\phi(\tilde{\mathbf{r}})] = \int \mathrm{d}\tilde{\mathbf{r}} \left[\frac{\sigma}{2}(\tilde{\nabla}\phi)^2 + \frac{\bar{\tau}}{2}\phi^2 + \frac{u}{4}\phi^4 - \bar{\mu}\phi\right]. \tag{2.5}$$

Where $\tilde{\nabla} = (\partial/\partial\tilde{x}, \partial/\partial\tilde{y})$ and $\mathrm{d}\tilde{\mathbf{r}} = \mathrm{d}\tilde{x}\mathrm{d}\tilde{y}$, characters with tildes have the dimension of length. The term with $\sigma(>0)$ generates the energy penalty for spatially inhomogeneous distribution of ϕ, and is related to the line tension between two adjacent domains. $\bar{\mu}$ is the chemical potential which regulates the average composition in the membranes. This free energy describe the phase separation. When $\bar{\tau} < 0$, f_c has two minima at $\phi_{1,2} = \pm\sqrt{-\tau/u}$ (when spatially averaged composition ϕ_0 is zero), corresponding to the composition of L_o and L_d phases, respectively. The dynamics of the phase separation is described by the time evolution equations of the compositions

$$\frac{\partial\phi}{\partial t} = L_\phi\tilde{\nabla}^2\frac{\delta F_\mathrm{c}}{\delta\phi}, \tag{2.6}$$

where L_ϕ is the kinetic coefficient and $\delta F_{\mathrm{c}}/\delta\phi$ is the functional derivative. By solving the above equation, one can show that phase separated domains merge to grow in time driven by the penalty σ. The growth continues until the size of the domain reaches the "macroscopic" size (i.e., comparable to the system size). Thus there is no characteristic size of the domain for the phase separation phenomena.

We define the orientation of a hybrid lipid molecule as a vector from the unsaturated tail towards the saturated tail by $\mathbf{b} = (b_x, b_y)$ as shown in Fig. 2.2. The vector $\mathbf{m}(\tilde{\mathbf{r}}) = (m_x(\tilde{\mathbf{r}}), m_y(\tilde{\mathbf{r}}))$ is defined as the spatial average of the $\mathbf{b}$ vectors over areas large as compared with molecular size but still small enough as compared with macroscopic scales. The energy of these orientational vector is expressed by

$$F_{\mathrm{o}}[\mathbf{m}(\tilde{\mathbf{r}})] = \int \mathrm{d}\tilde{\mathbf{r}} \left[\frac{a}{2}\mathbf{m}^2 + \frac{K_1}{2}(\tilde{\nabla}\cdot\mathbf{m})^2 + \frac{K_2}{2}(\tilde{\nabla}\times\mathbf{m})^2 \right]. \tag{2.7}$$

The term of $a(>0)$ is related to the orientational entropy, and $K_1, K_2(>0)$ are the elastic constants for the orientation. Without the gradient terms, the above energy is minimized when the orientational field is $\mathbf{m} = 0$.

When the two lipid species are spatially inhomogeneous both above T_{c} (concentration fluctuations) and below T_{c} (phase separations), the coupling of the concentration and the orientational vector fields emerges. Here the coupling term is given by

$$F_{\mathrm{coup}}[\phi(\tilde{\mathbf{r}}), \mathbf{m}(\tilde{\mathbf{r}})] = -g \int \mathrm{d}\tilde{\mathbf{r}}\, \mathbf{m}\cdot(\tilde{\nabla}\phi), \tag{2.8}$$

where $g > 0$ is the coupling constant. Notice that this term is negative when $\mathbf{m}$ and $\tilde{\nabla}\phi$ point to the same direction. Hybrid lipids are responsible for the emergence of the coupling, because the saturated chain and the unsaturated chain of the lipid have preferences to the L_{o}-phase and the L_{d}-phase, respectively. Especially at the boundary between the L_{o} and the L_{d}-domains, the hybrid lipids are expected to reduce the chain mismatch by orienting their saturated/unsaturated chains toward the L_{o} and L_{d}-phases. The mechanism of chain direction alignment at the boundary was proposed by Yamamoto *et.al.* [31], and

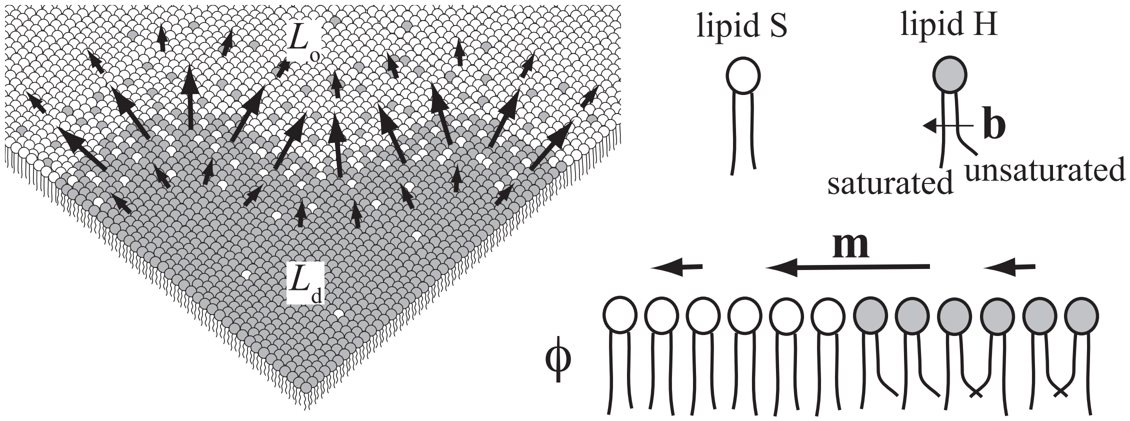

Figure 2.2: A lipid monolayer consisting of saturated lipids and hybrid lipids. The 2D vector of a lipid molecule from the less packing chain toward the packed chain is defined as $\mathbf{b}$. Spatially averaged orientational vector is defined as $\mathbf{m}$.

the mechanism we introduce here is a coarse grained and intuitive picture of this effect. The Ginzburg-Landau free energy functional for the lipid monolayers based on two order parameters $\phi(\tilde{\mathbf{r}})$ and $\mathbf{m}(\tilde{\mathbf{r}})$ is given by the sum of these contributions ($F_\mathrm{c} + F_\mathrm{o} + F_\mathrm{coup}$),

$$F_\mathrm{m}[\phi(\tilde{\mathbf{r}}), \mathbf{m}(\tilde{\mathbf{r}})] = \int \mathrm{d}\tilde{\mathbf{r}} \left[\frac{\sigma}{2}(\tilde{\nabla}\phi)^2 + \frac{\bar{\tau}}{2}\phi^2 + \frac{u}{4}\phi^4 - \bar{\mu}\phi \right.$$
$$\left. + \frac{a}{2}\mathbf{m}^2 + \frac{K_1}{2}(\tilde{\nabla}\cdot\mathbf{m})^2 + \frac{K_2}{2}(\tilde{\nabla}\times\mathbf{m})^2 - g\mathbf{m}\cdot(\tilde{\nabla}\phi) \right]. \tag{2.9}$$

In the Fourier space, $F_\mathrm{m}[\phi, \mathbf{m}]$ is expressed as

$$\begin{aligned} F_\mathrm{m}[\phi(\tilde{\mathbf{q}}), \mathbf{m}(\tilde{\mathbf{q}})] = \int \mathrm{d}\tilde{\mathbf{q}} \Bigg[& \frac{1}{2}\left(\sigma\tilde{q}^2 + \bar{\tau}\right)\phi(\tilde{\mathbf{q}})\phi(-\tilde{\mathbf{q}}) \\ & + \frac{1}{2}\left(a - K_1\tilde{q}_x^2 - K_2\tilde{q}_y^2\right) m_x(\tilde{\mathbf{q}})m_x(-\tilde{\mathbf{q}}) \\ & + \frac{1}{2}\left(a - K_1\tilde{q}_y^2 - K_2\tilde{q}_x^2\right) m_y(\tilde{\mathbf{q}})m_y(-\tilde{\mathbf{q}}) \\ & - (K_1 + K_2)\tilde{q}_x\tilde{q}_y m_x(\tilde{\mathbf{q}})m_y(-\tilde{\mathbf{q}}) \\ & + ig[\tilde{q}_x m_x(\tilde{\mathbf{q}})\phi(-\tilde{\mathbf{q}}) + \tilde{q}_y m_y(\tilde{\mathbf{q}})\phi(-\tilde{\mathbf{q}})] \Bigg] - \bar{\mu}\phi(\mathbf{0}) \\ + \int \mathrm{d}\tilde{\mathbf{q}} \int \mathrm{d}\tilde{\mathbf{q}}' \int \mathrm{d}\tilde{\mathbf{q}}'' & \left[\frac{u}{4}\phi(\tilde{\mathbf{q}})\phi(\tilde{\mathbf{q}}')\phi(\tilde{\mathbf{q}}'')\phi(-\tilde{\mathbf{q}} - \tilde{\mathbf{q}}' - \tilde{\mathbf{q}}'') \right], \end{aligned} \tag{2.10}$$

where i is the imaginary unit, $\tilde{\mathbf{q}} = (\tilde{q}_x, \tilde{q}_y)$ is the wavevector in the monolayer, and $\tilde{q} = |\tilde{\mathbf{q}}|$ is the wavenumber. Minimizing $F_\mathrm{m}[\phi(\tilde{\mathbf{q}}), \mathbf{m}(\tilde{\mathbf{q}})]$ with respect to $\mathbf{m}(\tilde{\mathbf{q}})$ yields the equilibrium orientational fields of the chains for each Fourier mode as,

$$\mathbf{m}^*(\tilde{\mathbf{q}}) = \frac{ig\tilde{q}}{a + K_1\tilde{q}^2}\phi(\tilde{\mathbf{q}}). \tag{2.11}$$

Note that the constant K_2 vanishes in this minimization process. By putting Eq. (2.11), the free energy depends only on the composition,

$$\begin{aligned} F_{\mathrm{m}}[\phi(\tilde{\mathbf{q}})] = &\int \mathrm{d}\tilde{\mathbf{q}}\left(\frac{\sigma}{2}\tilde{q}^2 + \frac{\bar{\tau}}{2} - \frac{g^2\tilde{q}^2}{2(a + K_1\tilde{q}^2)}\right)\phi(\tilde{\mathbf{q}})\phi(-\tilde{\mathbf{q}}) - \bar{\mu}\phi(\mathbf{0}) \\ &+ \int \mathrm{d}\tilde{\mathbf{q}} \int \mathrm{d}\tilde{\mathbf{q}}' \int \mathrm{d}\tilde{\mathbf{q}}'' \left[\frac{u}{4}\phi(\tilde{\mathbf{q}})\phi(\tilde{\mathbf{q}}')\phi(\tilde{\mathbf{q}}'')\phi(-\tilde{\mathbf{q}} - \tilde{\mathbf{q}}' - \tilde{\mathbf{q}}'')\right]. \end{aligned} \tag{2.12}$$

Again, the constant K_2 does not appear in the minimized energy. For small q, the coefficients of the coupling term can be expanded, and the free energy is given by

$$\begin{aligned} F_{\mathrm{m}}[\phi(\tilde{\mathbf{q}})] = &\int \mathrm{d}\tilde{\mathbf{q}}\left(2B\tilde{q}^4 - 2A\tilde{q}^2 + \frac{\bar{\tau}}{2}\right)\phi(\tilde{\mathbf{q}})\phi(-\tilde{\mathbf{q}}) - \bar{\mu}\phi(\mathbf{0}) \\ &+ \int \mathrm{d}\tilde{\mathbf{q}} \int \mathrm{d}\tilde{\mathbf{q}}' \int \mathrm{d}\tilde{\mathbf{q}}'' \left[\frac{u}{4}\phi(\tilde{\mathbf{q}})\phi(\tilde{\mathbf{q}}')\phi(\tilde{\mathbf{q}}'')\phi(-\tilde{\mathbf{q}} - \tilde{\mathbf{q}}' - \tilde{\mathbf{q}}'')\right], \end{aligned} \tag{2.13}$$

with

$$\tilde{B} = \frac{K_1 g^2}{4a^2}, \tag{2.14}$$

and

$$A = \frac{1}{4}\left(\frac{g^2}{a} - \sigma\right). \tag{2.15}$$

Notice that A is dimensionless quantity. The wavenumber $\tilde{q}$-dependence of the free energy $F_{\mathrm{m}}[\phi(\tilde{\mathbf{q}})]$ is plotted in Fig. 2.3. When the coupling is weak ($g^2/a - \sigma < 0$), the line tension has a positive value ($A < 0$) and the minimum is at $\tilde{q}^* = 0$, indicating the macro-phase separation (below T_{c}). If the coupling is strong ($g^2/a - \sigma > 0$), the line tension can become negative ($A > 0$) and the energy has a minimum at $\tilde{q}^* \neq 0$. The negative gradient squared term favors spatial modulations, whereas the positive coefficients of the Laplacian squared term ($\tilde{B} > 0$) suppresses modulations. As a result of these contributions, a stable modulation of finite wavenumber emerges. The characteristic wavenumber of this

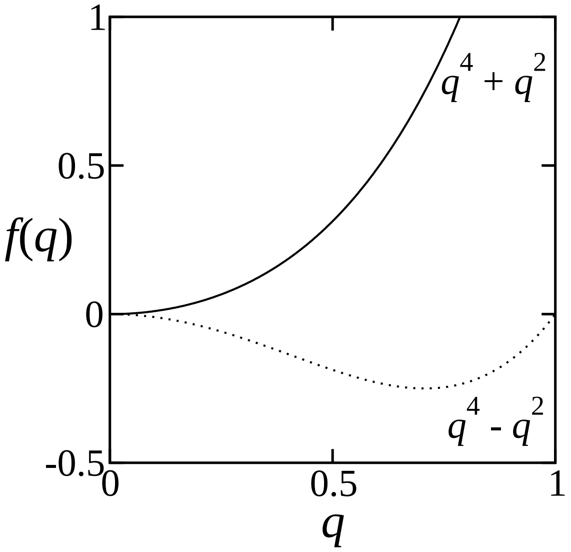

Figure 2.3: Wavenumber q dependence of the free energy.

modulated structure is obtained by minimizing Eq. (2.13) with respect to $\tilde{q}$

$$\tilde{q}^* = \sqrt{\frac{A}{2\tilde{B}}} = \sqrt{\frac{a(1 - a\sigma/g^2)}{2K_1}}. \tag{2.16}$$

Here the length scale of the modulation is determined by a, the line tension σ, the elastic coefficient K_1, and the coupling constant g. These coefficients are related to the properties of the lipid mixture.

In real space, Eq. (2.13) is expressed as

$$F_{\mathrm{m}}[\phi(\mathbf{r})] = \int \mathrm{d}\mathbf{r} \left[2B(\nabla^2\phi)^2 - 2A(\nabla\phi)^2 + \frac{\tau}{2}\phi^2 + \frac{1}{4}\phi^4 - \mu\phi \right], \tag{2.17}$$

Here $\mathbf{r} = u\tilde{\mathbf{r}}$ and $\nabla = \tilde{\nabla}/\sqrt{u}$ are the dimensionless area and Laplacian, respectively. $B = u\tilde{B}$, $\tau = \bar{\tau}/u$, and $\mu = \bar{\mu}/u$ are the dimensionless quantities. Equation (2.17) has been used successfully in the past to describe a variety of modulated systems: magnetic garnet films [41], Langmuir films [42], lipid membranes [43] and diblock copolymers [44, 45]. This free energy functional also describes the structure of 3D microemulsions [46, 47]. It should be noted that the free energy functional of Eq. (2.9) was proposed in order to explain the phase behavior of the 3D microemulsion systems [48]. In magnetic garnet films, modulated structures appear as a competition between the domain wall energy (favoring large domain) and the demagnetizing energy (dipolar interactions which favoring small domain) energy. In the case of Langumuir films, a balance between the line tension (favoring large domain) and the dipolar electrostatic repulsion (favoring small domain) generates modulations. In lipid membranes, the coupling of lipid composition and curvature of the membranes generates the modulated structures [21, 22, 23, 24]. In our model of lipid monolayers, a competition between the negative line tension (favoring small domain) and the elastic energy (favoring large domain) generates modulations. All of these modulated structures emerge as a balance between short and long range interactions. In the next subsection, we present the model for lipid bilayers in which two modulated monolayers are coupled each other.

2.2 Lipid bilayer

In order to illustrate the coupling effect between two modulated monolayers, we consider a pair of lipid monolayers forming a coupled bilayer. Each of the monolayer have finite sized modulations due to the above mentioned mechanism. As shown in Fig. 2.4, we assume the other monolayer is also a mixture of lipid S and lipid H. Area fractions of lipids in the other monolayer is defined by $\psi_{\mathrm{S}}(\mathbf{r})$ and $\psi_{\mathrm{H}}(\mathbf{r})$. Assuming that the monolayer is incompressible $\psi_{\mathrm{S}}(\mathbf{r}) + \psi_{\mathrm{H}}(\mathbf{r}) = 1$, order parameter of the lower monolayer is defined by $\psi(\mathbf{r}) = \psi_{\mathrm{S}}(\mathbf{r}) - \psi_{\mathrm{H}}(\mathbf{r})$. The coarse-grained free-energy functional for the coupled modulated bilayer is written as:

$$F_{\mathrm{b}}[\phi, \psi] = \int \mathrm{d}\mathbf{r} \bigg[2B(\nabla^2\phi)^2 - 2A(\nabla\phi)^2 + \frac{\tau_\phi}{2}\phi^2 + \frac{1}{4}\phi^4 - \mu_\phi\phi \\ + 2D(\nabla^2\psi)^2 - 2C(\nabla\psi)^2 + \frac{\tau_\psi}{2}\psi^2 + \frac{1}{4}\psi^4 - \mu_\psi\psi - \Lambda\phi\psi \bigg]. \qquad (2.18)$$

This is a modified dimensionless Ginzburg-Landau free energy expanded in powers of the order parameters ϕ and ψ and their derivatives. The first five terms depend only

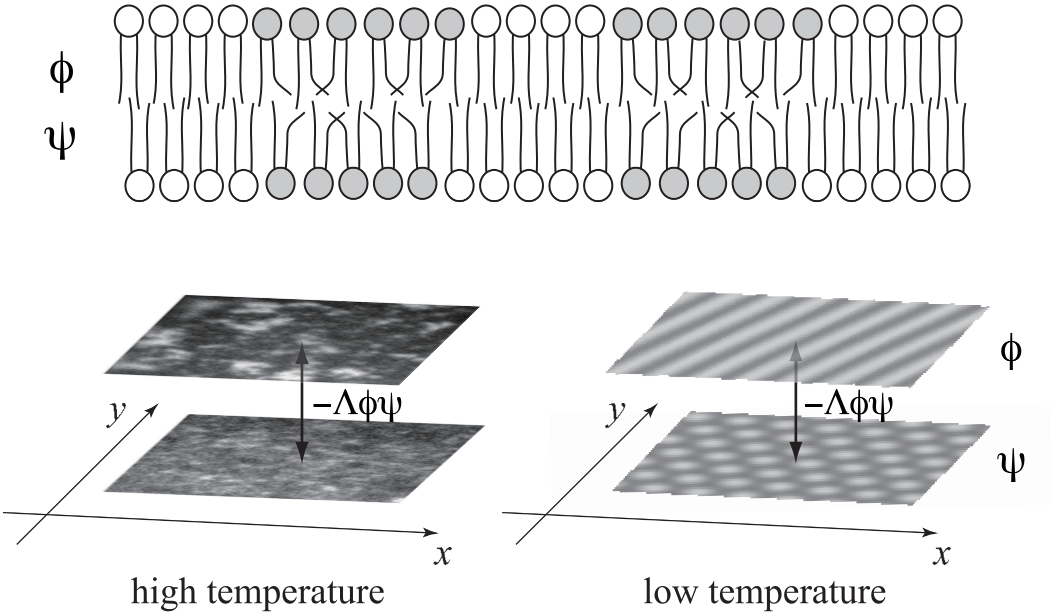

Figure 2.4: Schematic illustration of two coupled modulated monolayers forming a bilayer membrane. Each monolayer is composed of a binary S/H lipid mixture, which can have a spatial modulation. The relative composition of lipids of S and H in the upper and the lower leaflets are defined by ϕ and ψ, respectively. In general, the average composition in the two monolayers can be different. The lipid tails interact across the bilayer mid-plane. The phenomenological coupling term between these two variables are assumed to be bi-linear of the form $-\Lambda\phi\psi$ in the free energy of Eq. (2.18).

on ϕ and its derivatives and describe the upper monolayer and its possible modulations. Similarly, the next five terms that are only functions of ψ and its derivatives describing the lower monolayer. The last term represents the coupling between the two leaflets. The coefficients of the gradient squared and the Laplacian squared terms (C, D) are related to the properties of the lower monolayer. The ϕ^2, ϕ^4, ψ^2 and ψ^4 terms in $F_{\rm b}$ are the usual Landau expansion terms with τ_ϕ and τ_ψ being the scaled temperatures. Finally, the linear term coefficients, μ_ϕ and μ_ψ are the scaled chemical potentials.

Here we address the physical origin of the coupling term. We first note that this quadratic term is invariant under the exchange of $\phi \leftrightarrow \psi$. When $\Lambda > 0$, this term can be obtained from a $(\phi - \psi)^2$ term [38, 39], which represents a local energy penalty when the upper and lower monolayers have different compositions. In the case of mixed lipid bilayers, such a coupling may result from the conformational confinement of the lipid chains, and hence would have entropic origin [38]. By estimating the degree of the lipid chain interdigitation, the magnitude of the coupling parameter Λ was estimated by May [37]. In general, the coupling constant Λ can also be negative depending on the specific coupling mechanism [37]. However, it will be explained later that the phase diagram for $\Lambda < 0$ can easily be obtained from the $\Lambda > 0$ one. Hence, it is sufficient to consider only the $\Lambda > 0$ case without loss of generality. The case when the other coupling terms including non-local coupling between the monolayers is discussed in Appendix A.

Chapter 3

Concentration Fluctuations

In this chapter, we consider concentration fluctuations in modulated bilayers occurring above the critical temperature. We obtain analytical expressions for the static structure factors, the phase diagrams, and the intermediate structure factors of the coupled modulated bilayers.

3.1 Statics

We write the order parameters ϕ and ψ as

$$\phi = \phi_0 + \delta\phi, \qquad \psi = \psi_0 + \delta\psi, \tag{3.1}$$

where $\phi_0 = \langle \phi \rangle$ and $\psi_0 = \langle \psi \rangle$ are the spatially averaged compositions in each monolayer, and $\delta\phi$ and $\delta\psi$ describe the deviations of the composition from their average values. In equilibrium, the average compositions satisfy the following conditions

$$\tau_\phi \phi_0 + \phi_0^3 - \mu_\phi - \Lambda \psi_0 = 0, \tag{3.2}$$

$$\tau_\psi \psi_0 + \psi_0^3 - \mu_\psi - \Lambda \phi_0 = 0. \tag{3.3}$$

Inserting Eq. (3.1) to Eq. (2.18) and leaving only up to quadratic terms in $\delta\phi$ and $\delta\psi$, we obtain the Gaussian free energy

$$\begin{aligned}F_{\mathrm{G}}[\delta\phi,\delta\psi] = \int \mathrm{d}\mathbf{r}\Bigg[&2B(\nabla^2\delta\phi)^2 - 2A(\nabla\delta\phi)^2 + \frac{\tilde{\tau}_\phi}{2}(\delta\phi)^2 \\ &+2D(\nabla^2\delta\psi)^2 - 2C(\nabla\delta\psi)^2 + \frac{\tilde{\tau}_\psi}{2}(\delta\psi)^2 - \Lambda(\delta\phi)(\delta\psi)\Bigg], \end{aligned} \tag{3.4}$$

where we have used the notations $\tilde{\tau}_\phi = \tau_\phi + 3\phi_0^2$ and $\tilde{\tau}_\psi = \tau_\psi + 3\psi_0^2$.

The above free energy can be expressed in Fourier space. For this purpose, we first define the Fourier coefficients of $\delta\phi$ and $\delta\psi$ by $\delta\phi(\mathbf{q})$ and $\delta\psi(\mathbf{q})$, respectively, i.e.,

$$\delta\phi(\mathbf{q}) = \int \mathrm{d}\mathbf{r}\,\delta\phi(\mathbf{r}\,)\exp(-i\mathbf{q}\cdot\mathbf{r}\,), \tag{3.5}$$

$$\delta\psi(\mathbf{q}) = \int \mathrm{d}\mathbf{r}\,\delta\psi(\mathbf{r}\,)\exp(-i\mathbf{q}\cdot\mathbf{r}\,). \tag{3.6}$$

Then Eq. (3.4) becomes

$$F_{\mathrm{G}}[\delta\phi(\mathbf{q}),\delta\psi(\mathbf{q})] = \frac{1}{2}\int \mathrm{d}\mathbf{q}\left[\begin{array}{cc}\delta\phi(-\mathbf{q}) & \delta\psi(-\mathbf{q})\end{array}\right] S^{-1}(\mathbf{q})\left[\begin{array}{c}\delta\phi(\mathbf{q})\\ \delta\psi(\mathbf{q})\end{array}\right], \tag{3.7}$$

where

$$S^{-1}(\mathbf{q}) = \left[\begin{array}{cc}2\Gamma_\phi(q) & -\Lambda \\ -\Lambda & 2\Gamma_\psi(q)\end{array}\right], \tag{3.8}$$

with

$$\begin{aligned}\Gamma_\phi(q) &= 2Bq^4 - 2Aq^2 + \frac{\tilde{\tau}_\phi}{2}, \\ \Gamma_\psi(q) &= 2Dq^4 - 2Cq^2 + \frac{\tilde{\tau}_\psi}{2}.\end{aligned} \tag{3.9}$$

Note that $q = |\mathbf{q}|$.

The inverse matrix of Eq. (3.8) gives the structure factor matrix $S(\mathbf{q})$

$$S(\mathbf{q}) = \left[\begin{array}{cc}S_{\phi\phi}(\mathbf{q}) & S_{\phi\psi}(\mathbf{q}) \\ S_{\psi\phi}(\mathbf{q}) & S_{\psi\psi}(\mathbf{q})\end{array}\right], \tag{3.10}$$

in which the partial structure factors $S_{\phi\phi}(\mathbf{q})$, $S_{\phi\psi}(\mathbf{q})$, $S_{\psi\phi}(\mathbf{q})$, $S_{\psi\psi}(\mathbf{q})$ are defined by

$$S_{\phi\phi}(\mathbf{q}) = \langle\delta\phi(\mathbf{q})\delta\phi(-\mathbf{q})\rangle, \tag{3.11}$$

$$S_{\psi\psi}(\mathbf{q}) = \langle \delta\psi(\mathbf{q})\delta\psi(-\mathbf{q})\rangle, \tag{3.12}$$

$$S_{\phi\psi}(\mathbf{q}) = S_{\psi\phi}(\mathbf{q}) = \langle \delta\phi(\mathbf{q})\delta\psi(-\mathbf{q})\rangle = \langle \delta\psi(\mathbf{q})\delta\phi(-\mathbf{q})\rangle. \tag{3.13}$$

After some calculations, we obtain

$$S_{\phi\phi}(\mathbf{q}) = \frac{2\Gamma_\psi(q)}{4\Gamma_\phi(q)\Gamma_\psi(q) - \Lambda^2}, \tag{3.14}$$

$$S_{\psi\psi}(\mathbf{q}) = \frac{2\Gamma_\phi(q)}{4\Gamma_\phi(q)\Gamma_\psi(q) - \Lambda^2}, \tag{3.15}$$

$$S_{\phi\psi}(\mathbf{q}) = \frac{\Lambda}{4\Gamma_\phi(q)\Gamma_\psi(q) - \Lambda^2}. \tag{3.16}$$

We can see that the coupling parameter Λ effectively changes the critical temperature. The total structure factor is given by

$$S_{\text{tot}}(\mathbf{q}) = S_{\phi\phi}(\mathbf{q}) + S_{\psi\psi}(\mathbf{q}) + 2S_{\phi\psi}(\mathbf{q}) = \frac{2(\Gamma_\phi(q) + \Gamma_\psi(q) + \Lambda)}{4\Gamma_\phi(q)\Gamma_\psi(q) - \Lambda^2}. \tag{3.17}$$

The thermodynamic compressibility is obtained by taking the limit of $q \to 0$ for each partial structure factor. Then we obtain

$$\kappa_{\phi\phi} = S_{\phi\phi}(q \to 0) = \frac{\tilde{\tau}_\psi}{\tilde{\tau}_\phi\tilde{\tau}_\psi - \Lambda^2}, \tag{3.18}$$

$$\kappa_{\psi\psi} = S_{\psi\psi}(q \to 0) = \frac{\tilde{\tau}_\phi}{\tilde{\tau}_\phi\tilde{\tau}_\psi - \Lambda^2}, \tag{3.19}$$

$$\kappa_{\phi\psi} = \kappa_{\phi\psi} = S_{\phi\psi}(q \to 0) = S_{\phi\psi}(q \to 0) = \frac{\Lambda}{\tilde{\tau}_\phi\tilde{\tau}_\psi - \Lambda^2}. \tag{3.20}$$

For the total compressibility, we get

$$\kappa_{\text{tot}} = S_{\text{tot}}(q \to 0) = \frac{\tilde{\tau}_\phi + \tilde{\tau}_\psi + 2\Lambda}{\tilde{\tau}_\phi\tilde{\tau}_\psi - \Lambda^2}. \tag{3.21}$$

3.1.1 Decoupled case ($\Lambda = 0$)

We first discuss the case when the two monolayers are decoupled, i.e, $\Lambda = 0$. Then the structure factors are simply given by

$$S_\phi(\mathbf{q}) = 1/2\Gamma_\phi(q), \qquad S_\psi(\mathbf{q}) = 1/2\Gamma_\psi(q). \tag{3.22}$$

These functions exhibit peaks at $q_\phi^* = \sqrt{A/2B}(A > 0)$ and $q_\psi^* = \sqrt{C/2D}(C > 0)$, indicating that fluctuations characterized by the corresponding length scales dominantly exist in each monolayer in thermal equilibrium. The peak intensities in the respective monolayer is $S_\phi(q = q_\phi^*) = 1/(\tilde{\tau}_\phi - A^2/B)$ and $S_\psi(q = q_\psi^*) = 1/(\tilde{\tau}_\psi - C^2/D)$, hence the critical temperatures are given as $\tilde{\tau}_\phi^* = A^2/B$ and $\tilde{\tau}_\psi^* = C^2/D$, respectively.

The 2D inverse Fourier transform of Eq. (3.22) yields the real space correlation functions (see Appendix B for the derivation)

$$G_\phi(r) = \frac{\xi_\phi \lambda_\phi}{32\pi B} \mathrm{Re}\left[H_0^{(1)}\left(\frac{2\pi r}{\lambda_\phi} + i\frac{r}{\xi_\phi} \right) \right], \tag{3.23}$$

$$G_\psi(r) = \frac{\xi_\psi \lambda_\psi}{32\pi D} \mathrm{Re}\left[H_0^{(1)}\left(\frac{2\pi r}{\lambda_\psi} + i\frac{r}{\xi_\psi} \right) \right], \tag{3.24}$$

where $H_0^{(1)}$ is the Hankel function of first kind. Each correlation function contains two length scales; the first one being the alternation period

$$\frac{\lambda_\phi}{2\pi} = \left(\frac{B}{\tilde{\tau}_\phi}\right)^{1/4} \frac{2}{\sqrt{1-\gamma_\phi}}, \qquad \frac{\lambda_\psi}{2\pi} = \left(\frac{D}{\tilde{\tau}_\psi}\right)^{1/4} \frac{2}{\sqrt{1-\gamma_\psi}}, \tag{3.25}$$

and the other being the correlation length

$$\xi_\phi = \left(\frac{B}{\tilde{\tau}_\phi}\right)^{1/4} \frac{2}{\sqrt{1+\gamma_\phi}}, \qquad \xi_\psi = \left(\frac{D}{\tilde{\tau}_\psi}\right)^{1/4} \frac{2}{\sqrt{1+\gamma_\psi}}. \tag{3.26}$$

Here we have used the notations $\gamma_\phi = -A/\sqrt{\tilde{\tau}_\phi B}$, $\gamma_\psi = -C/\sqrt{\tilde{\tau}_\psi D}$.

In Fig. 3.1(a), we plot the correlation function Eq. (3.23) for various parameters. Similar to 3D microemulsions [46], the correlation of concentration fluctuation oscillates and decays exponentially as a function of the distance r. When $-1 \le \gamma_\phi \le 1$, both λ_ϕ and ξ_ϕ are finite, and the corresponding phase is called the structured-disorder phase. In this phase, the line of $\gamma_\phi = 0$ is called the Lifshitz line. The peak position of the structure factor is $q_\phi^* \neq 0$ for $-1 \le \gamma_\phi \le 0$, whereas it is at $q_\phi^* = 0$ for $0 \le \gamma_\phi \le 1$.The periodicity λ_ϕ diverges when $\gamma_\phi \to 1$, and the system is in the disorder phase when $\gamma_\phi \ge 1$. The line for $\gamma_\phi = 1$ is called the disorder line. The correlation length ξ_ϕ diverges when $\gamma_\phi \to -1$ (hence the critical point), and the ordered phase appears for $\gamma_\phi \leq -1$.Figure 3.1(b) summarizes the phase behavior of a decoupled monolayer in terms of the parameter γ_ϕ.

The above arguments are equivalent to analyzing poles of Eq. (3.22) in a complex plane (see Appendix B for details). All the poles are real numbers when $\gamma_\phi \leq -1$ so that λ_ϕ is finite in the ordered phase. Since all the poles are complex number when $-1 \leq \gamma_\phi \leq 1$, both λ_ϕ and ξ_ϕ are finite in the structured-disorder phase. All the poles are pure imaginary numbers when $\gamma_\phi \geq 1$, and only ξ_ϕ is finite in the disorder phase.

The phase diagram of the decoupled bilayer is easily obtained from Fig. 3.1(b) by combining its two cross-sections (one for γ_ϕ and one for γ_ψ), and shown in Fig. 3.2(a). All the phases are expressed as combinations of the ordered phase (O), the structured-disorder phase (S) and the disorder phase (D). Lifshitz lines are also shown using dotted lines.

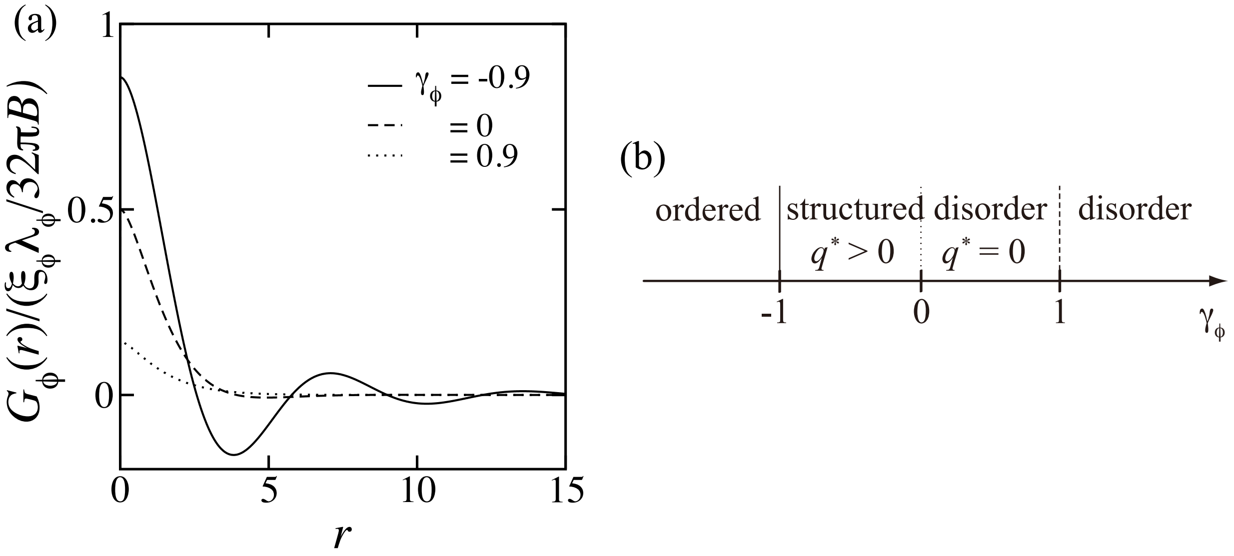

Figure 3.1: (a) Real space correlation function of monolayers in the structured disorder phase as a function of r with various parameters. (b) Phase diagram of the modulated monolayer, where $\gamma_\phi = -A/\sqrt{B\tilde{\tau}_\phi}$. Depending on the value of the γ_ϕ, the states of the monolayer is categorized as the ordered phase, the structured disorder phase or the disorder phase. Lifshitz line is located at $\gamma_\phi = 0$.

3.1.2 Coupled case ($\Lambda \neq 0$)

When the two monolayers are coupled ($\Lambda \neq 0$), the corresponding phase diagram can be obtained by analyzing poles of the following quantity (the denominator of the structure factors of the coupled bilayer)

$$S_{\mathrm{d}} = \frac{1}{(q^4 + 2\gamma_\phi\sqrt{\tilde{\tau}_\phi/4B}q^2 + \tilde{\tau}_\phi/4B)(q^4 + 2\gamma_\psi\sqrt{\tilde{\tau}_\psi/4D}q^2 + \tilde{\tau}_\psi/4D) - \Lambda^2/(16BD)}, \tag{3.27}$$

and one example is shown in Fig. 3.2(b).

The boundary between the OO and SS phases is determined by the condition that the structure factor diverges. In the region assigned as the DD phase, all the poles of Eq. (3.27) are pure imaginary numbers. There are complex poles in the SS phase, while there is at least one real pole in the OO phase. We can see that the asymmetric phases like "SD" and "DO" have disappeared. As it will be explained later in the part of the static structure factors, one monolayer induces modulations to the other monolayer due to the coupling, and the regions of the OO and SS phases are expanded, while the DD phase region becomes smaller. Notice that increasing the coupling is equivalent to lowering the temperature, since our coupling term is quadratic in terms of the compositions ($-\Lambda\phi\psi$). The Lifshitz lines corresponding to each monolayer are numerically obtained by detecting the peak positions of Eqs. (3.14) and (3.15). The dashed dot lines close to the phase boundaries are the equimaxima lines [49]. On these lines, the peak heights in one monolayer at $q = 0$ and at $q \neq 0$ induced by the other monolayer are the same.

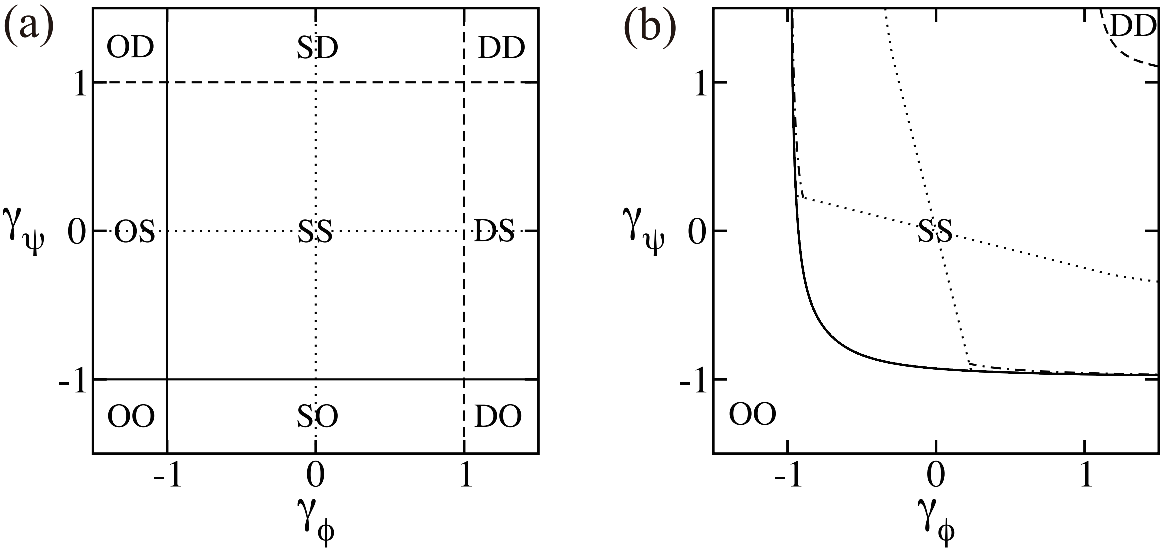

Figure 3.2: Phase diagram of the bilayer around the critical temperature for $\tilde{\tau}_\phi/4B = \tilde{\tau}_\psi/4D = 1$. All the phases are expressed as the combination of two characters, each of them represents phases in ϕ- and ψ-monolayer. "O", "S" and "D" stand for the ordered phase, structured disorder phase and disorder phase, respectively. Solid, broken and dotted lines are the transition, disorder and Lifshitz lines respectively. (a) Phase diagram of decoupled bilayer ($\Lambda = 0$) and (b) finite coupling ($\Lambda/\sqrt{BD} = 2$), $\gamma_\phi = -A/(\sqrt{B\tilde{\tau}_\phi})$, $\gamma_\psi = -C/(\sqrt{D\tilde{\tau}_\psi})$. The broken dotted lines are the equimaxima lines. Lifshitz and equimaxima lines in (b) are drawn under the condition of $B = D = 0.5$.

In Fig. 3.3(a) and (b), we plot the structure factors of the decoupled ($\Lambda = 0$) and the coupled ($\Lambda = 0.4$) bilayers, respectively. Here we consider the case when the two characteristic wavelengths are different, i.e., $q^*_\phi \neq q^*_\psi$. In order to have the better comparison, the intensities of the two peaks are set to be equal, according to the condition $A^2/B = C^2/D = 1$. For the coupled case, we can see that the fluctuations are induced in both of the monolayers. The structure factor $S_{\phi\psi}$ expresses the cross correlation of the two monolayers as shown in Eq. (3.16). This quantity is related to the induced fluctuations due to the coupling. We see that the peak height reflecting that of $S_{\phi\phi}$ at $q = 1/\sqrt{2}$ is increased in $S_{\phi\phi}$, whereas the peak height reflecting that of $S_{\psi\psi}$ at $q = 3/\sqrt{2}$ is nearly unchanged compared with the decoupled case. The peak position of $S_{\phi\psi}$ is nearly located at that of $S_{\phi\phi}$. The position of the peak in $S_{\phi\psi}$ is determined by the product of the S_ϕ and S_ψ. Notice that the structure factor of the modulated monolayers decays as q^{-4} for $q \gg q^*$. Then $S_{\psi\psi}(q < q^*_\psi)$ has relatively large value and $S_{\phi\phi}(q > q^*_\phi)$ is small (see Fig. 3.3(a)), and the cross correlation of the two structure factors $S_{\phi\psi}$ is large for $q \sim q^*_\phi$ and small for $q \sim q^*_\psi$. Notice that the such a tendency of the induced fluctuations due to the coupling is strong when the wavenumber ratio q^*_ψ/q^*_ϕ is different from unity. This is the direct consequence of the asymmetry of the two peak positions in the modulated bilayers. Similar phenomena should occur not only for the coupled lipid membrane system but also for other coupled modulated systems, e.g., coupled magnetic films with different lengths of the modulation.

In Figs. 3.4, 3.5, 3.6, we plot the structure factors in the case when the temperatures of the monolayers are different ($\tilde{\tau}_\phi \neq \tilde{\tau}_\psi$). In Fig. 3.4, we show the case when the monolayer which is characterized by a larger wavenumber has lower temperature ($q^*_\psi/q^*_\phi = 3$, $\tilde{\tau}_\phi = 1.5, \tilde{\tau}_\psi = 1.2$). In the decoupled case (a), we can see that the peak height $S_{\psi\psi}(q = q^*_\psi)$ is larger than that of the Fig. 3.3(a) because the temperature is close to the critical point. The coupled case is shown in Fig. 3.4(b). The structure factors at the peak position $q = q^*_\psi$

do not change, whereas the peak at $q = q^*_\phi$ is induced to the both of the monolayers. In Fig. 3.5, we show the case when the monolayer which is characterized by a smaller wavenumber has lower temperature ($q^*_\psi/q^*_\phi = 3$, $\tilde{\tau}_\phi = 1.2, \tilde{\tau}_\psi = 1.5$). The decoupled case and the coupled case are shown in (a) and (b). The increase of the structure factor due to the coupling at the peak position $S_{\phi\phi}(q = q^*_\phi)$ is larger than that of the Fig. 3.4(b). In Fig. 3.6, we show the case when the monolayer which is characterized by a larger wavenumber is close to the critical temperature ($q^*_\psi/q^*_\phi = 3$, $\tilde{\tau}_\phi = 1.5, \tilde{\tau}_\psi = 1.01$). The cross correlation $S_{\phi\psi}$ exhibits a peak at $q = q^*_\psi$, but its value is still smaller than that of the peak at $q = q^*_\phi$. In the limit of $\tilde{\tau}_\psi \to 1$, the peak value of $q = q^*_\psi$ becomes larger than that of the $q = q^*_\phi$ and the bilayer state changes to the ordered phase. These results show that the induction of the fluctuations at smaller wavenumber occurs even when the temperatures of each monolayer are different.

In Fig. 3.7, the numerically obtained peak positions of the cross of structure factor $S_{\phi\psi}$ denoted as $q^*_{\phi\psi}$ are shown. In all the temperature cases, we can see that peak positions do not depend on the coupling constant Λ. For all the wavenumber ratios, the values of the $q_{\phi\psi}$ have almost same values with the peak wavenumber of the smaller ones ($q = 1/\sqrt{2}$). In the case when one of the monolayers has lower temperature (b and c), the lines of $q^*_\phi = q^*_\psi = 1/\sqrt{2}$ have endpoints. The endpoints represent the transition point to the ordered phase. As we will discuss later, the coupling change the transition lines.

The peak position of $S_{\phi\psi}$ denoted as $q^*_{\phi\psi}$ is numerically obtained and plotted in Fig. 3.8(a) as a function of q^*_ϕ and q^*_ψ. Here the two peak heights are same $S_\phi(q = q^*_\phi) = S_\psi(q = q^*_\psi)$ under the condition $A^2/B = C^2/D = 1$. We see that when the fluctuations of different characteristic wavenumbers are coupled, the value of $q^*_{\phi\psi}$ is almost equal to that of the smaller one. As the characteristic wavenumbers are increased ($q^*_\phi \sim q^*_\psi \sim 2$), the contour lines of $q^*_{\phi\psi}$ are no longer parallel to the axes. This is because of the large overlap of the structure factors of the two monolayers. Notice that the width of the peak in the

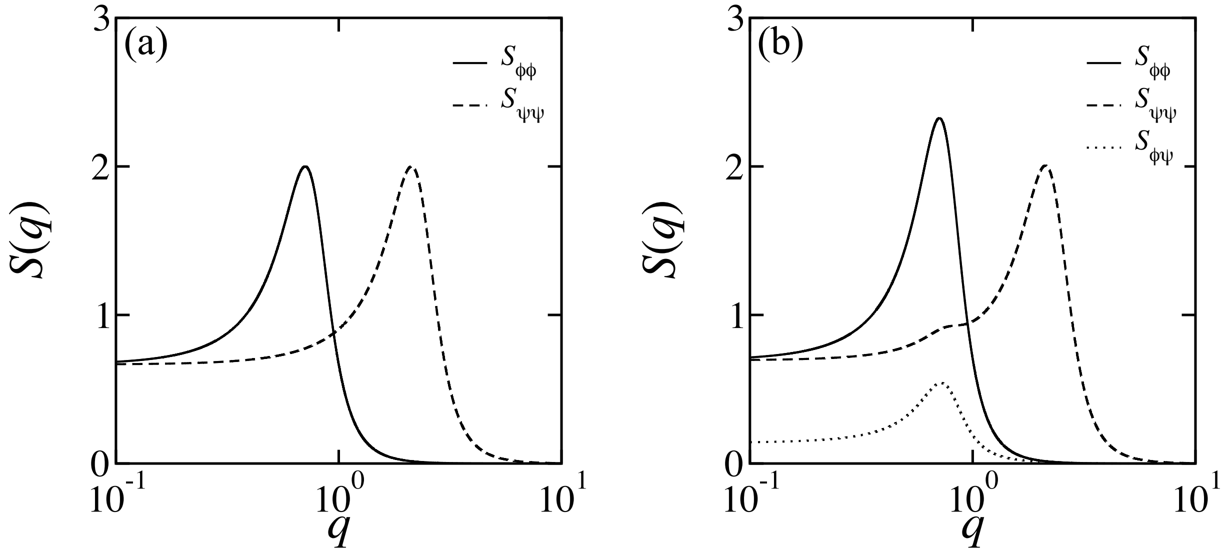

Figure 3.3: Static structure factors of the bilayer $S_{\phi\phi}$, $S_{\psi\psi}$, $S_{\phi\psi}$ for $\tilde{\tau}_\phi = \tilde{\tau}_\psi = 1.5$, $B = A = 1$, $D = 0.0123$, $C = 0.1111$ $(q^*_\phi = 1/\sqrt{2}, q^*_\psi = 3/\sqrt{2})$. (a) $\Lambda = 0$, (b) $\Lambda = 0.3$.

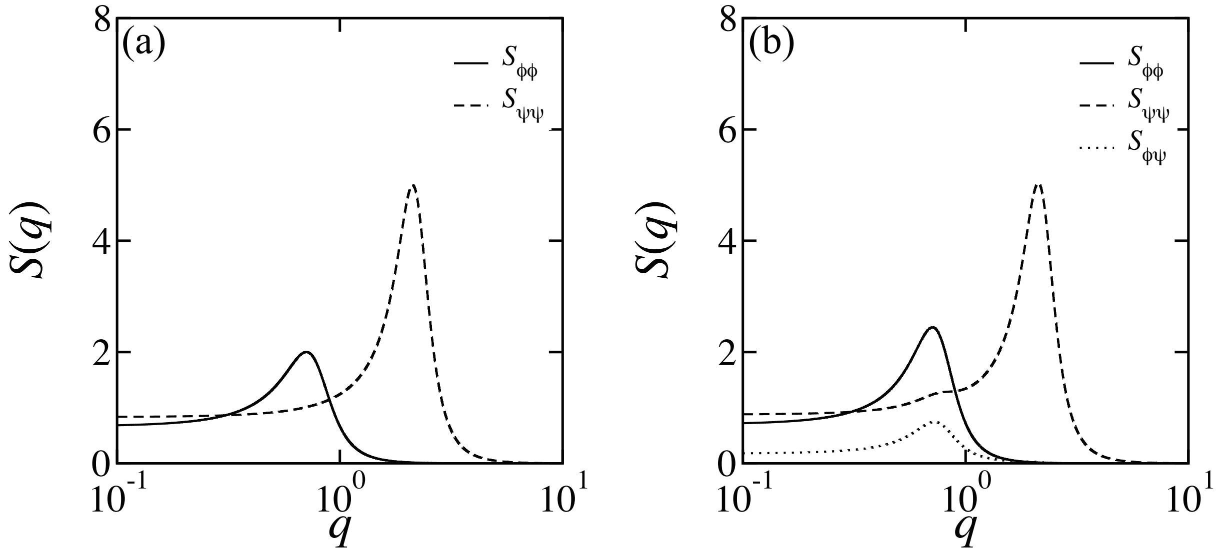

Figure 3.4: Static structure factors of the bilayer $S_{\phi\phi}$, $S_{\psi\psi}$, $S_{\phi\psi}$ for $\tilde{\tau}_\phi = 1.5, \tilde{\tau}_\psi = 1.2$, $B = A = 1$, $D = 0.0123$, $C = 0.1111$ $(q^*_\phi = 1/\sqrt{2}, q^*_\psi = 3/\sqrt{2})$. (a) $\Lambda = 0$, (b) $\Lambda = 0.3$.

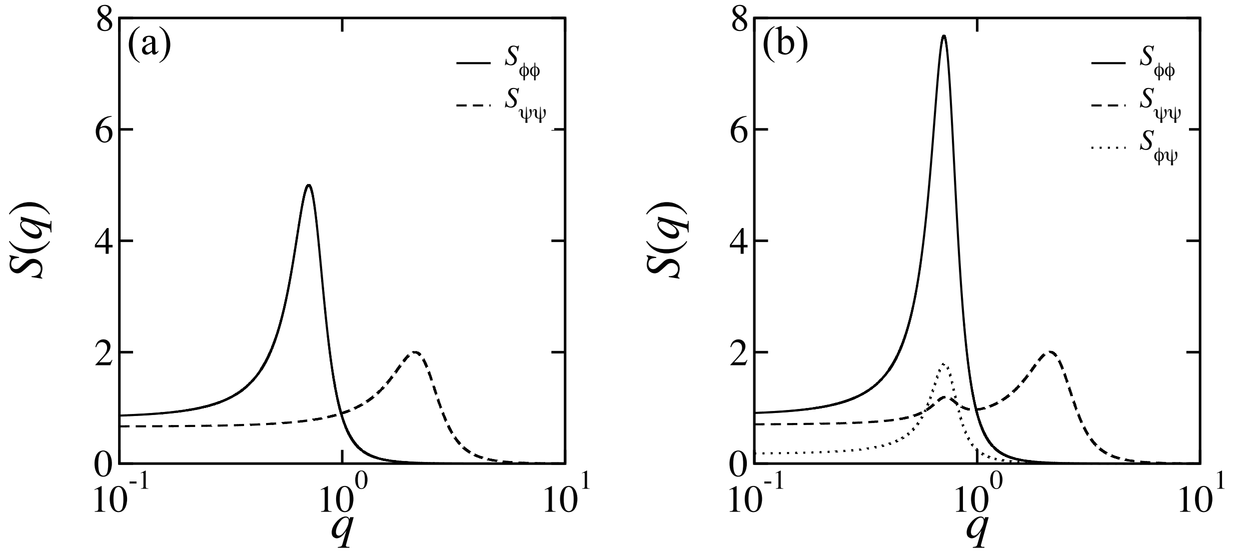

Figure 3.5: Static structure factors of the bilayer $S_{\phi\phi}$, $S_{\psi\psi}$, $S_{\phi\psi}$ for $\tilde{\tau}_\phi = 1.2, \tilde{\tau}_\psi = 1.5$, $B = A = 1$, $D = 0.0123$, $C = 0.1111$ $(q^*_\phi = 1/\sqrt{2}, q^*_\psi = 3/\sqrt{2})$. (a) $\Lambda = 0$, (b) $\Lambda = 0.3$.

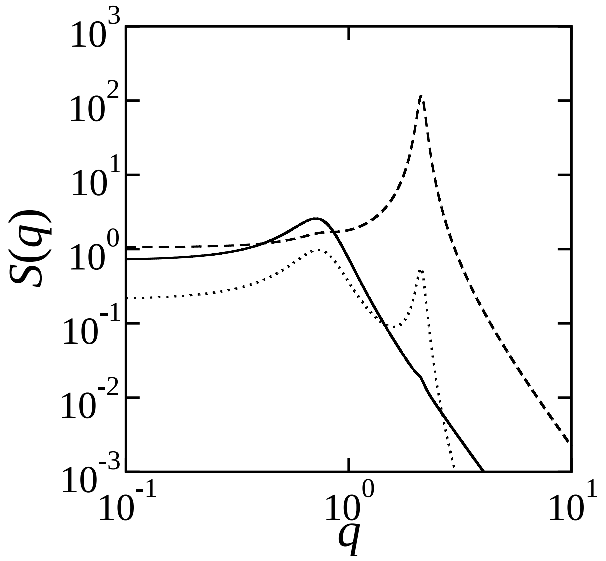

Figure 3.6: Static structure factors of the bilayer $S_{\phi\phi}$, $S_{\psi\psi}$, $S_{\phi\psi}$ for $\tilde{\tau}_\phi = 1.5, \tilde{\tau}_\psi = 1.01$, $B = A = 1$, $D = 0.0123$, $C = 0.1111$ $(q^*_\phi = 1/\sqrt{2}, q^*_\psi = 3/\sqrt{2})$, $\Lambda = 0.3$.

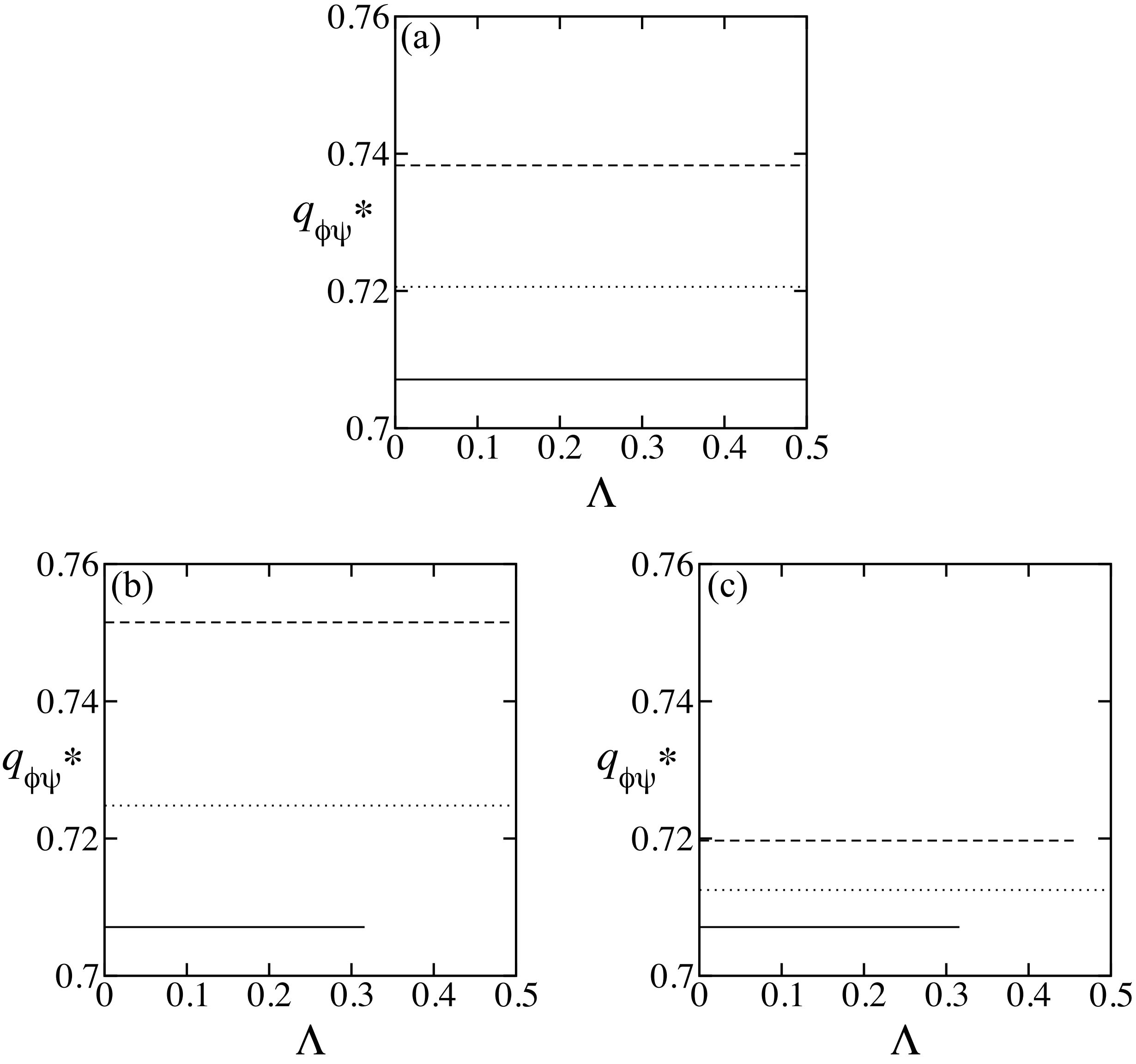

Figure 3.7: Effect of the coupling on the peak positions of the cross correlation of the structure factors $S_{\phi\psi}$. Solid lines represent the case of $B = A = D = C = 1$ $(q^*_\phi = q^*_\psi = 1/\sqrt{2})$, broken lines are $B = A = 1$, $D = 0.0625$, $C = 0.25$ $(q^*_\phi = 1/\sqrt{2}, q^*_\psi = \sqrt{2})$, and dotted lines are $B = A = 1$, $D = 0.0123$, $C = 0.1111$ $(q^*_\phi = 1/\sqrt{2}, q^*_\psi = 3/\sqrt{2})$. (a) $\tilde{\tau}_\phi = 1.5$, $\tilde{\tau}_\psi = 1.5$ (b) $\tilde{\tau}_\phi = 1.5$, $\tilde{\tau}_\psi = 1.2$ (c) $\tilde{\tau}_\phi = 1.2$, $\tilde{\tau}_\psi = 1.5$.

modulated monolayers increases with increasing the peak wavenumber, see Fig. 3.3(a).

When the temperatures of each monolayer are different, the peak position of $S_{\phi\psi}$ is shown in Fig. 3.8(b) and (c). We see that the distribution of the $q^*_{\phi\psi}$ changes, especially when the characteristic wavenumbers of the monolayers are large ($q_\phi > 2$ and $q_\psi > 2$).

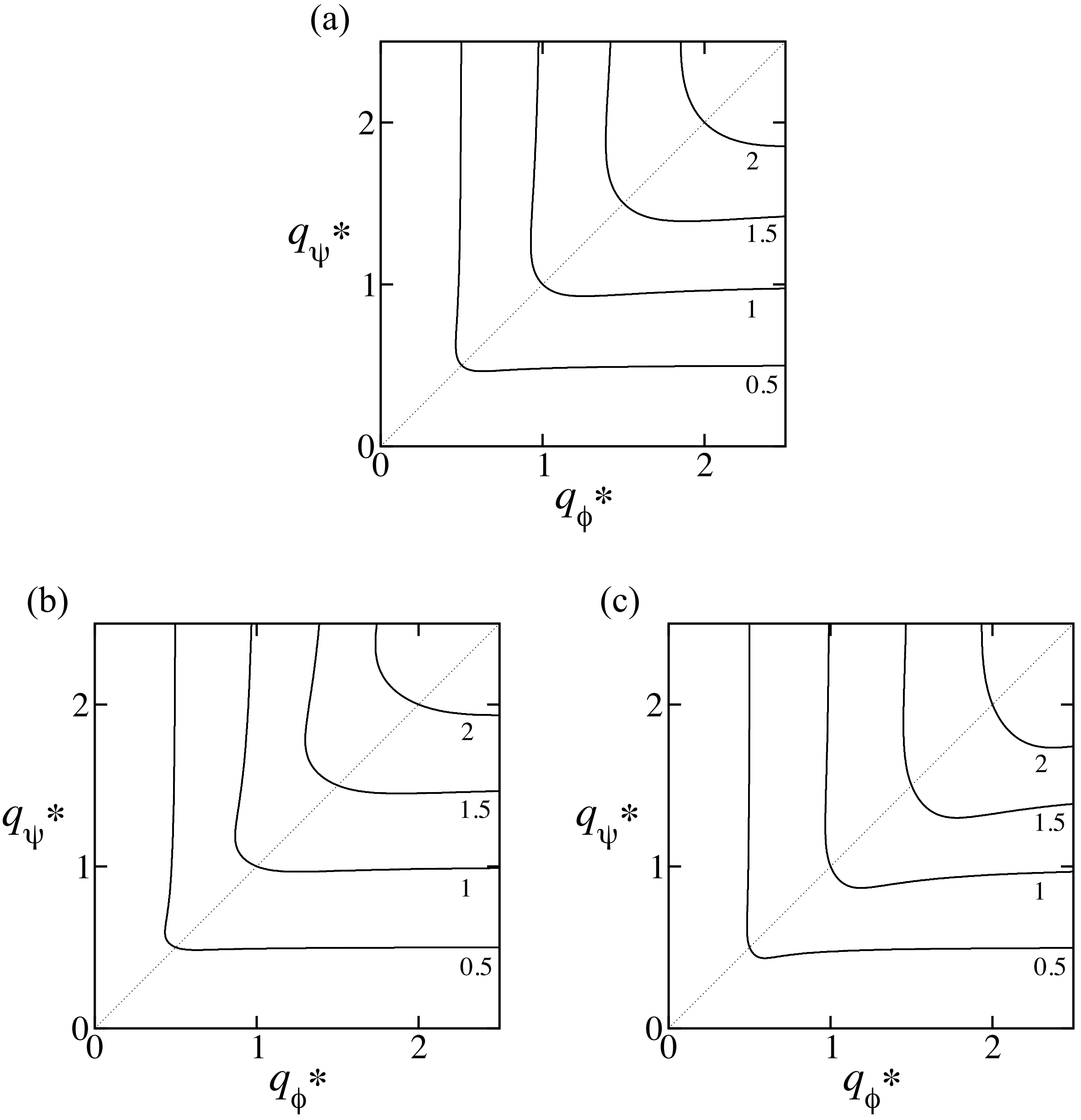

Figure 3.8: Contour plot of the peak positions of the structure factor $S_{\phi\psi}$ as functions of $q_\phi^* = \sqrt{A/2B}$ and $q_\psi^* = \sqrt{C/2D}$. Coupling constant is $\Lambda = 0.3$. The condition $A^2/B = C^2/D$ is assumed. (a) $\tilde{\tau}_\phi = \tilde{\tau}_\psi = 1.5$, (b) $\tilde{\tau}_\phi = 1.5, \tilde{\tau}_\psi = 1.2$, (c) $\tilde{\tau}_\phi = 1.2, \tilde{\tau}_\psi = 1.5$.

The peak height of $S_{\phi\psi}$ is plotted in Fig. 3.9 as a function of the coupling parameter Λ and the ratio of the characteristic wavenumbers q^*_ψ/q^*_ϕ while the parameters are fixed to $A = B = 1$ and $q^*_\phi = 1/\sqrt{2}$. The peak height becomes larger as the coupling parameter Λ is increased. This is because the critical temperature of the coupled bilayer is effectively changed for a larger coupling parameter. We also plot the transition lines. The left and right regions of the transition lines corresponds to the structured disorder phase and the ordered phase, respectively. The peak height is also increased as q^*_ψ/q^*_ϕ approaches unity, since the structure factors $S_{\phi\phi}$ and $S_{\psi\psi}$ overlap completely in this limit. When the temperature of the monolayer with small characteristic wavenumber is low (c), the peak height is large for smaller values of Λ.

The coupling parameter Λ changes the critical temperature. In Fig. 3.10, we plot the critical temperature as a function of the coupling constant Λ. First, we consider the case when both of the monolayers have the same temperature $\tilde{\tau}_\phi = \tilde{\tau}_\psi$ (a). Above the critical temperature, the system is in the structured disorder phase, whereas it is in the ordered phase below the critical temperature. When $q^*_\phi = q^*_\psi$, the critical temperature linearly increases with the coupling parameter Λ. When the ratio q^*_ϕ/q^*_ψ is larger than unity, the critical temperature becomes smaller. This is attributed to the smaller overlap of the peaks in the structure factors of the two monolayers. In Fig. 3.10(b) and (c), we fix the temperature of the one of the monolayers, and looked at the critical temperature of the bilayer. When the temperature of the monolayer with a small wavenumber is fixed at $\tilde{\tau}_\psi = 1.5$, the critical temperature $\tilde{\tau}^*_\phi$ is smaller when $\tilde{\tau}^*_\phi < 1.5$ and is larger when $\tilde{\tau}^*_\phi > 1.5$, compared with the case of the Fig. 3.10(a). When the temperature of the monolayer with a larger wavenumber is fixed at $\tilde{\tau}_\phi = 1.5$ and $q^*_\phi/q^*_\psi \neq 1$, the critical temperature of the ψ-monolayer is almost $\tilde{\tau}^*_\psi \approx 1$ when Λ is smaller than the threshold value. Because the peak height of the structure factor at q^*_ϕ is small for $\tilde{\tau}_\phi = 1.5$, the increase of the peak height due to the coupling is less effective. To summarize, in the case of the finite coupling

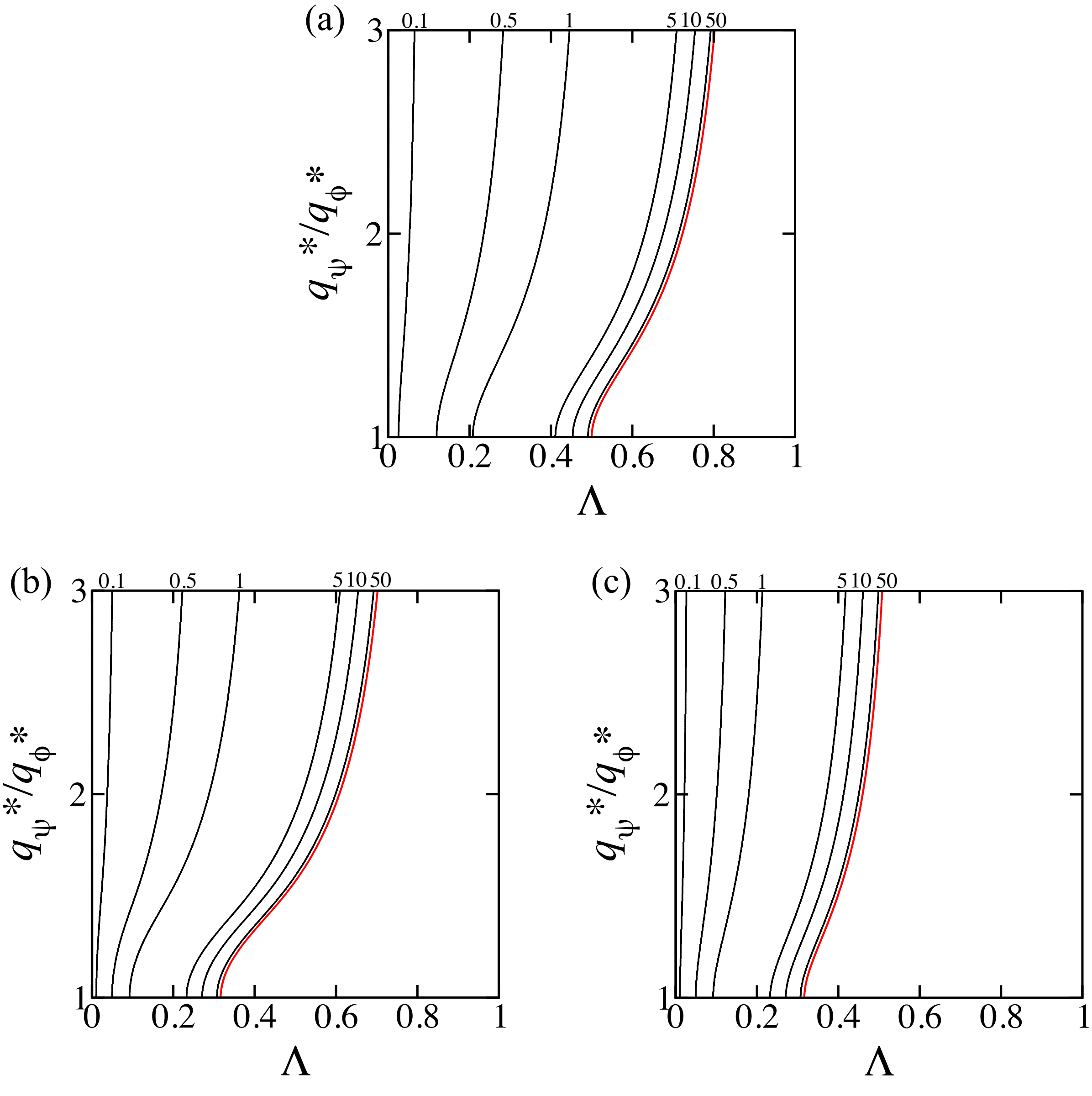

Figure 3.9: Contour plot of the intensity of the peak in the structure factor $S_{\phi\psi}(q = q^*_{\phi\psi})$ as a functions of characteristic wavenumber ratio q^*_ψ / q^*_ϕ and the coupling strength Λ for $B = A = 1$ and $C^2/D = 1$. Red lines represents the transition lines. (a) $\tilde{\tau}_\phi = \tilde{\tau}_\psi = 1.5$, (b) $\tilde{\tau}_\phi = 1.5, \tilde{\tau}_\psi = 1.2$, (c) $\tilde{\tau}_\phi = 1.2, \tilde{\tau}_\psi = 1.5$.

parameter, the temperature in the monolayer with the smaller wavenumber dominates the behavior of the critical temperature of the bilayer.

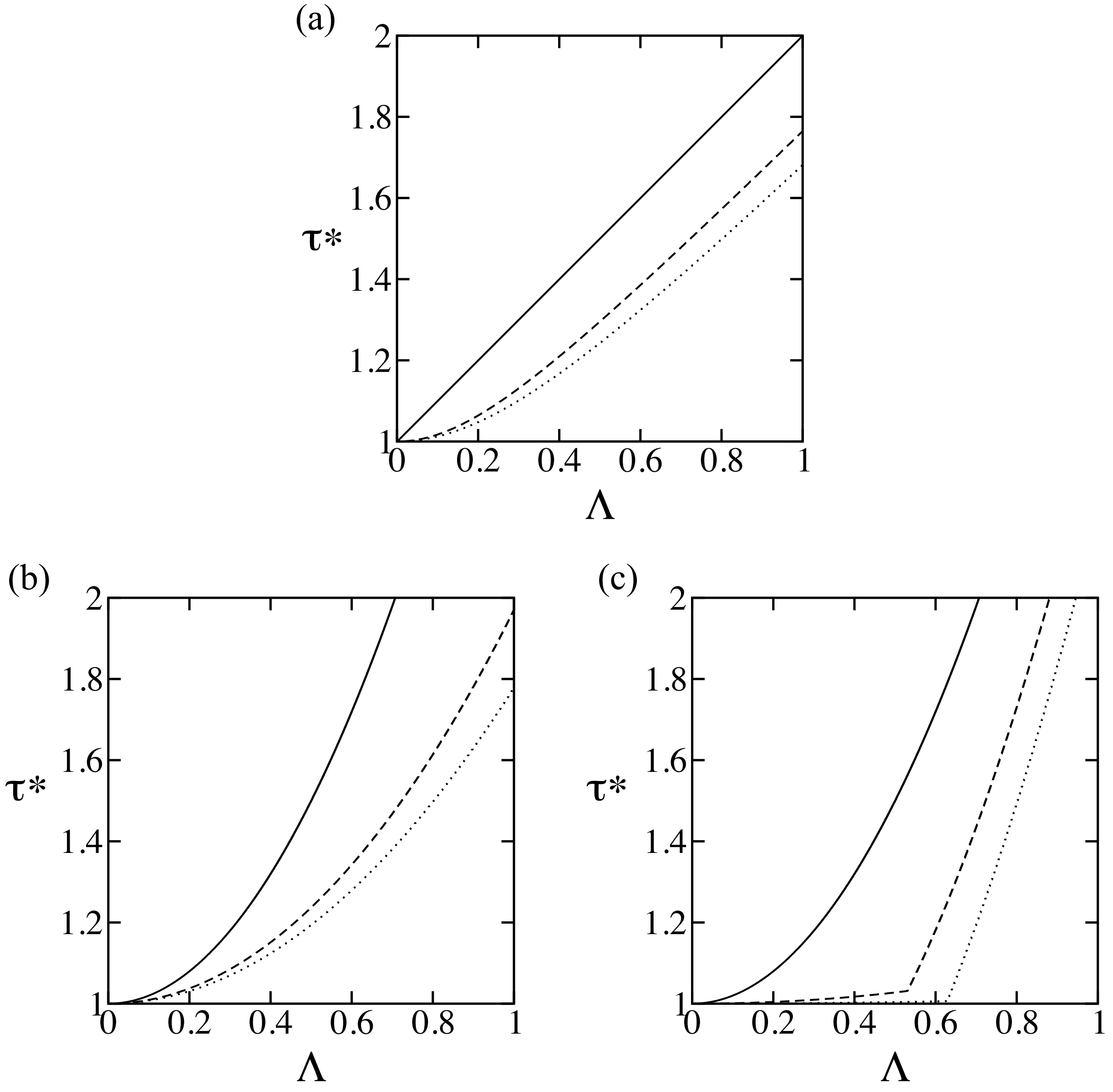

Figure 3.10: Transition temperatures as a function of the coupling constant. Solid line is $q^*_\psi/q^*_\phi = 1$, broken line is $q^*_\psi/q^*_\phi = 2$, dotted line is $q^*_\psi/q^*_\phi = 3$. $A = B = 1$, $C^2/D = 1$. (a) $\tilde{\tau}_\phi = \tilde{\tau}_\psi$, (b) $\tilde{\tau}_\psi = 1.5$, (c) $\tilde{\tau}_\phi = 1.5$.

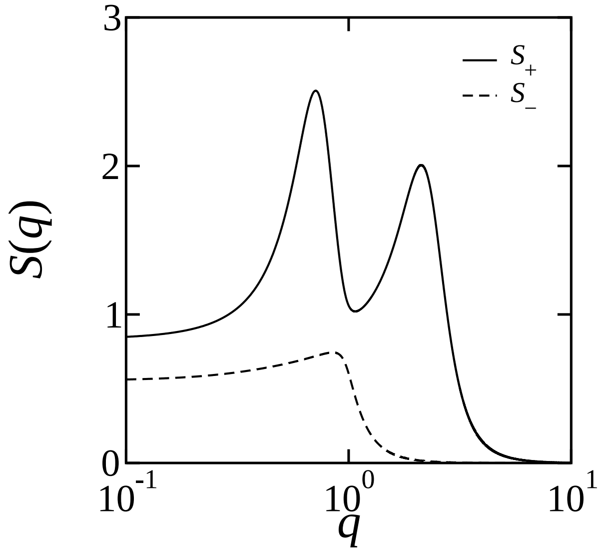

Figure 3.11: Diagonalized structure factors $S_\pm$ as functions of q for $\tilde{\tau}_\phi = \tilde{\tau}_\psi = 1.5$, $\Lambda = 0.3$ $B = A = 1$, $D = 0.0123$, $C = 0.1111$ ($q^*_\phi = 1/\sqrt{2}, q^*_\psi = 3/\sqrt{2}$).

Finally, it should be noted that the structure factor matrix Eq. (3.10) can be diagonalized as

$$S(\mathbf{q}) = \begin{bmatrix} 1/\Gamma_- & 0 \\ 0 & 1/\Gamma_+ \end{bmatrix}, \tag{3.28}$$

where

$$\Gamma_\pm(q) = \Gamma_\phi(q) + \Gamma_\psi(q) \mp \sqrt{(\Gamma_\phi(q) - \Gamma_\psi(q))^2 + \Lambda^2}. \tag{3.29}$$

In the above, $S_+ = 1/\Gamma_+$ and $S_- = 1/\Gamma_-$ express the in-plane and inter-membrane contribution to the structure factors, respectively. In Fig. 3.11, $S_+ = 1/\Gamma_+$ and $S_- = 1/\Gamma_-$ are plotted using the same parameters as in Fig. 3.3(b). It should be noted that although the peak position of $1/\Gamma_+$ is the same as that of Eqs. (3.14) and (3.15), the peak position of $1/\Gamma_-$ is larger than that of the cross correlation Eq. (3.16).

3.2 Dynamics

In this section, we discuss the dynamics of the concentration fluctuations in the coupled bilayers. In order to consider the time dependence, the fluctuation of the order parameters are denoted as $\delta\phi(\mathbf{r}, t)$ and $\delta\psi(\mathbf{r}, t)$ where t is time. The time evolution of these variables obey the following equations

$$\frac{\partial \delta\phi(\mathbf{r}, t)}{\partial t} = L_\phi \nabla^2 \frac{\delta F_{\mathrm{G}}}{\delta(\delta\phi(\mathbf{r}))} + \nu_\phi(\mathbf{r}, t), \tag{3.30}$$

$$\frac{\partial \delta\psi(\mathbf{r}, t)}{\partial t} = L_\psi \nabla^2 \frac{\delta F_{\mathrm{G}}}{\delta(\delta\psi(\mathbf{r}))} + \nu_\psi(\mathbf{r}, t), \tag{3.31}$$

where L_ϕ and L_ψ are the scaled kinetic coefficients. Using the free energy functional Eq. (3.4), we obtain

$$\frac{\partial \delta\phi(\mathbf{r}, t)}{\partial t} = L_\phi \nabla^2 [4B(\nabla^4 \delta\phi) + 4A(\nabla^2 \delta\phi) + \tilde{\tau}_\phi \delta\phi - \Lambda \delta\psi] + \nu_\phi(\mathbf{r}, t), \tag{3.32}$$

$$\frac{\partial \delta\psi(\mathbf{r}, t)}{\partial t} = L_\psi \nabla^2 [4D(\nabla^4 \delta\psi) + 4C(\nabla^2 \delta\psi) + \tilde{\tau}_\psi \delta\psi - \Lambda \delta\phi] + \nu_\psi(\mathbf{r}, t). \tag{3.33}$$

In the above, $\nu_\phi(\mathbf{r}, t)$ and $\nu_\psi(\mathbf{r}, t)$ represent Gaussian noises which satisfy

$$\langle \nu_\phi(\mathbf{r}, t) \rangle = \langle \nu_\psi(\mathbf{r}, t) \rangle = 0, \tag{3.34}$$

$$\langle \nu_\phi(\mathbf{r}, t) \nu_\phi(\mathbf{r}', t') \rangle = -L_\phi \nabla^2 \delta(\mathbf{r} - \mathbf{r}') \delta(t - t'), \tag{3.35}$$

$$\langle \nu_\psi(\mathbf{r}, t) \nu_\psi(\mathbf{r}', t') \rangle = -L_\psi \nabla^2 \delta(\mathbf{r} - \mathbf{r}') \delta(t - t'), \tag{3.36}$$

$$\langle \nu_\phi(\mathbf{r}, t) \nu_\psi(\mathbf{r}, t) \rangle = 0, \tag{3.37}$$

where $\langle \cdots \rangle$ indicates the space and time average.

We define the Fourier transform of the fluctuations both in space and time as

$$\delta\phi(\mathbf{q}, \omega) = \int \mathrm{d}\mathbf{r}\, \mathrm{d}t\, \delta\phi(\mathbf{r}, t) \exp[-i(\mathbf{q} \cdot \mathbf{r} - \omega t)], \tag{3.38}$$

and

$$\delta\psi(\mathbf{q}, \omega) = \int \mathrm{d}\mathbf{r}\, \mathrm{d}t\, \delta\psi(\mathbf{r}, t) \exp[-i(\mathbf{q} \cdot \mathbf{r} - \omega t)]. \tag{3.39}$$

Inserting Eq. (3.4) into Eqs. (3.30) and (3.31), we obtain

$$i\omega\delta\phi(\mathbf{q},\omega) = -q^2 L_\phi[2\Gamma_\phi(q)\delta\phi(\mathbf{q},\omega) - \Lambda\delta\psi(\mathbf{q},\omega)] + \nu_\phi(\mathbf{q},\omega), \tag{3.40}$$

$$i\omega\delta\psi(\mathbf{q},\omega) = -q^2 L_\psi[2\Gamma_\psi(q)\delta\psi(\mathbf{q},\omega) - \Lambda\delta\phi(\mathbf{q},\omega)] + \nu_\psi(\mathbf{q},\omega). \tag{3.41}$$

Then $\delta\phi(\mathbf{q},\omega)$ and $\delta\psi(\mathbf{q},\omega)$ can be obtained as

$$\delta\phi(\mathbf{q},\omega) = \frac{[2L_\psi q^2\Gamma_\psi(q) + i\omega]\nu_\phi(\mathbf{q},\omega) + L_\phi q^2\Lambda\nu_\psi(\mathbf{q},\omega)}{[2L_\phi q^2\Gamma_\phi(q) + i\omega][2L_\psi q^2\Gamma_\psi(q) + i\omega] - L_\phi L_\psi q^4\Lambda^2}, \tag{3.42}$$

$$\delta\psi(\mathbf{q},\omega) = \frac{L_\psi q^2\Lambda\nu_\phi(\mathbf{q},\omega) + [2L_\phi q^2\Gamma_\phi(q) + i\omega]\nu_\psi(\mathbf{q},\omega)}{[2L_\phi q^2\Gamma_\phi(q) + i\omega][2L_\psi q^2\Gamma_\psi(q) + i\omega] - L_\phi L_\psi q^4\Lambda^2}. \tag{3.43}$$

Here the properties of noises are expressed in the Fourier space as

$$\langle\nu_\phi(\mathbf{q},\omega)\rangle = \langle\nu_\psi(\mathbf{q},\omega)\rangle = 0, \tag{3.44}$$

$$\langle\nu_\phi(\mathbf{q},\omega)\nu_\phi(-\mathbf{q},-\omega)\rangle = 2L_\phi q^2, \tag{3.45}$$

$$\langle\nu_\psi(\mathbf{q},\omega)\nu_\psi(-\mathbf{q},-\omega)\rangle = 2L_\psi q^2, \tag{3.46}$$

$$\langle\nu_\phi(\mathbf{q},\omega)\nu_\psi(-\mathbf{q},-\omega)\rangle = 0. \tag{3.47}$$

Using the above expressions, the dynamical structure factors can be obtained to be

$$S_{\phi\phi}(\mathbf{q},\omega) = \langle\delta\phi(\mathbf{q},\omega)\delta\phi(-\mathbf{q},-\omega)\rangle = \frac{2L_\phi q^2(\omega^2 + \omega_\psi^2)}{(\omega^2 + \omega_\phi^2)(\omega^2 + \omega_\psi^2) - L_\phi L_\psi q^4\Lambda^2\omega_{\phi\psi}^2}, \tag{3.48}$$

$$S_{\psi\psi}(\mathbf{q},\omega) = \langle\delta\psi(\mathbf{q},\omega)\delta\psi(-\mathbf{q},-\omega)\rangle = \frac{2L_\psi q^2(\omega^2 + \omega_\phi^2)}{(\omega^2 + \omega_\phi^2)(\omega^2 + \omega_\psi^2) - L_\phi L_\psi q^4\Lambda^2\omega_{\phi\psi}^2}, \tag{3.49}$$

$$S_{\phi\psi}(\mathbf{q},\omega) = \langle\delta\phi(\mathbf{q},\omega)\delta\psi(-\mathbf{q},-\omega)\rangle = \frac{2L_\phi L_\psi q^4\Lambda\omega_{\phi\psi}}{(\omega^2 + \omega_\phi^2)(\omega^2 + \omega_\psi^2) - L_\phi L_\psi q^4\Lambda^2\omega_{\phi\psi}^2}, \tag{3.50}$$

where

$$\omega_\phi^2 = 4L_\phi^2 q^4[\Gamma_\phi(q)]^2 + L_\phi L_\psi q^4\Lambda^2, \tag{3.51}$$

$$\omega_\psi^2 = 4L_\psi^2 q^4[\Gamma_\psi(q)]^2 + L_\phi L_\psi q^4\Lambda^2, \tag{3.52}$$

$$\omega_{\phi\psi} = 2q^2[L_\phi\Gamma_\phi(q) + L_\psi\Gamma_\psi(q)]. \tag{3.53}$$

The above structure factors are decomposed into two terms

$$S_{ij}(\mathbf{q},\omega)=\frac{\alpha_{ij}}{\omega^2+\omega_+^2}+\frac{\beta_{ij}}{\omega^2+\omega_-^2}, \tag{3.54}$$

where i and j are either ϕ or ψ, and $\omega_\pm$ are the characteristic frequencies given by

$$\omega_\pm^2=\frac{1}{2}\left[\omega_\phi^2+\omega_\psi^2\mp\sqrt{(\omega_\phi^2-\omega_\psi^2)^2+4L_\phi L_\psi q^4\Lambda^2\omega_{\phi\psi}^2}\right], \tag{3.55}$$

and the coefficients are

$$\alpha_{\phi\phi}=\frac{2L_\phi q^2(\omega_\psi^2-\omega_+^2)}{\omega_-^2-\omega_+^2}, \qquad \beta_{\phi\phi}=\frac{2L_\phi q^2(\omega_-^2-\omega_\psi^2)}{\omega_-^2-\omega_+^2}, \tag{3.56}$$

$$\alpha_{\psi\psi}=\frac{2L_\psi q^2(\omega_\phi^2-\omega_+^2)}{\omega_-^2-\omega_+^2}, \qquad \beta_{\psi\psi}=\frac{2L_\psi q^2(\omega_-^2-\omega_\phi^2)}{\omega_-^2-\omega_+^2}, \tag{3.57}$$

$$\alpha_{\phi\psi}=\frac{2L_\phi L_\psi q^4\Lambda\omega_{\phi\psi}}{\omega_-^2-\omega_+^2}, \qquad \beta_{\phi\psi}=-\frac{2L_\phi L_\psi q^4\Lambda\omega_{\phi\psi}}{\omega_-^2-\omega_+^2}. \tag{3.58}$$

The intermediate structure factors are obtained by

$$S_{\phi\phi}(\mathbf{q},t)=\int\frac{\mathrm{d}\omega}{2\pi}\,S_{\phi\phi}(\mathbf{q},\omega)\exp(-i\omega t), \tag{3.59}$$

$$S_{\psi\psi}(\mathbf{q},t)=\int\frac{\mathrm{d}\omega}{2\pi}\,S_{\psi\psi}(\mathbf{q},\omega)\exp(-i\omega t), \tag{3.60}$$

$$S_{\phi\psi}(\mathbf{q},t)=\int\frac{\mathrm{d}\omega}{2\pi}\,S_{\phi\psi}(\mathbf{q},\omega)\exp(-i\omega t). \tag{3.61}$$

Using equation Eq. (3.54), we simply obtain

$$S_{ij}(\mathbf{q},t)=\frac{\alpha_{ij}}{2\omega_+}\exp(-\omega_+t)+\frac{\beta_{ij}}{2\omega_-}\exp(-\omega_-t). \tag{3.62}$$

The concentration fluctuations decay as double exponentials with two decay times.

When $L_\phi=L_\psi=L$, the characteristic frequencies are simplified to

$$\omega_\pm=Lq^2\left[\Gamma_\phi(q)+\Gamma_\psi(q)\mp\sqrt{(\Gamma_\phi(q)-\Gamma_\psi(q))^2+\Lambda^2}\right]. \tag{3.63}$$

The inverse of $\omega_\pm$ gives the decay times of the concentration fluctuations. These decay times are plotted in Fig. 3.12 as a function of wavenumber q. When the two monolayers are decoupled ($\Lambda=0$), the intermediate structure factor of each monolayer becomes

$$S_\phi(\mathbf{q},t)=\frac{1}{2\Gamma_\phi(q)}\exp[-2Lq^2\Gamma_\phi(q)t], \tag{3.64}$$

$$S_{\psi}(\mathbf{q},t) = \frac{1}{2\Gamma_{\psi}(q)} \exp[-2Lq^2\Gamma_{\psi}(q)t]. \tag{3.65}$$

We plotted the decay times $1/\omega_{\phi} = 1/(2Lq^2\Gamma_{\phi})$, $1/\omega_{\psi} = 1/(2Lq^2\Gamma_{\psi})$ in Fig. 3.12(a). The parameters used in Fig. 3.12 are the same as those in Fig. 3.3. There are shoulders and peaks at the characteristic wavenumbers ($q^* = 1/\sqrt{2}, 3/\sqrt{2}$). The decay time at the peak position is longer for a larger structure. The coupled case is shown in Fig. 3.12(b). Due to the coupling, the decay times are represented as the major and the minor parts. The major and the minor decay times are the in-plane and inter-membrane fluctuations, respectively. The minor decay time has a shoulder between the two characteristic wavenumbers. Similar to the effect seen in Fig. 3.3, the coupling increases the decay time corresponding to the smaller wavenumber structure.

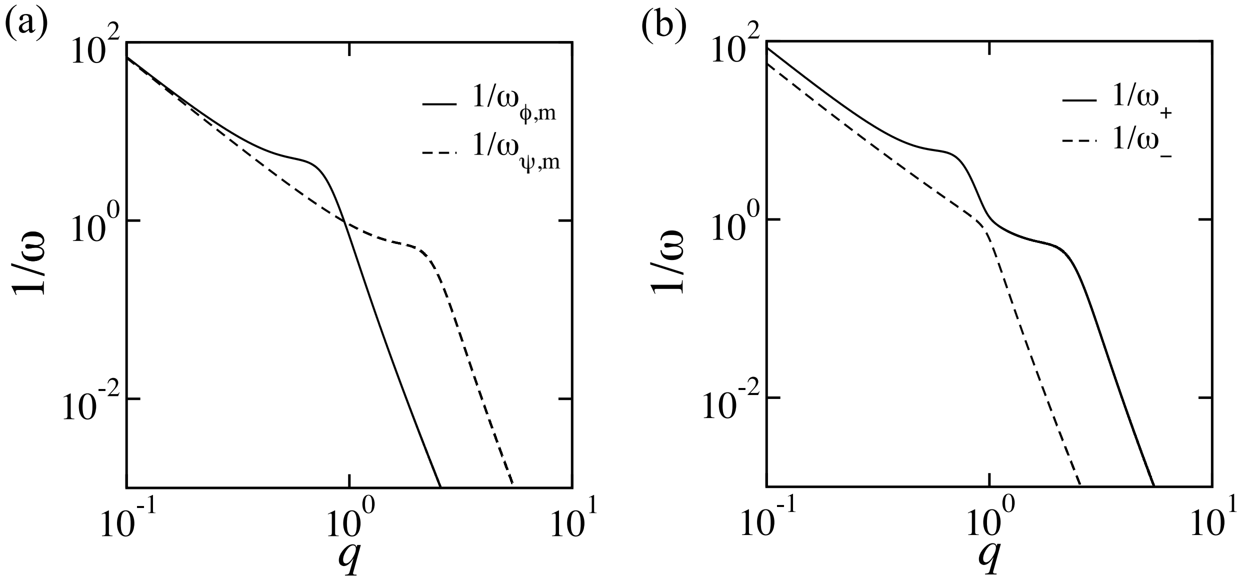

Figure 3.12: Decay time for the concentration fluctuations for $\tilde{\tau}_\phi = \tilde{\tau}_\psi = 1.5$, $B = A = 1$, $D = 0.0123$, $C = 0.1111$, $(q^*_\phi = 1/\sqrt{2}, q^*_\psi = 3\sqrt{2})$, $L = 1$. (a) $\Lambda = 0$ decoupled case and (b) $\Lambda = 0.3$ coupled case.

In Fig. 3.13, we plot the the time courses of scaled structure factors $S_{\phi\phi}(q,t)$ in (a) and (b), and $S_{\psi\psi}(q,t)$ in (c) and (d) for different wavenumbers. The decoupled cases in Fig. 3.13(a) and (c) show that the concentration fluctuations decay exponentially with time for any wavenumber. For the coupled cases shown in Fig. 3.13(b) and (d), the two decay modes are seen for $S_{\phi\phi}(\mathbf{q},t)$ for $q=\sqrt{2}$ being the characteristic wavenumber of the ψ-monolayer, and for $S_{\psi\psi}(\mathbf{q},t)$ for $q=1/\sqrt{2}$ being the characteristic wavenumber of the ϕ-monolayer. These second decay modes correspond to that of the $S_{\phi\psi}(\mathbf{q},t)$ as shown in Fig. 3.14.

At the crossover point, the two contributions in Eq. (3.62) become equal so that

$$\frac{\alpha_{\phi\phi}}{\omega_+}\exp(-\omega_+ t_\phi^*) = \frac{\beta_{\phi\phi}}{\omega_-}\exp(-\omega_- t_\phi^*), \tag{3.66}$$

and

$$\frac{\alpha_{\psi\psi}}{\omega_+}\exp(-\omega_+ t_\psi^*) = \frac{\beta_{\psi\psi}}{\omega_-}\exp(-\omega_- t_\psi^*). \tag{3.67}$$

Then we get the expression for the crossover time as

$$t_\phi^* = \log\left(\frac{\omega_+^2-\omega_\psi^2}{\omega_\psi^2-\omega_-^2}\frac{\omega_-}{\omega_+}\right)^{\frac{1}{\omega_+-\omega_-}}, \tag{3.68}$$

$$t_\psi^* = \log\left(\frac{\omega_+^2-\omega_\phi^2}{\omega_\phi^2-\omega_-^2}\frac{\omega_-}{\omega_+}\right)^{\frac{1}{\omega_+-\omega_-}}. \tag{3.69}$$

It should be noted that this expression is valid only $t_\phi^*, t_\psi^* > 0$.

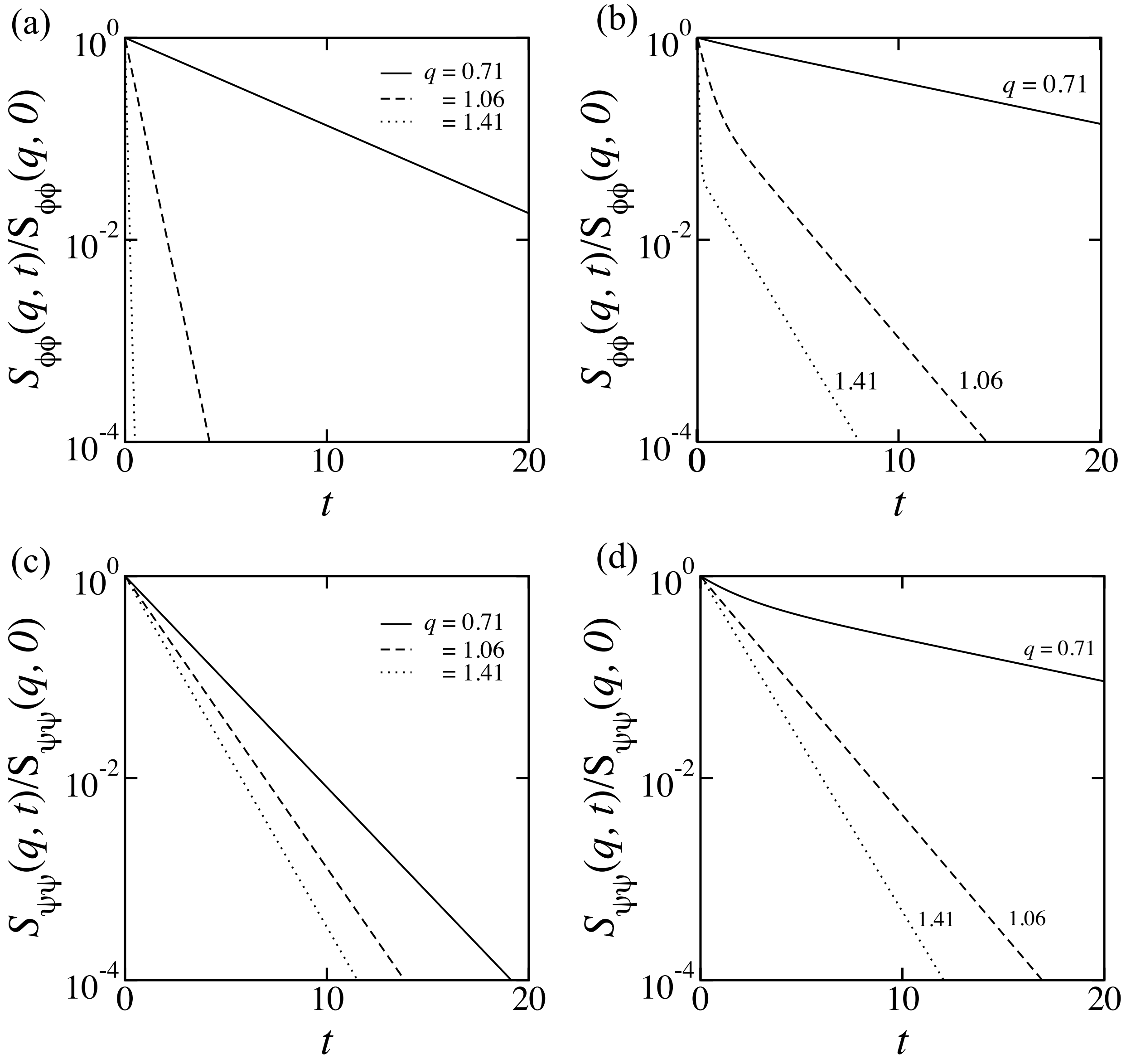

Figure 3.13: Time evolution of the scaled intermediate structure factors in ϕ monolayer (a,b) and ψ monolayer (c,d). Parameters are $\tilde{\tau}_\phi = \tilde{\tau}_\psi = 1.4$, $B = A = 1$, $D = 0.0625$, $C = 0.25$, $(q^*_\phi = 1/\sqrt{2}, q^*_\psi = \sqrt{2})$. $\Lambda = 0$ for (a,c) and $\Lambda = 0.4$ for (b,d).

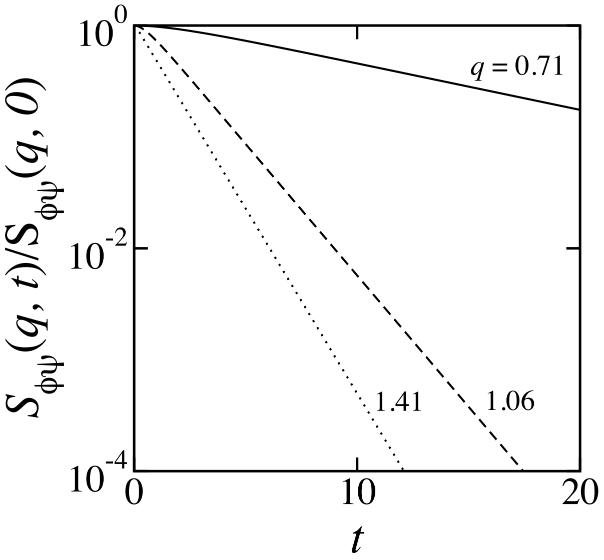

Figure 3.14: Time evolution of the scaled intermediate structure factor $S_{\phi\psi}$. Parameters are $\tilde{\tau}_\phi = \tilde{\tau}_\psi = 1.4$, $B = A = 1$, $D = 0.0625$, $C = 0.25$ ($q^*_\phi = 1/\sqrt{2}, q^*_\psi = \sqrt{2}$), $\Lambda = 0.4$.

Chapter 4

Phase Separations

In this chapter, we discuss the phase separation behavior of the bilayer below the critical temperature. First, we demonstrate the phase behavior of the lipid monolayers. Then we obtain the mean-field phase diagrams of coupled bilayers when the two monolayers have the same preferred modulation wavelength. We have also performed numerical simulations for the phase separation dynamics, especially when two monolayers have different preferred modulation wavelengths.

4.1 Bilayers with the same q^*

4.1.1 Decoupled case ($\Lambda = 0$)

The phase behavior for the uncoupled case ($\Lambda = 0$), can be obtained by the analysis of the free energy [43]

$$F_{\mathrm{m}}[\phi] = \int \mathrm{d}\mathbf{r} \left[2B(\nabla^2\phi)^2 - 2A(\nabla\phi)^2 + \frac{\tau}{2}\phi^2 + \frac{1}{4}\phi^4 - \mu\phi \right], \tag{4.1}$$

and is only briefly reviewed here (see also Fig. 4.3(a)).

For a 2D system, the mean-field phase diagram can be constructed by comparing the free energies of striped (S) and hexagonal (H) phases (see Figs. 4.1, 4.2). In terms of the ϕ-order parameter, the stripe phase is described by

$$\phi_{\mathrm{S}}(\mathbf{r}) = \phi_0 + 2\phi_q \cos(qx), \tag{4.2}$$

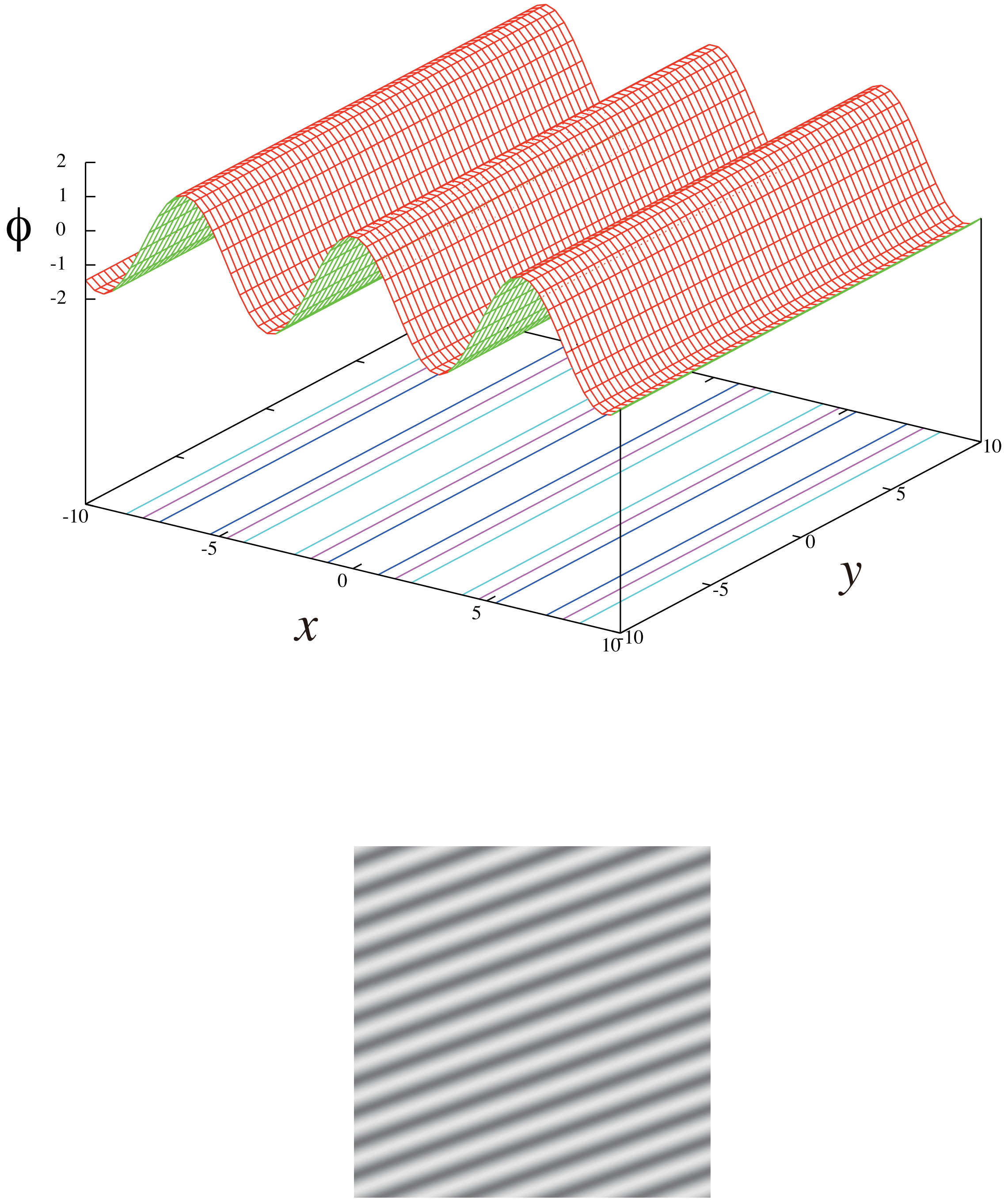

stripe

Figure 4.1: Morphology of the stripe phase.

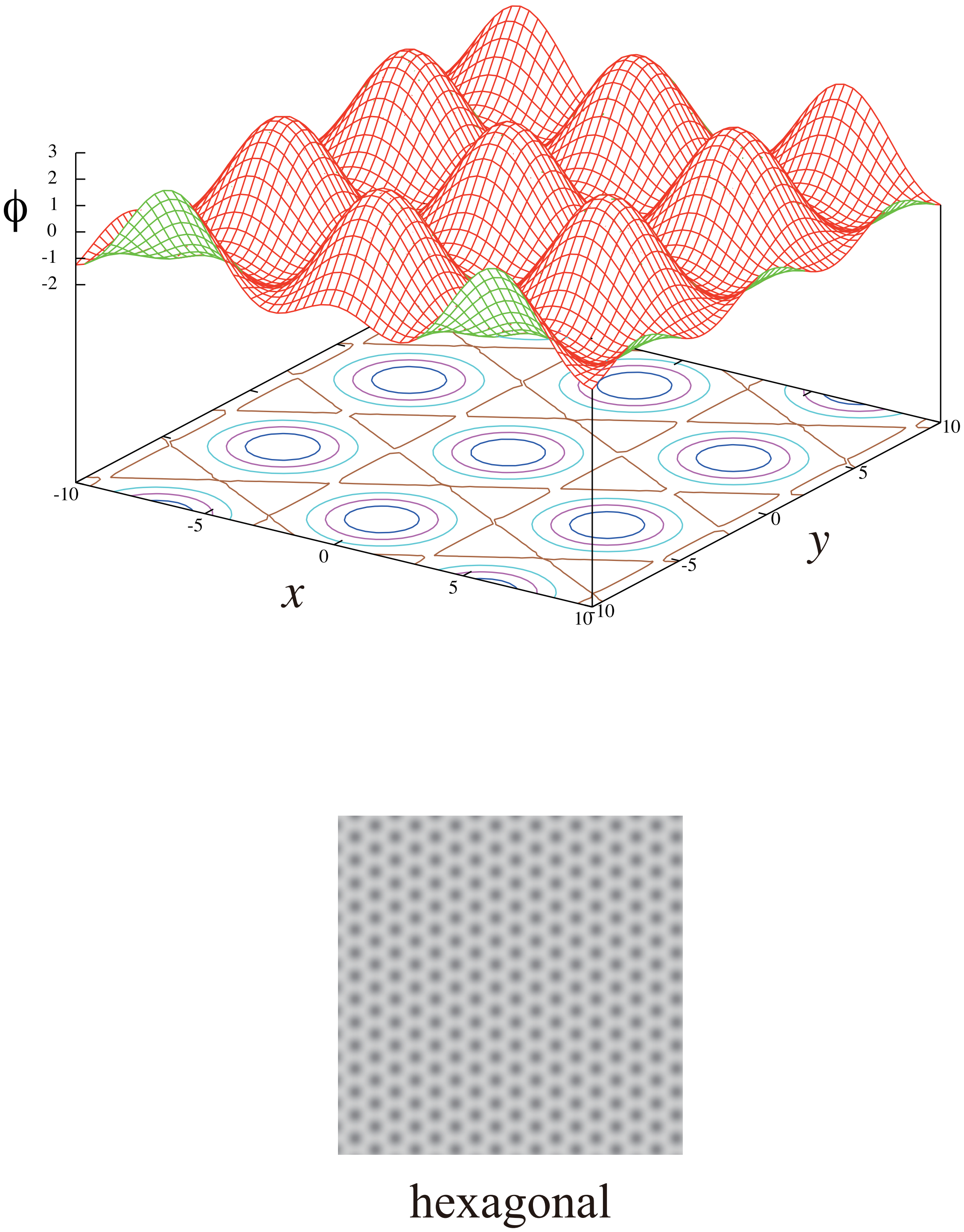

Figure 4.2: Morphology of the hexagonal phase.

where $\phi_0 = \langle \phi \rangle$ is the spatially averaged composition (imposed by the chemical potential μ_ϕ), and ϕ_q is the amplitude of the q-mode in the x-direction. Similarly, the composition of the hexagonal phase is given by a superposition of three 2D modes of equal magnitude, $|\mathbf{q}_i| = q$

$$\phi_{\rm H}(\mathbf{r}) = \phi_0 + \frac{2\phi_q}{\sqrt{3}} \sum_{i=1}^{3} \cos(\mathbf{q}_i \cdot \mathbf{r}), \tag{4.3}$$

where

$$\begin{aligned} \mathbf{q}_1 &= q\hat{x}, \\ \mathbf{q}_2 &= \frac{q}{2}\left(-\hat{x} + \sqrt{3}\hat{y}\right), \\ \mathbf{q}_3 &= \frac{q}{2}\left(-\hat{x} - \sqrt{3}\hat{y}\right), \end{aligned} \tag{4.4}$$

and $\sum_{i=1}^{3} \mathbf{q}_i = 0$. In the above, we consider a single-mode modulation. This can be justified for the weak segregation regime close to the critical point [41].

Averaging over one spatial period, we obtain the free energy densities of the striped, hexagonal, and disordered phases, respectively

$$f_{\rm S0}(\phi_0, \phi_q, q; \tau) = \frac{\tau}{2}\phi_0^2 + \frac{1}{4}\phi_0^4 + (\tau + 3\phi_0^2)\phi_q^2 + \frac{3}{2}\phi_q^4 + 4(Bq^4 - Aq^2)\phi_q^2, \tag{4.5}$$

$$f_{\rm H0}(\phi_0, \phi_q, q; \tau) = \frac{\tau}{2}\phi_0^2 + \frac{1}{4}\phi_0^4 + (\tau + 3\phi_0^2)\phi_q^2 + \frac{4}{\sqrt{3}}\phi_0\phi_q^3 + \frac{5}{2}\phi_q^4 + 4(Bq^4 - Aq^2)\phi_q^2, \tag{4.6}$$

$$f_{\rm D}(\phi_0; \tau) = \frac{\tau}{2}\phi_0^2 + \frac{1}{4}\phi_0^4, \tag{4.7}$$

By minimizing the free energy densities with respect to q, we obtain the most unstable wavenumber as $q^* = \sqrt{A/2B}$. By setting $q = q^*$ in Eqs. (4.5) and (4.6), we have

$$f_{\rm S}(\phi_0, \phi_q; \tau) = \frac{\tau}{2}\phi_0^2 + \frac{1}{4}\phi_0^4 + \left(\tau - \frac{A^2}{B} + 3\phi_0^2\right)\phi_q^2 + \frac{3}{2}\phi_q^4, \tag{4.8}$$

$$f_{\rm H}(\phi_0, \phi_q; \tau) = \frac{\tau}{2}\phi_0^2 + \frac{1}{4}\phi_0^4 + \left(\tau - \frac{A^2}{B} + 3\phi_0^2\right)\phi_q^2 + \frac{4}{\sqrt{3}}\phi_0\phi_q^3 + \frac{5}{2}\phi_q^4. \tag{4.9}$$

From the free energy densities Eqs. (4.8) and (4.9), we have the minimized amplitudes are obtained by the condition $\partial f_i / \partial \phi_q = 0$. For stripe phase, we have

$$\phi_q^{*2} = -\frac{\tau - A^2/B + 3\phi_0^2}{3}, \tag{4.10}$$

and for the hexagonal phase, we get

$$\phi^*_{q,\pm} = \frac{-\sqrt{3}\phi_0 \pm \sqrt{5A^2/B - 5\tau - 12\phi_0^2}}{5}, \tag{4.11}$$

with $\phi^*_{q,+}$ for $\phi_0 < 0$ and $\phi^*_{q,-}$ for $\phi_0 > 0$. For given ϕ_0, τ, B and A, we calculate the minimized free energies $f_{\rm S}(\phi_0;\tau)$, $f_{\rm H}(\phi_0;\tau)$ and $f_{\rm D}(\phi_0;\tau)$ numerically, and determine phase which has the lowest energy.

In Fig. 4.3(a), we reproduce the original phase diagram of Ref. [42, 43] ($B = A = 1$). The stripe, hexagonal, and disorder phases are separated by first-order phase-transition lines. Regions of two-phase coexistence do exist but are omitted from the figure for clarity sake [50]. Thus, the transition lines indicate the locus of points at which the free energies of two different phases cross each other, and are not the proper phase boundaries (binodals). The critical point (filled circle) is located at $(\phi_0, \tau) = (0, 1)$.

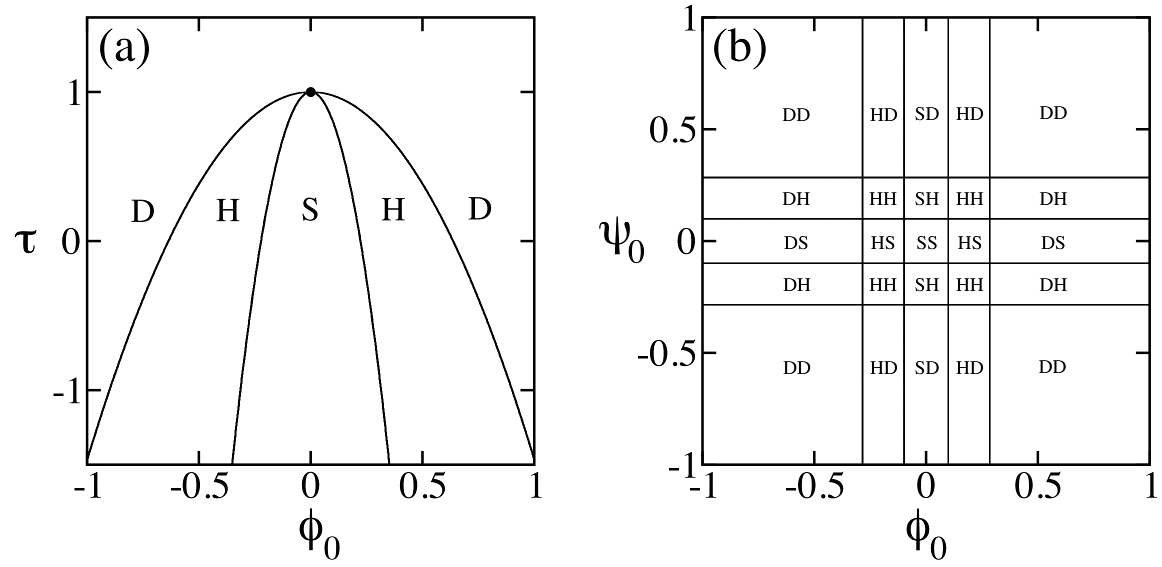

Figure 4.3: (a) Mean-field phase diagram of a single monolayer with a modulated structure in the vicinity of the critical temperature, computed using a model as in Eqs. (4.7)-(4.9). Here $B = A = 1$. ϕ_0 is the average composition and τ is the reduced temperature. The three phases are: striped (S), hexagonal (H), and disordered (D). These phases are separated by first-order transition lines, while for clarity we omit showing coexistence regions. The filled circle located at $(\phi_0, \tau) = (0, 1)$ indicates the critical point. Note the shift of the critical temperature from zero to unity when the modulated phases are considered. (b) Mean-field phase diagram of decoupled ($\Lambda = 0$) modulated monolayers at $\tau_\phi = \tau_\psi = 0.8$, $B = A = D = C = 1$. ϕ_0 and ψ_0 are the average compositions in the two leaflets. The notations of the different phases are described in the text (see Sec. 4.1.2). All the phases are separated by first-order transition lines.

4.1.2 Coupled case ($\Lambda \neq 0$)

The phase diagrams of the coupled bilayers are obtained through the mean-field analysis as before. We consider the case when $B = A = D = C = 1$ so that the preferred wavenumbers are the same for both monolayers, $q^*_\phi = q^*_\psi = q^* = 1/\sqrt{2}$. The mean-field phase diagram is calculated within the single-mode approximation. Various combinations of 2D modulated structures appearing in the two monolayers are possible. The first example is the striped-striped (SS) phase, in which both monolayers exhibit the striped phase. This can be expressed as

$$\phi_{\rm S}(\mathbf{r}) = \phi_0 + 2\phi_q \cos(qx), \tag{4.12}$$

$$\psi_{\rm S}(\mathbf{r}) = \psi_0 + 2\psi_q \cos(qx), \tag{4.13}$$

where $\phi_0 = \langle\phi\rangle$ and $\psi_0 = \langle\psi\rangle$ are the average compositions, ϕ_q and ψ_q are the respective amplitudes. These composition profiles are substituted into the free energy of Eq. (2.18). Averaging over one spatial period, we obtain the free energy density of the SS phase:

$$f_{\rm SS} = f_{\rm S}(\phi_0, \phi_q; \tau_\phi) + f_{\rm S}(\psi_0, \psi_q; \tau_\psi) - \Lambda(\phi_0\psi_0 + 2\phi_q\psi_q), \tag{4.14}$$

where $f_{\rm S}$ is defined in Eq. (4.8). By minimizing $f_{\rm SS}$ with respect to both ϕ_q and ψ_q, the conditions for the minimized amplitudes are obtained as

$$\begin{aligned} &(\tau_\phi - 1 + 3\phi_0^2)\phi_q + 3\phi_q^3 - \Lambda\psi_q = 0, \\ &(\tau_\psi - 1 + 3\psi_0^2)\psi_q + 3\psi_q^3 - \Lambda\phi_q = 0. \end{aligned} \tag{4.15}$$

For given ϕ_0, ψ_0, τ_ϕ, τ_ψ and Λ, we numerically calculate the minimized amplitudes ϕ_q^* and ψ_q^*, and the minimized free energy $f_{\rm SS}(\phi_0, \psi_0; \tau_\phi, \tau_\psi, \Lambda)$. (The source code for the calculation is listed in Appendix D)

When either ϕ_q or ψ_q vanishes, the corresponding monolayer is in its disordered phase and the mixed bilayer state will be called the striped-disordered (SD) or the disordered-striped (DS) phase. Note that we use the convention that the first index is of the ϕ–leaflet and the second of the ψ–one. When both ϕ_q and ψ_q are zero, the free energy density of the disordered-disordered (DD) phase is given by

$$f_{\rm DD} = f_{\rm D}(\phi_0; \tau_\phi) + f_{\rm D}(\psi_0; \tau_\psi) - \Lambda\phi_0\psi_0, \tag{4.16}$$

where $f_{\rm D}$ is defined in Eq. (4.7). This free energy $f_{\rm DD}$ was analyzed in Ref. [39] in order to investigate the macro–phase separation of a bilayer membrane with coupled monolayers. It was shown that the bilayer can exist in four different phases, and can also exhibit a three-phase coexistence.

Similar to the stripe-stripe case, the order parameters of the hexagonal-hexagonal (HH) phase can be represented as

$$\phi_{\rm H}(\mathbf{r}) = \phi_0 + \frac{2\phi_q}{\sqrt{3}} \sum_{i=1}^{3} \cos(\mathbf{q}_i \cdot \mathbf{r}), \tag{4.17}$$

$$\psi_{\rm H}(\mathbf{r}) = \psi_0 + \frac{2\psi_q}{\sqrt{3}} \sum_{i=1}^{3} \cos(\mathbf{q}_i \cdot \mathbf{r}). \tag{4.18}$$

Where the basis of the three $\mathbf{q}_i$ was defined in Eq. (4.4). By repeating the same procedure as for the SS phase, the free energy density of the HH phase is obtained as

$$f_{\rm HH} = f_{\rm H}(\phi_0, \phi_q; \tau_\phi) + f_{\rm H}(\psi_0, \psi_q; \tau_\psi) - \Lambda(\phi_0\psi_0 + 2\phi_q\psi_q), \tag{4.19}$$

where $f_{\rm H}$ is defined in Eq. (4.9). The conditions for the minimized amplitudes are

$$\begin{aligned} &(\tau_\phi - 1 + 3\phi_0^2)\phi_q + 2\sqrt{3}\phi_0\phi_q^2 + 5\phi_q^3 - \Lambda\psi_q = 0, \\ &(\tau_\psi - 1 + 3\psi_0^2)\psi_q + 2\sqrt{3}\psi_0\psi_q^2 + 5\psi_q^3 - \Lambda\phi_q = 0. \end{aligned} \tag{4.20}$$

When either ϕ_q or ψ_q vanishes, one of the monolayers is in the disordered phase and the bilayer will be called the hexagonal-disordered (HD) phase or the disordered-hexagonal (DH) phase.

When the normal hexagonal phase in one leaflet is coupled to the inverted hexagonal phase in the other leaflet, it is energetically favorable to have a particular phase shift of

$2\pi/3$ between the two hexagonal structures. The order parameters which represent such a different type of hexagonal-hexagonal (HH*) phase can be written as

$$\phi_{\mathrm{H}}(\mathbf{r}) = \phi_0 + \frac{2\phi_q}{\sqrt{3}} \sum_{i=1}^{3} \cos(\mathbf{q}_i \cdot \mathbf{r}), \tag{4.21}$$

$$\psi_{\mathrm{H}^*}(\mathbf{r}) = \psi_0 + \frac{2\psi_q}{\sqrt{3}} \sum_{i=1}^{3} \cos(\mathbf{q}_i \cdot \mathbf{r} + \frac{2\pi}{3}). \tag{4.22}$$

The free energy density of the HH* phase is then obtained as

$$f_{\mathrm{HH}^*} = f_{\mathrm{H}}(\phi_0, \phi_q; \tau_\phi) + f_{\mathrm{H}}(\psi_0, \psi_q; \tau_\psi) - \Lambda(\phi_0\psi_0 - \phi_q\psi_q). \tag{4.23}$$

The conditions for the minimized amplitudes are

$$\begin{aligned} &2(\tau_\phi - 1 + 3\phi_0^2)\phi_q + 4\sqrt{3}\phi_0\phi_q^2 + 10\phi_q^3 + \Lambda\psi_q = 0, \\ &2(\tau_\psi - 1 + 3\psi_0^2)\psi_q + 4\sqrt{3}\psi_0\psi_q^2 + 10\psi_q^3 + \Lambda\phi_q = 0. \end{aligned} \tag{4.24}$$

Another combination which should be considered in the present model is the asymmetric case where one monolayer exhibits the striped phase and the other is the hexagonal phase. This striped-hexagonal (SH) phase is expressed as

$$\phi_{\mathrm{S}}(\mathbf{r}) = \phi_0 + 2\phi_q \cos(q^* x), \tag{4.25}$$

$$\psi_{\mathrm{H}}(\mathbf{r}) = \psi_0 + \frac{2\psi_q}{\sqrt{3}} \sum_{i=1}^{3} \cos(\mathbf{q}_i \cdot \mathbf{r}). \tag{4.26}$$

The free energy density of this SH phase is calculated to be

$$f_{\mathrm{SH}} = f_{\mathrm{S}}(\phi_0, \phi_q; \tau_\phi) + f_{\mathrm{H}}(\psi_0, \psi_q; \tau_\psi) - \Lambda\left(\phi_0\psi_0 + \frac{2}{\sqrt{3}}\phi_q\psi_q\right). \tag{4.27}$$

The conditions for the minimized amplitudes are

$$\begin{aligned} &(\tau_\phi - 1 + 3\phi_0^2)\phi_q + 3\phi_q^3 - \frac{\Lambda\psi_q}{\sqrt{3}} = 0, \\ &(\tau_\psi - 1 + 3\psi_0^2)\psi_q + 2\sqrt{3}\psi_0\psi_q^2 + 5\psi_q^3 + \frac{\Lambda\phi_q}{\sqrt{3}} = 0. \end{aligned} \tag{4.28}$$

The phase in which $\phi_{\rm S}$ and $\psi_{\rm H}$ in Eqs. (4.25) and (4.26) are interchanged with $\phi_{\rm H}$ and $\psi_{\rm S}$ is called the hexagonal-striped (HS) phase, and its free energy is obtained from the SH phase by noting the $\phi \leftrightarrow \psi$ symmetry. In addition to these phases, we have also taken into account the square-square (QQ) phase expressed by

$$\phi_{\rm Q}(\mathbf{r}) = \phi_0 + \frac{2\phi_q}{\sqrt{2}}\left[\cos(q^*x) + \cos(q^*y)\right], \tag{4.29}$$

$$\psi_{\rm Q}(\mathbf{r}) = \psi_0 + \frac{2\psi_q}{\sqrt{2}}\left[\cos(q^*x) + \cos(q^*y)\right]. \tag{4.30}$$

Then its free energy density is given by

$$f_{\rm QQ} = f_{\rm Q}(\phi_0, \phi_q; \tau_\phi) + f_{\rm Q}(\psi_0, \psi_q; \tau_\psi) - \Lambda\left(\phi_0\psi_0 + 2\phi_q\psi_q\right), \tag{4.31}$$

where

$$f_{\rm Q}(\phi_0, \phi_q; \tau) = \frac{\tau}{2}\phi_0^2 + \frac{1}{4}\phi_0^4 + (\tau - 1 + 3\phi_0^2)\phi_q^2 + \frac{9}{4}\phi_q^4. \tag{4.32}$$

The conditions for the minimized amplitudes are

$$\begin{aligned} &2(\tau_\phi - 1 + 3\phi_0^2)\phi_q + 9\phi_q^3 - 2\Lambda\psi_q = 0, \\ &2(\tau_\psi - 1 + 3\psi_0^2)\psi_q + 9\psi_q^3 - 2\Lambda\phi_q = 0. \end{aligned} \tag{4.33}$$

However, we will show below that this QQ phase cannot be more stable than the other phases.

By numerically solving Eqs. (4.15), (4.20), (4.24), (4.28) and (4.33) for a given set of $\phi_0, \psi_0, \tau_\phi, \tau_\psi, \Lambda$, we obtained the minimized amplitudes ϕ_q^* and ψ_q^* for the different phases. In Figs. 4.4 and 4.5, the minimized amplitudes for the decoupled bilayers are shown for each phase. Notice that for the stripe-stripe phase, $|\phi_q^*|$ and $|\psi_q^*|$ are presented since the signs are arbitrary (see Eq. (4.10)). We see that the amplitudes of the hexagonal structure have its preferred sign depending on the compositions.

In Figs. 4.6 and 4.7, the minimized amplitudes for the weakly coupled bilayers are shown for each phase. In the SH and HS phases, the signs of the amplitude of the

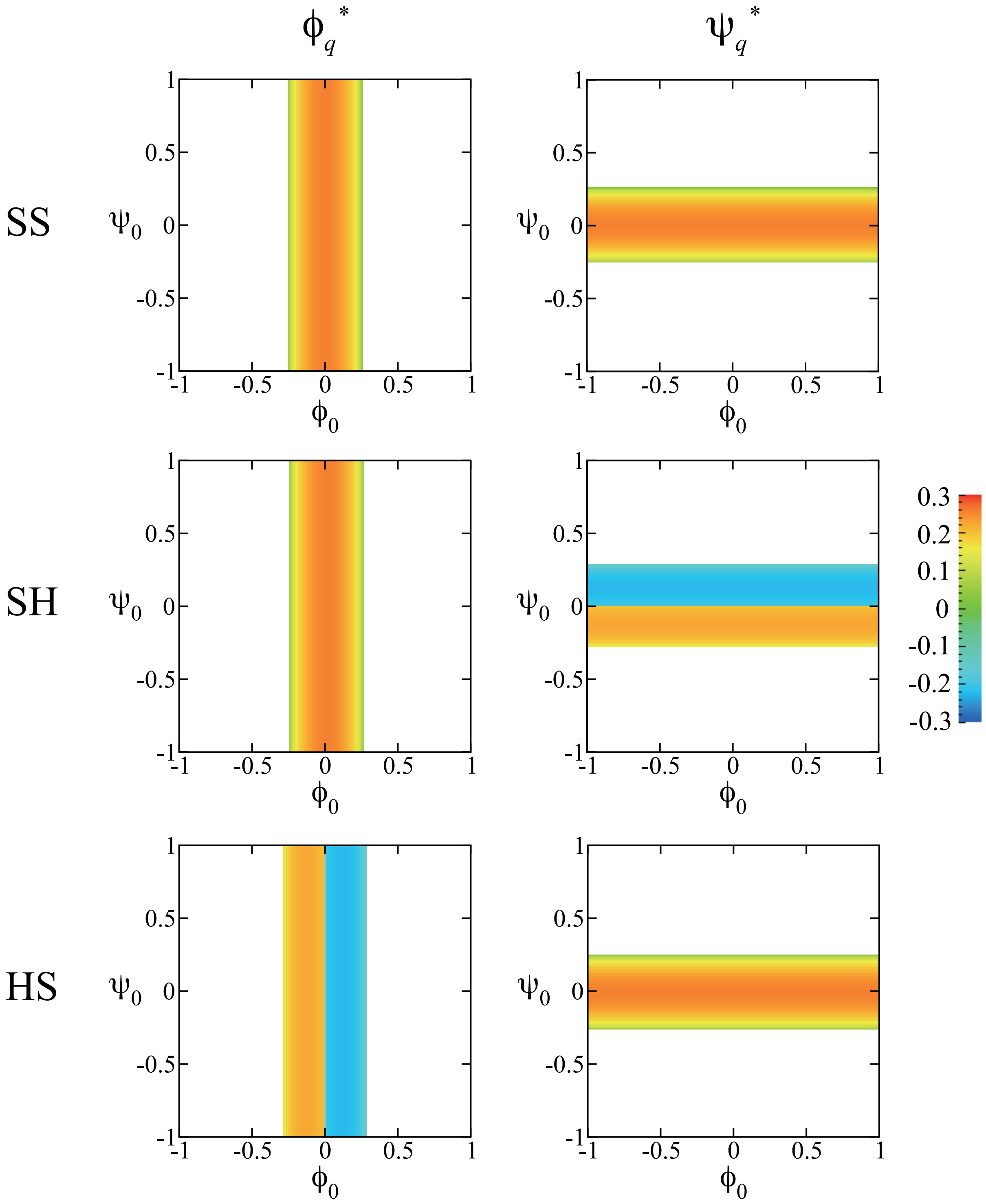

Figure 4.4: Minimized amplitudes (ϕ_q^* and ψ_q^*) for SS, SH, HS phases. Parameters are $\tau_\phi = \tau_\psi = 0.8, \Lambda = 0$. $|\phi_q^*|$ and $|\psi_q^*|$ are shown for SS phase.

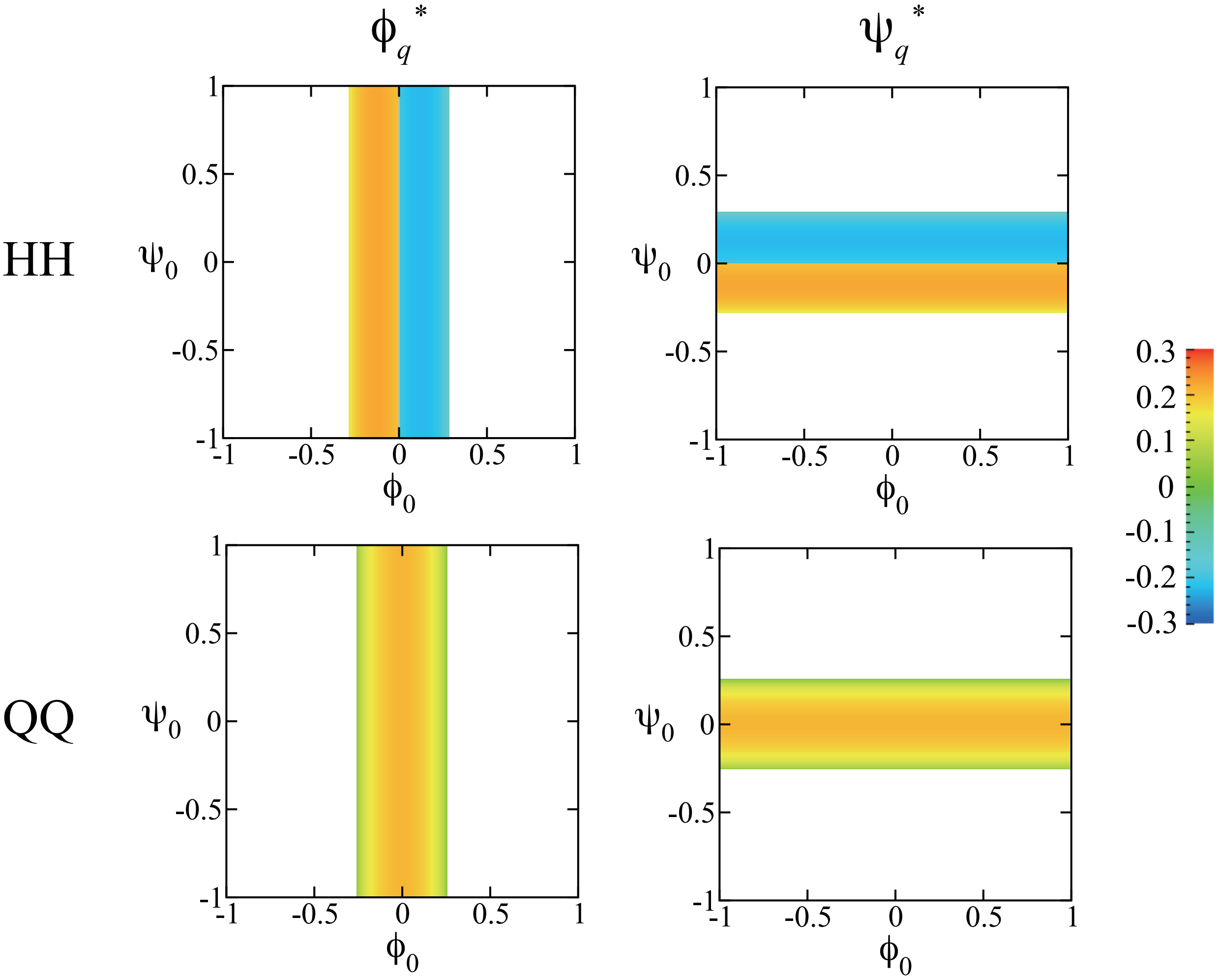

Figure 4.5: Minimized amplitudes (ϕ_q^* and ψ_q^*) for HH, QQ phases. Parameters are $\tau_\phi = \tau_\psi = 0.8, \Lambda = 0$.

hexagonal and the stripe phases are the same for any set of (ϕ_0, ψ_0). The signs of the amplitudes of the two monolayers of the HH and the HH* phases are opposite in the regions of $\phi_0\psi_0 < 0$. The absolute values of ϕ_q^* and ψ_q^* in HH* phase in that region are larger than that of the HH phase. This means that the concentration overlap between the monolayers in HH* phase is larger than that of the HH phase.

In Figs. 4.8 and 4.9, the minimized amplitudes for the strongly coupled bilayers ($\Lambda = 0.2$) are shown for each phase. We see that the region of the non-zero amplitude is expanded due to the large value of the coupling.

By substituting these amplitude values, the minimized free energies are calculated for each phase, and we obtain the phase diagram for the coupled bilayer. As a reference, we first show in Fig. 4.3(b) the phase diagram in the decoupled case $\Lambda = 0$ for $\tau = 0.8$. This can easily be obtained from Fig. 4.3(a) by combining its two cross-sections (one for ϕ_0 and one for ψ_0) at $\tau = 0.8$. Figure 4.10 gives the phase diagrams for a coupled bilayer when (a) $\Lambda = 0.02$, (b) $\Lambda = 0.05$, (c) $\Lambda = 0.15$ and (d) $\Lambda = 0.2$, while the temperature is fixed to $\tau = 0.8$. On the (ϕ_0, ψ_0)-plane, we have identified the phase which has the lowest energy, whereas possible phase coexistence regions between different phases have been ignored. All the boundary lines indicate first-order transitions. Since the free energy Eq. (2.18) is invariant under the exchange of $\phi \leftrightarrow \psi$, the phase diagrams are symmetric about the diagonal line $\phi_0 = \psi_0$ as the upper and lower leaflets have been chosen arbitrarily. These phase diagrams are also symmetric under the rotation of 180 degrees around the origin because Eq. (2.18) is invariant (except the linear terms) under the simultaneous transformations of $\phi \to -\phi$ and $\psi \to -\psi$. This is reasonable as the labels of “S” or “H” for the two lipids have been assigned arbitrarily in the free energy Eq. (2.18). As a consequence, the phase diagrams are also symmetric about the diagonal line $\phi_0 = -\psi_0$. The symmetries with respect to both $\phi_0 = 0$ and $\psi_0 = 0$ in Fig. 4.3(b) for $\Lambda = 0$ are now broken because of the coupling between the two leaflets.

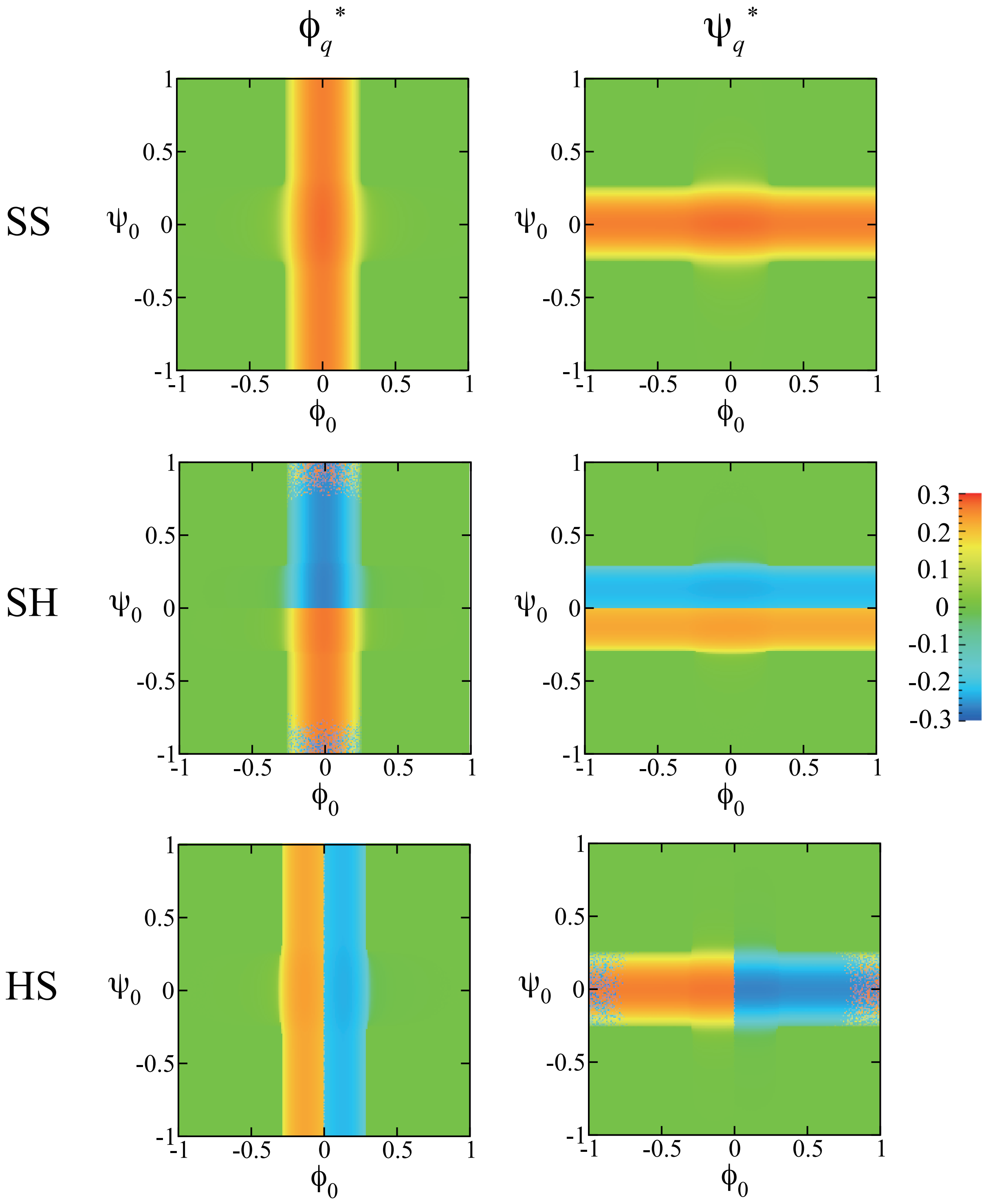

Figure 4.6: Minimized amplitudes (ϕ_q^* and ψ_q^*) for SS, SH, HS phases. Parameters are $\tau_\phi = \tau_\psi = 0.8, \Lambda = 0.02$. $|\phi_q^*|$ and $|\psi_q^*|$ are shown for SS phase.

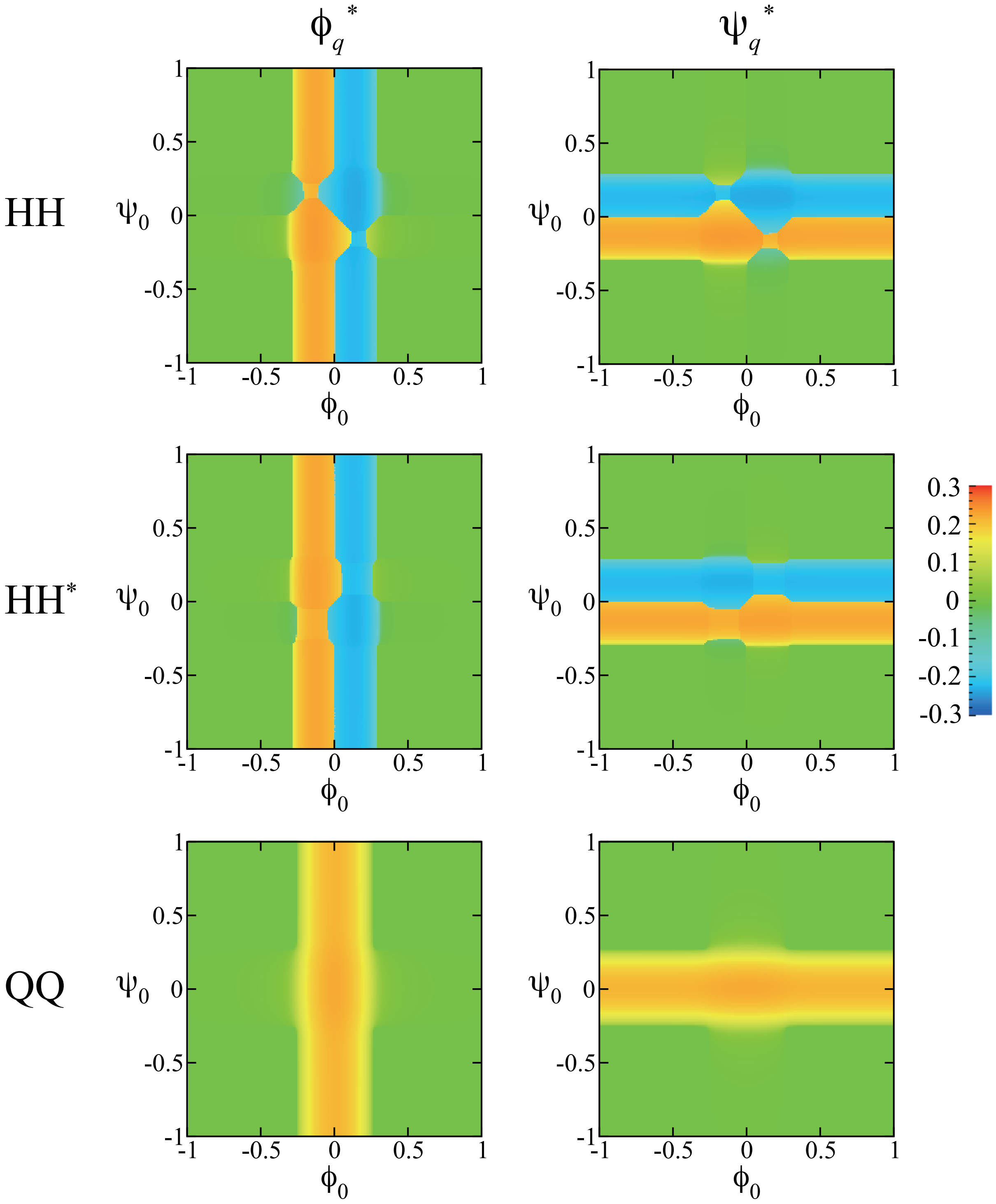

Figure 4.7: Minimized amplitudes (ϕ_q^* and ψ_q^*) for HH, HH*, QQ phases. Parameters are $\tau_\phi = \tau_\psi = 0.8, \Lambda = 0.02$.

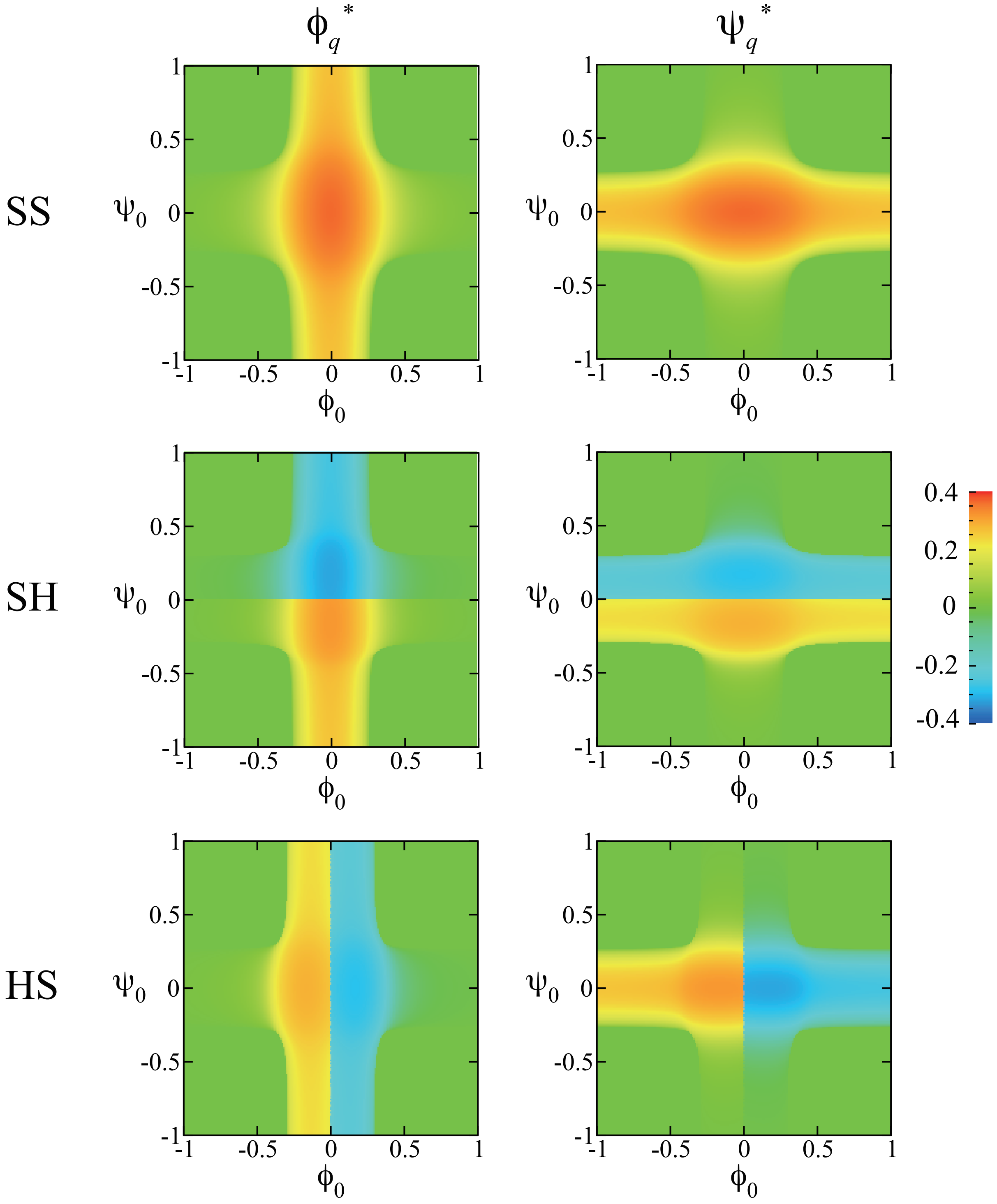

Figure 4.8: Minimized amplitudes (ϕ_q^* and ψ_q^*) for SS, SH, HS phases. Parameters are $\tau_\phi = \tau_\psi = 0.8, \Lambda = 0.2$. $|\phi_q^*|$ and $|\psi_q^*|$ are shown for SS phase.

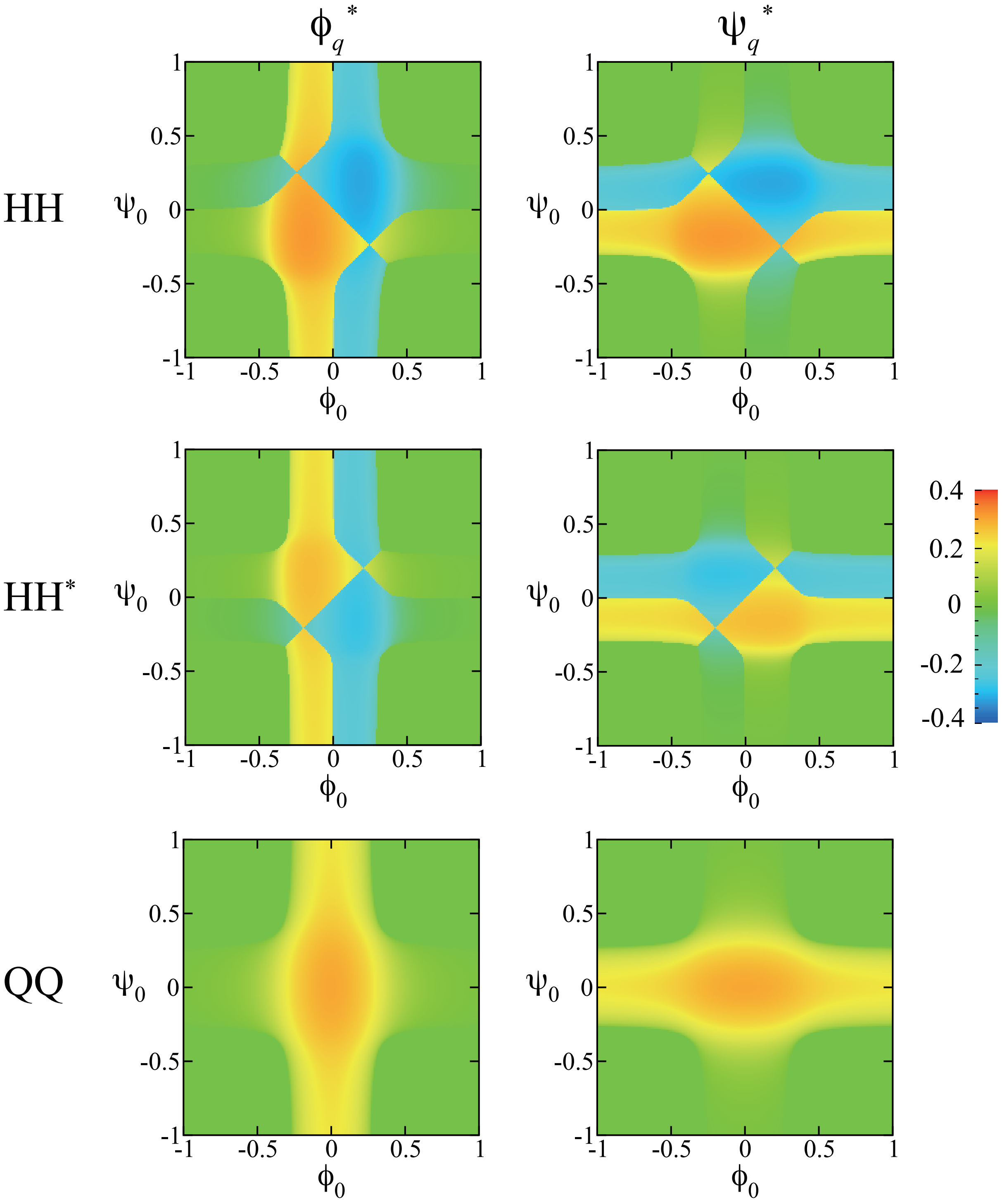

Figure 4.9: Minimized amplitudes (ϕ_q^* and ψ_q^*) for HH, HH*, QQ phases. Parameters are $\tau_\phi = \tau_\psi = 0.8, \Lambda = 0.2$.

When the coupling parameter is small (a, $\Lambda = 0.02$), the global topology of the phase diagram resembles that of the uncoupled case presented in Fig. 4.3(b). Close to the origin, $\phi_0 = \psi_0 = 0$, there is a region of SS phase surrounded by eight other phases: two SH, two HS, two HH, and two HH* phases. The HH phase appearing in the region of $\phi_0 < 0$ and $\psi_0 < 0$ is the combination of the two inverted hexagonal structures on each monolayer. One sees that the HH* phase appears in the regions of $\phi_0\psi_0 < 0$, where the hexagonal and the inverted hexagonal structures are coupled to each other.

A remarkable feature of this phase diagram is the existence of the SS and HH phases in the regions where either $|\phi_0|$ or $|\psi_0|$ are large. These outer SS and HH phases extend up to the maximum or the minimum values of the compositions. These regions of the SS and HH phases with $\Lambda > 0$ roughly correspond to those of the SD (DS) and HD (DH) phases, respectively, in Fig. 4.3(b) with $\Lambda = 0$. Hence the modulated structure in one of the monolayers induces the same modulated phase in the other monolayer due to the coupling term. Notice that the SD (DS) phase and HD (DH) phase do not exist in Fig. 4.10(a). We further remark that the extent of the four DD phase regions is almost unaffected by the coupling. Even when the temperature is lowered by decreasing τ, only the phases located close to the origin ($\phi_0 = \psi_0 = 0$) would expand, and the global topology does not change substantially.

When the coupling parameter is slightly increased (b, $\Lambda = 0.05$), the region of the SH and HS phases are decreased, whereas that of the HH* phase is unchanged. On the other hand, the area of the SS and HH phases are increased.

When the coupling becomes larger (c, $\Lambda = 0.15$), the five regions of the SS phase merge together forming one single continuous SS region. The four HH regions are still distinct and separate the SS region from four DD phase regions. Small fractions of the HH* phase remain.

For the largest value of the coupling parameter (d, $\Lambda = 0.2$), all the phases have symmetric combinations such as SS or HH phases. The asymmetric combination such as the SH phase does not appear, because the large coupling parameter strongly prefers symmetric phases of equal modulations in the two monolayers, although the ϕ_q and ψ_q amplitudes of the two modulated monolayers are not the same in the stripe SS phase (or the hexagonal HH phase). As the value of Λ is increased from 0.02 to 0.2, firstly the SH phase disappears, and then the HH* phase disappears.

When the value of Λ is further increased as shown in Fig. 4.11, the regions of the SS and HH phases expand on the expense of the DD phase regions. Finally we remark that the QQ phase was never found to be more stable than any of the other phases considered above.

Although we have so far assumed that Λ is positive, the phase diagrams for $\Lambda < 0$ can be easily obtained from those for $\Lambda > 0$ by rotating them by 90 degrees around the origin. This is because the free energy Eq. (2.18) is invariant under the simultaneous transformations of either $\phi \to -\phi$ and $\Lambda \to -\Lambda$, or $\psi \to -\psi$ and $\Lambda \to -\Lambda$.

When the temperatures in the two monolayers are different, the phase diagrams are shown in Fig. 4.12. Due to the lower temperature in the ϕ-monolayer, the area of the ordered phases is increased compared with that in Fig. 4.10. Similar to Fig. 4.10, the asymmetric phases vanish when the value of the coupling is large. Although the phase diagrams are symmetric about the rotation of 180 degrees around the origin, it is not symmetric about the diagonal line $\phi_0 = \psi_0$ because the free energy Eq. (2.18) is not invariant under the exchange of $\phi \leftrightarrow \psi$ when $\tau_\phi \neq \tau_\psi$. The symmetry about the diagonal line $\phi_0 = -\psi_0$ is also broken.

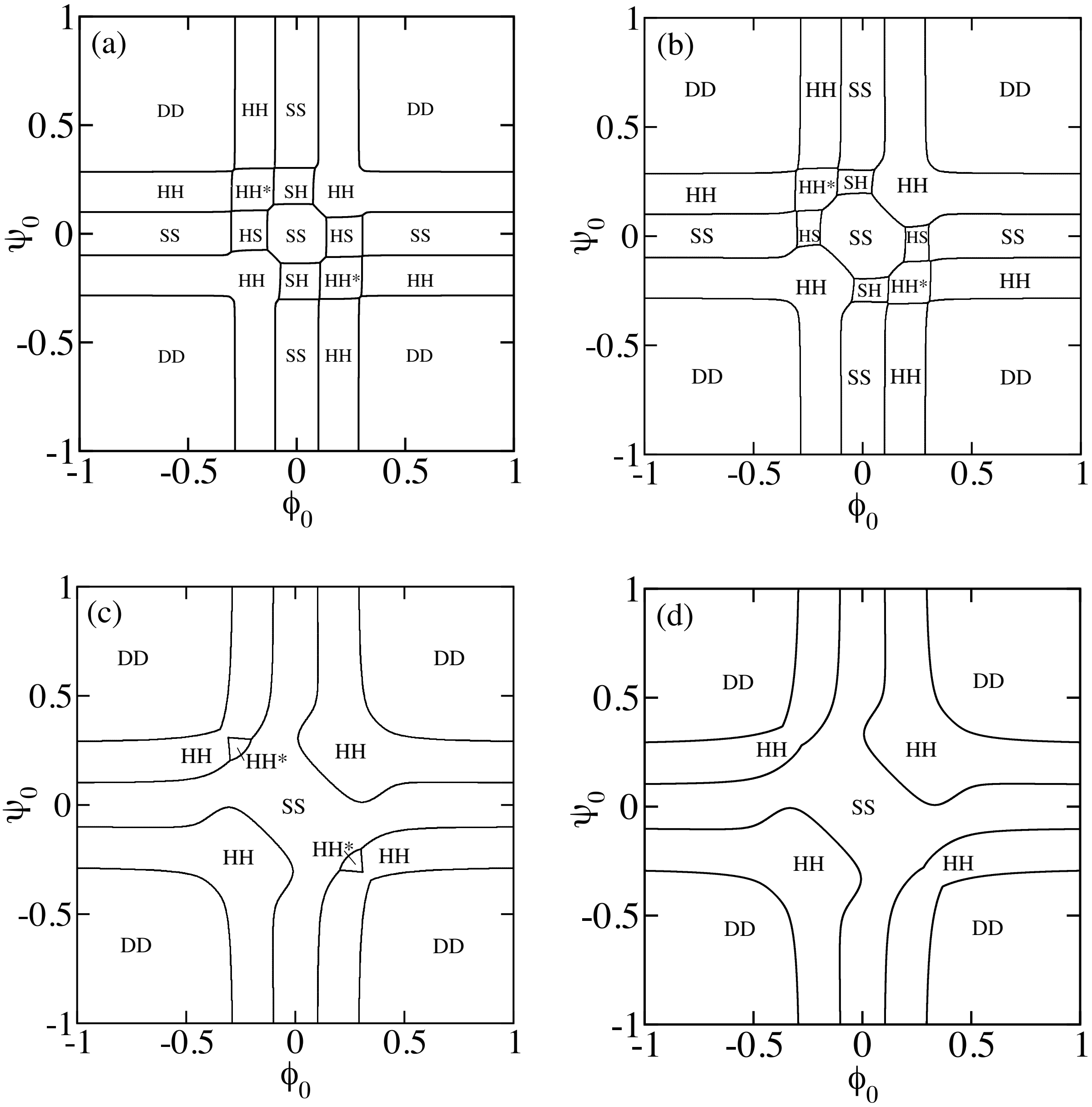

Figure 4.10: Mean-field phase diagram of coupled modulated bilayers for $\tau_\phi = \tau_\psi = 0.8$. ϕ_0 and ψ_0 are the average compositions in the two leaflets. The coupling parameter is chosen to be (a) $\Lambda = 0.02$, (b) $\Lambda = 0.05$, (c) $\Lambda = 0.15$ and (d) $\Lambda = 0.2$. The notations of the different phases are described in the text (see Sec. 4.1.2). All the phases are separated by first-order transition lines. The phase diagram is symmetric with respect to the two principal diagonals $\phi_0 = \psi_0$ and $\phi_0 = -\psi_0$, as described in the text.

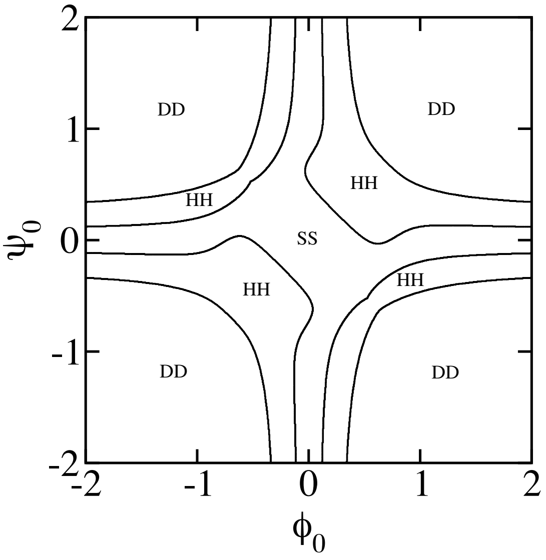

Figure 4.11: Mean-field phase diagram of coupled modulated bilayers for $\tau_\phi = \tau_\psi = 0.8$ and $\Lambda = 1$. ϕ_0 and ψ_0 are the average compositions in the two leaflets.

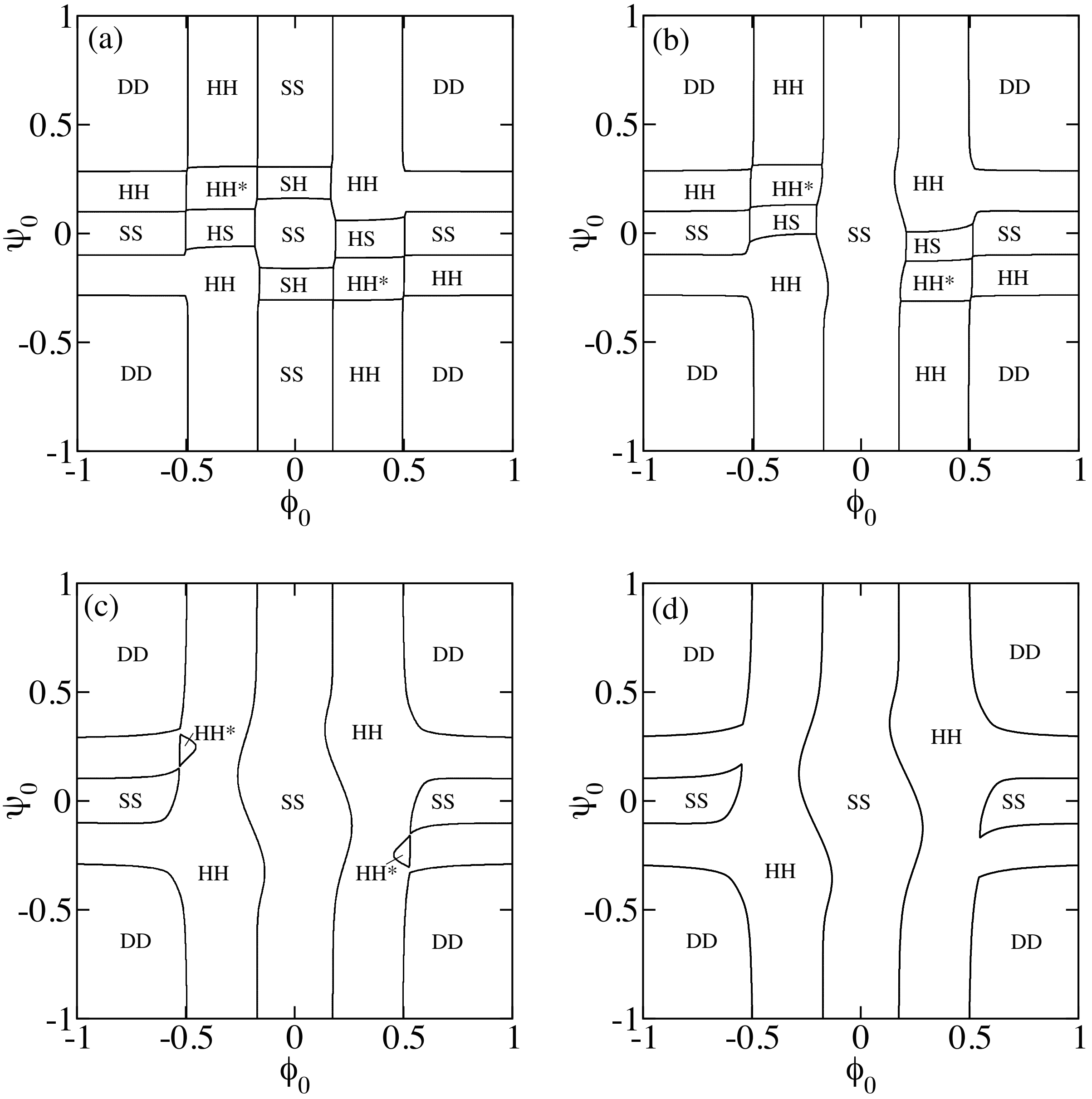

Figure 4.12: Mean-field phase diagram of coupled modulated bilayers for $\tau_\phi = 0.4, \tau_\psi = 0.8$. ϕ_0 and ψ_0 are the average compositions in the two leaflets. The coupling parameter is chosen to be (a) $\Lambda = 0.02$, (b) $\Lambda = 0.05$, (c) $\Lambda = 0.15$ and (d) $\Lambda = 0.2$.

4.1.3 Dynamics

Here we discuss the dynamics of phase separation of coupled modulated bilayers. In order to investigate the phase separation dynamics of the bilayers, we consider the following time evolution equations

$$\frac{\partial \phi}{\partial t} = L_\phi \nabla^2 \frac{\delta F_\mathrm{b}}{\delta \phi}, \tag{4.34}$$

$$\frac{\partial \psi}{\partial t} = L_\psi \nabla^2 \frac{\delta F_\mathrm{b}}{\delta \psi}. \tag{4.35}$$

Both ϕ and ψ are conserved order parameters in each of the monolayer (model B in the Hohenberg-Halperin classification [51]). Using the free energy functional, the above equations become

$$\frac{\partial \phi}{\partial t} = L_\phi \nabla^2 [4B(\nabla^4 \phi) + 4A(\nabla^2 \phi) + \tau_\phi \phi + \phi^3 - \Lambda \psi], \tag{4.36}$$

$$\frac{\partial \psi}{\partial t} = L_\psi \nabla^2 [4D(\nabla^4 \psi) + 4C(\nabla^2 \psi) + \tau_\psi \psi + \psi^3 - \Lambda \phi]. \tag{4.37}$$

For simplicity, the kinetic coefficients L_ϕ and L_ψ are taken to be unity, and both the hydrodynamic effect and thermal fluctuations are neglected.

We solve the above equations numerically in 2D using the periodic boundary condition. Each simulation starts from a disordered state with a small random noise around the average compositions ϕ_0 and ψ_0. The source code for solving the kinetic equations is shown in Appendix D. We will show the spatial patterns of ϕ, ψ, $\phi + \psi$, $\phi - \psi$ and the Fourier transformed pattern of ψ. The pattern of $\phi + \psi$ can be directly observed in the experiment on Montal-Mueller bilayers using fluorescence microscopy [36]. Time is measured in discrete time steps, and $t = 5,000$ corresponds to a well equilibrated system. In almost all the simulations below, the temperatures are fixed to be $\tau_\phi = \tau_\psi = 0.8$, and the characteristic wavenumber in ϕ-monolayer (when $\Lambda = 0$) is fixed as $q^*_\phi = 1/\sqrt{2}$ with $B = A = 1$. The periodicity in ψ-monolayer is given by $q^*_\psi = \sqrt{C/2D}$. We assume that the both monolayers have the same amplitudes of the modulation when $\Lambda = 0$, which requires the condition $C^2/D = 1$.

Here we discuss the phase separation patterns of the bilayer with the same characteristic wavenumber in each monolayer ($D = C = 1$, $q_\phi^* = q_\psi^*$). As a demonstration, we show the snapshots of the phase separation process of the bilayer which consists of two striped monolayers when $\Lambda = 0.02$ in Fig. 4.13. Starting from the isotropic state (a), both of the monolayers start to segregate (b), and form stripes (c). After a long time of annealing and reconnection, well aligned stripes are obtained (d). As time evolves, the mismatch between the two stripes $\phi - \psi$ decreases due to the coupling. Finally these morphologies overlap completely and the $\phi - \psi$ field almost vanishes.

In Fig. 4.14, the phase separated patterns with various combinations of the compositions are shown. For the comparison, the pattern shown in Fig. 4.13(d) is reproduced in Fig. 4.14(a). Similarly, the phase separated patterns of the HH phase is shown in Fig. 4.14(b). The coupling between the hexagonal phase with $\phi_0 = 0.2$ and the stripe phase with $\psi_0 = 0$ is shown in Fig. 4.14(c). The hexagonal and the stripe morphologies overlap in phase in order to reduce the concentration mismatch between the two structures. Figure 4.14(d) illustrates the coupling between the hexagonal phase with $\phi_0 = 0.2$ and the inverted hexagonal phase with $\psi_0 = -0.2$. This combination yields the HH* phase as seen from the pattern of $\phi + \psi$ where the two hexagonal structures are superimposed. These calculated morphologies are consistent with the phase diagram of Fig. 4.10(a) obtained according to the mean-field analysis. In Fig. 4.14(e), the patterns of a coupled bilayer with $\phi_0 = 0.5$ (no phase separation occurs in the decoupled case) and $\psi_0 = 0$ are shown. Here the finite coupling induces the modulation of the ϕ-monolayer, as expected from the phase diagram of Fig. 4.10(d). In Fig. 4.14(f), the patterns with $\phi_0 = -0.3$ and $\phi_0 = 0.3$ are shown. The phase shifted hexagonal phase is obtained, this result is not consistent with the mean field phase diagram of the bilayer shown in Fig. 4.10(d) in which the HH phase is expected to appear. In the $\phi - \psi$ pattern, we see that the hexagonal pattern is more distorted than that of the Fig. 4.14(d). This implies that the frustration between the monolayers is larger. Further increase of the coupling parameter ($\Lambda = 1$) in the region of the HH phase with $\phi_0\psi_0 < 0$, the square morphology is obtained (not shown). Notice that the patterns obtained via solving dynamical equations may not be well equibrated. In order to clarify the discrepancy, other minimization method for the patterns such as the conjugate gradient method should be tested in the future.

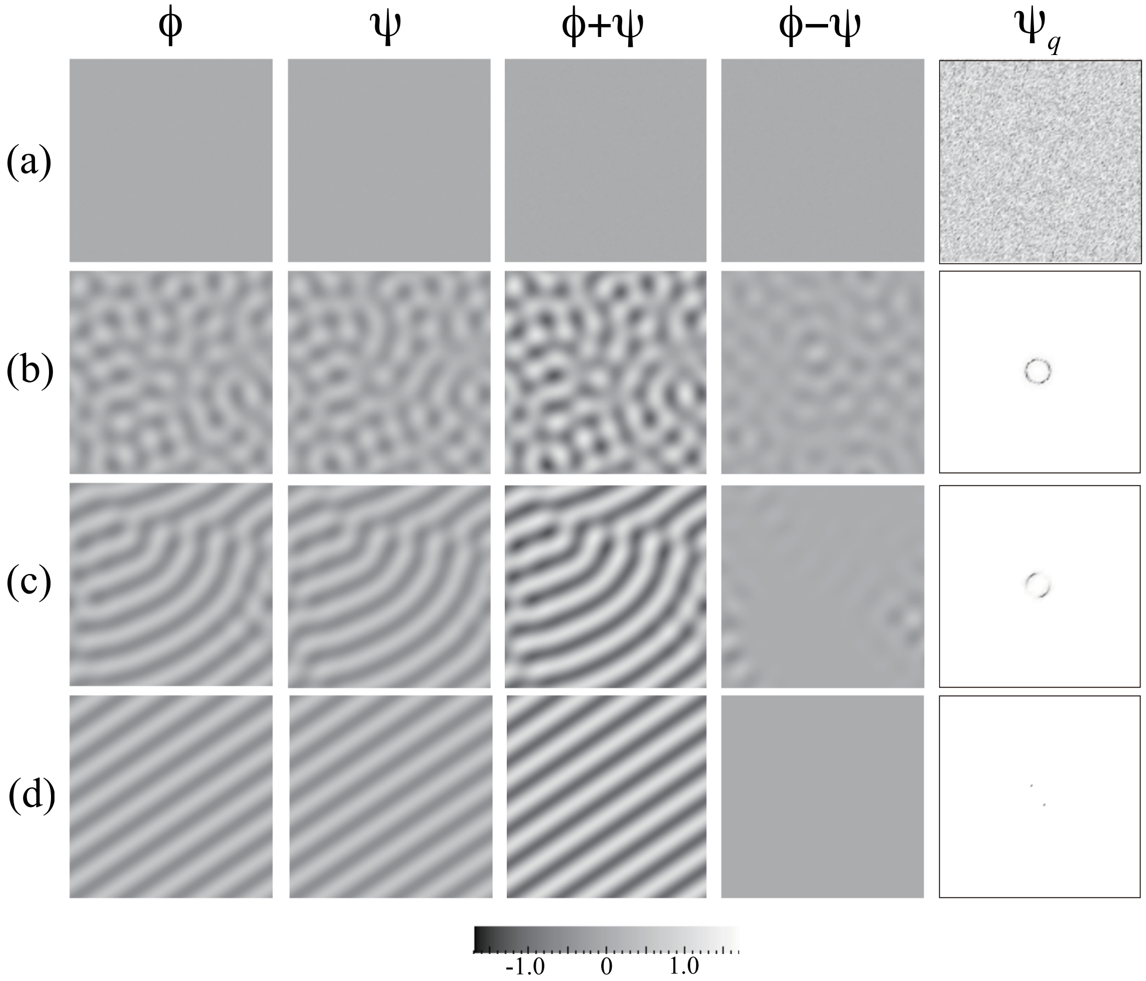

Figure 4.13: Time evolution of the phase separation in the coupled bilayer, which consists of striped monolayers with same periodicity. Patterns in ϕ, ψ monolayers, $\phi+\psi$, $\phi-\psi$, and Fourier space patterns of ψ-monolayers ψ_q are presented. (a) $t=0$, (b) $t=60$, (c) $t=250$, (d) $t=5000$. The parameters are $\phi_0=\psi_0=0, \tau_\phi=\tau_\psi=0.8, B=A=D=C=1$ ($q^*_\phi = q^*_\psi = 1/\sqrt{2}$), $\Lambda=0.02$.

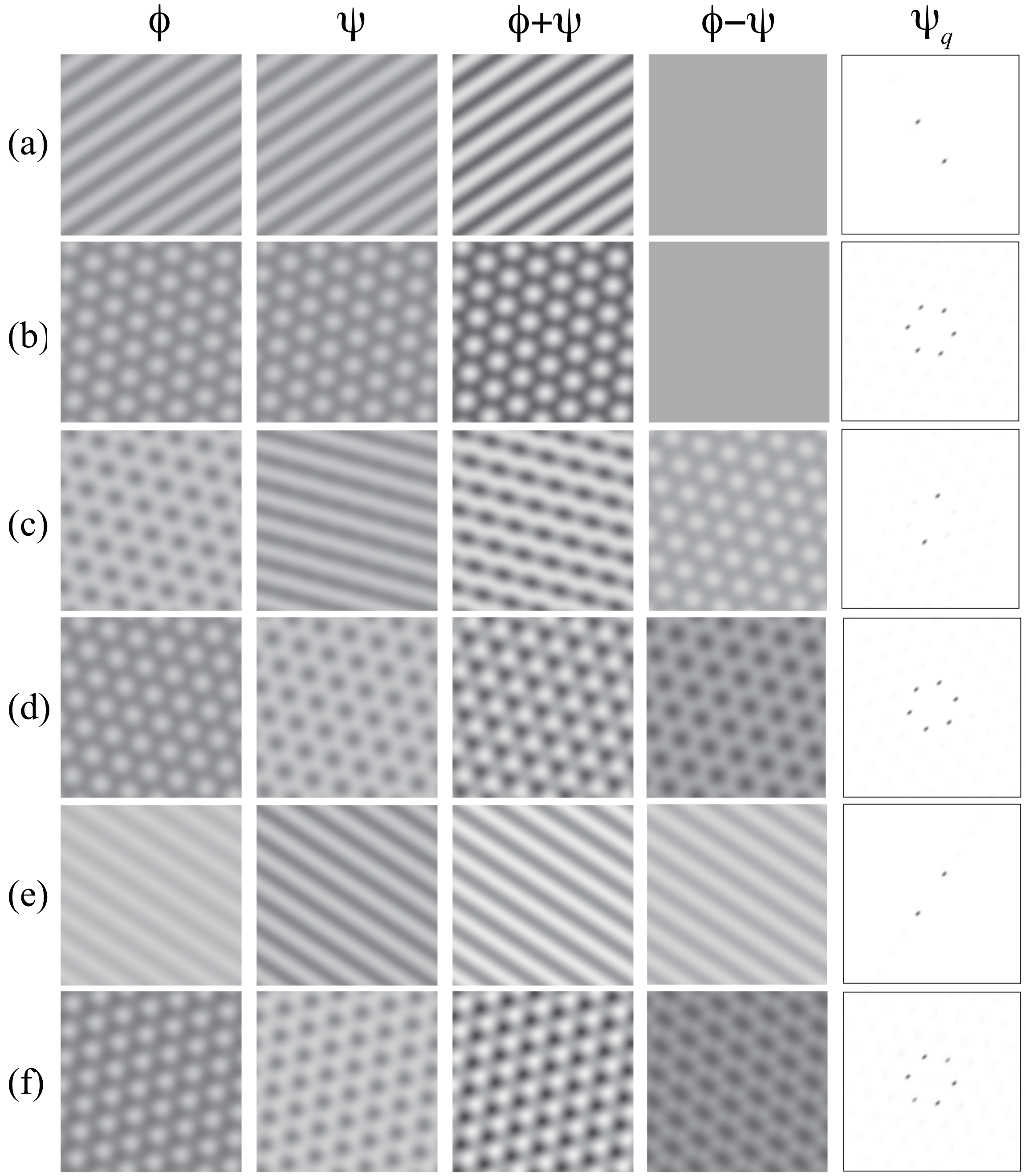

Figure 4.14: Phase separated patterns of coupled modulated bilayers for the same periodicity in the monolayers $B = A = D = C = 1(q^*_\phi = q^*_\psi = 1/\sqrt{2})$. The patterns of ϕ, ψ, $\phi+\psi$, $\phi-\psi$ and ψ_q obtained after long time simulation ($t = 5000$) are presented. The parameters chosen here are $\tau_\phi = \tau_\psi = 0.8$, (a) $\phi_0 = \psi_0 = 0, \Lambda = 0.02$, (b) $\phi_0 = -0.2, \psi_0 = -0.2, \Lambda = 0.02$, (c) $\phi_0 = 0.2, \psi_0 = 0, \Lambda = 0.02$, (d) $\phi_0 = -0.2, \psi_0 = 0.2, \Lambda = 0.02$, (e) $\phi_0 = 0.5, \psi_0 = 0, \Lambda = 0.2$, (f) $\phi_0 = -0.3, \psi_0 = 0.3, \Lambda = 0.2$.

4.2 Bilayers with different q^*

4.2.1 Phase separated patterns

When the characteristic wavenumbers of the monolayers are different, the two phase separated morphologies cannot overlap completely. Then the frustrations between the monolayers arise due to the coupling, which affects the phase separated patterns.

In Fig. 4.15, we show the snapshots of the phase separation process of the bilayer when the stripes of the monolayers have different periodicities, i.e, $q^*_\psi/q^*_\phi = 3$ and $\Lambda = 0.3$. Starting from the isotropic state (a), the ψ-monolayer first forms stripes (b), and then the ϕ-monolayer segregates and chops the stripes in the ψ-monolayer (c). Chopped stripe gradually transform to the finger like structure (d), and after a long time of annealing and reconnection of the stripes in the ϕ-monolayer (e), the pattern of alternating fingers in the ψ-monolayer is obtained (f). From the 2D Fourier patterns of the ψ-monolayer, it is clear that the intermediate patterns have two different lengths of modulations. The condition for the appearance of the intermediate structure is discusses below, and the detailed analysis of the phase separation process will be argued at the end of this section.

In Fig. 4.16 (a), (b), (c), we show the phase separated patterns ($t = 5000$) of the two stripes having different periodicities ($q^*_\psi/q^*_\phi = 3$) for various values of Λ. In the case of weak coupling (Fig. 4.16(a), $\Lambda = 0.1$), the two monolayers independently exhibit the stripe morphology. When the coupling constant is increased moderately (Fig. 4.16(b), $\Lambda = 0.3$), a stripe with finger-like structure appears in the ψ-monolayer, while the morphology in the ϕ-monolayer is unchanged. The structure with a larger periodicity dominates over that with a smaller periodicity. This tendency is in accordance with the properties of the static structure factor of the coupled bilayers having two different characteristic length of the fluctuations in each monolayer (Fig. 3.3). A stronger coupling leads to the similar morphologies both in ϕ- and ψ-monolayers (Fig. 4.16(c), $\Lambda = 0.5$). We can see that the

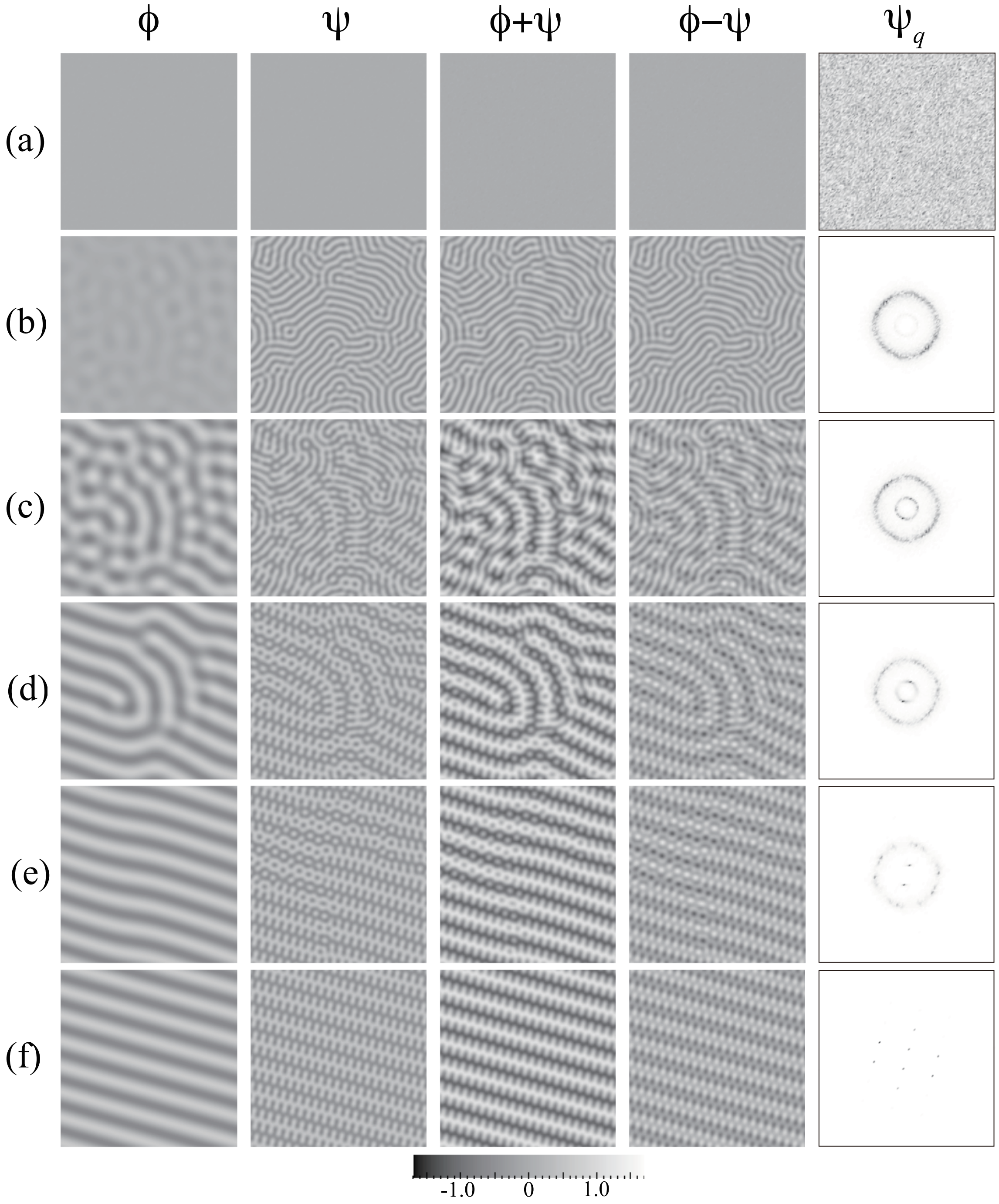

Figure 4.15: Time evolution of the phase separation in the coupled bilayer, which consists of striped monolayers with two different periodicity. Patterns in ϕ, ψ monolayers, $\phi+\psi$, $\phi-\psi$, and Fourier space patterns of ψ-monolayers are presented. (a) $t=0$, (b) $t=25$, (c) $t=60$, (d) $t=250$, (e) $t=1000$, (f) $t=5000$. The parameters are $\phi_0=\psi_0=0, \tau_\phi=\tau_\psi=0.8, B=A=1, D=0.0123, C=0.1111(q^*_\psi/q^*_\phi=3), \Lambda=0.3$.

inherent modulation in the ψ-monolayer is relatively weak (see the Fourier pattern ψ_q). Figure 4.16 (a)-(c) provides a typical sequence of the morphological changes of frustrated bilayers as Λ is increased. These three patterns are typically termed as “independent”, “intermediate”, and “coincident”, respectively.

In order to quantify the morphologies of these frustrated bilayers, we calculate the spatially averaged compositional correlation between the two monolayers defined by

$$\Delta = \left[\frac{1}{L^2} \int \mathrm{d}\mathbf{r} \, (\phi - \psi)^2 \right]^{1/2}, \tag{4.38}$$

where L is the system size. In Fig. 4.16(d), we plot this quantity as a function of Λ and q^*_ψ / q^*_ϕ. For each set of parameters, the value of Δ at $t = 1000$ is obtained from the simulation result. We consider that the simulation has almost reached the equilibrium by this time step (see also Fig. 4.27). The morphologies of the bilayers are categorized according to “independent”, “intermediate” and “coincident” patterns, as explained in the last paragraph. The value of Δ is large in the “independent” case, while it is small in the “coincident” case.

The spatially averaged correlation of the bilayers is defined as

$$\langle \phi\psi \rangle = \frac{1}{L^2} \int \mathrm{d}\mathbf{r} \ \phi\psi. \tag{4.39}$$

In Fig. 4.17, $\langle \phi\psi \rangle$ is shown as a function of Λ and q^*_ψ / q^*_ψ. The behavior of $\langle \phi\psi \rangle$ is similar to that of the peak value of the cross correlation $S_{\phi\psi}(q = q^*_{\phi\psi})$ shown in Fig. 3.9(a). Hence we can anticipate that the phase separated patterns are primarily determined by the cross correlation of the structure factor $S_{\phi\psi}$ between the two monolayers. It should be noted that the ordered pattern as in Fig. 4.16(b) can only be obtained with a rather specific choice of the parameters. In the “intermediate” region, the patterns with spots also appear in addition to the finger-like structure (see Fig. 4.15(d)).

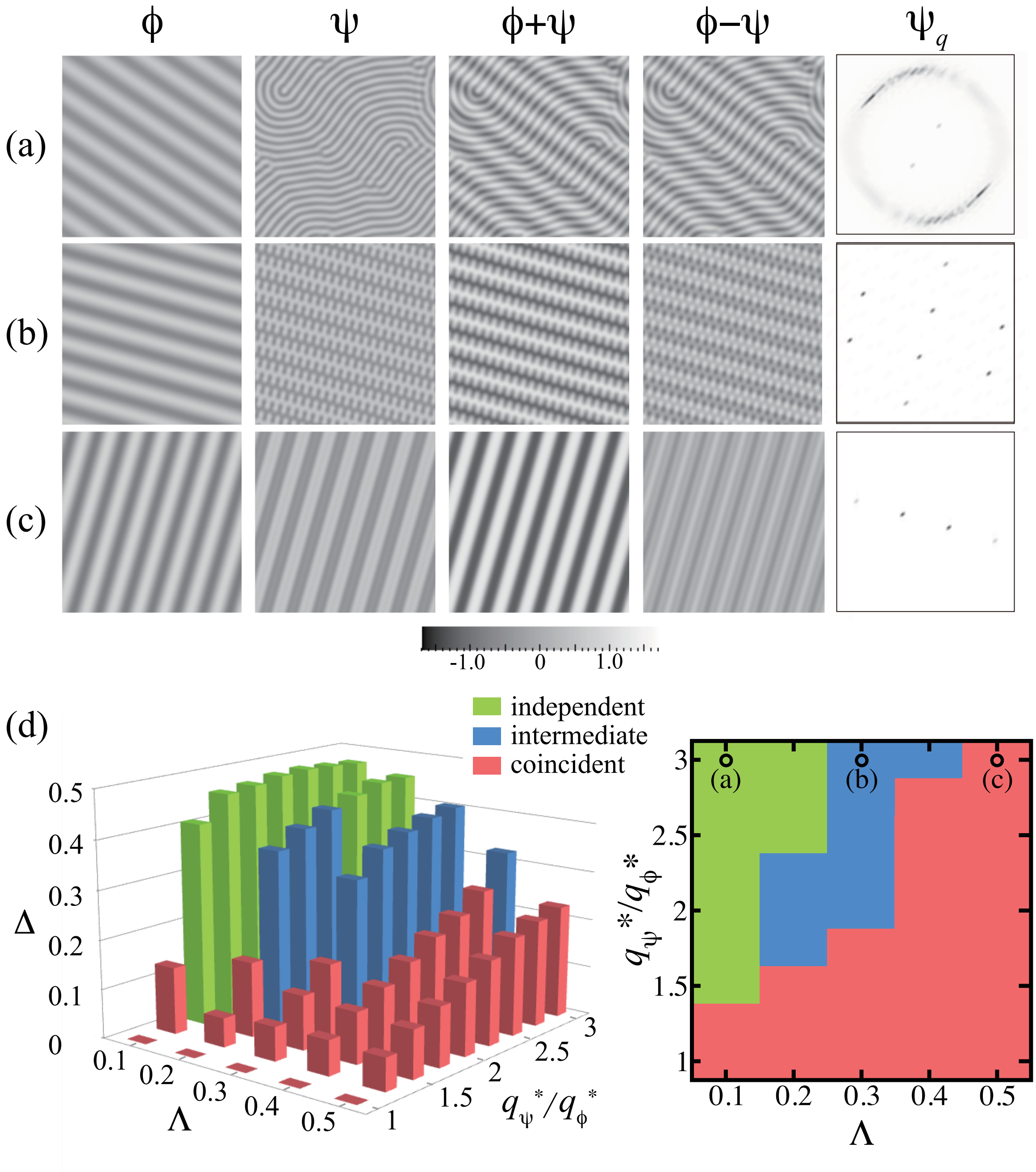

Figure 4.16: Patterns of coupled bilayers consisting of striped monolayers with two different periodicity ($\phi_0 = \psi_0 = 0, \tau_\phi = \tau_\psi = 0.8$). The patterns of ϕ, ψ, $\phi+\psi$, $\phi-\psi$ and ψ_q obtained after long time simulation ($t = 5000$) are presented. The parameters chosen here are $B = A = 1, D = 0.0123, C = 0.1111$ ($q^*_\psi/q^*_\phi = 3$), (a) $\Lambda = 0.1$, (b) $\Lambda = 0.3$, (c) $\Lambda = 0.5$. (d) Averaged degree of the overlap of the compositions between the monolayers $\Delta(t = 1000)$ of the two stripe coupled bilayers. We categorize the morphologies of the patterns into three, “independent”, “intermediate”, “coincident”.

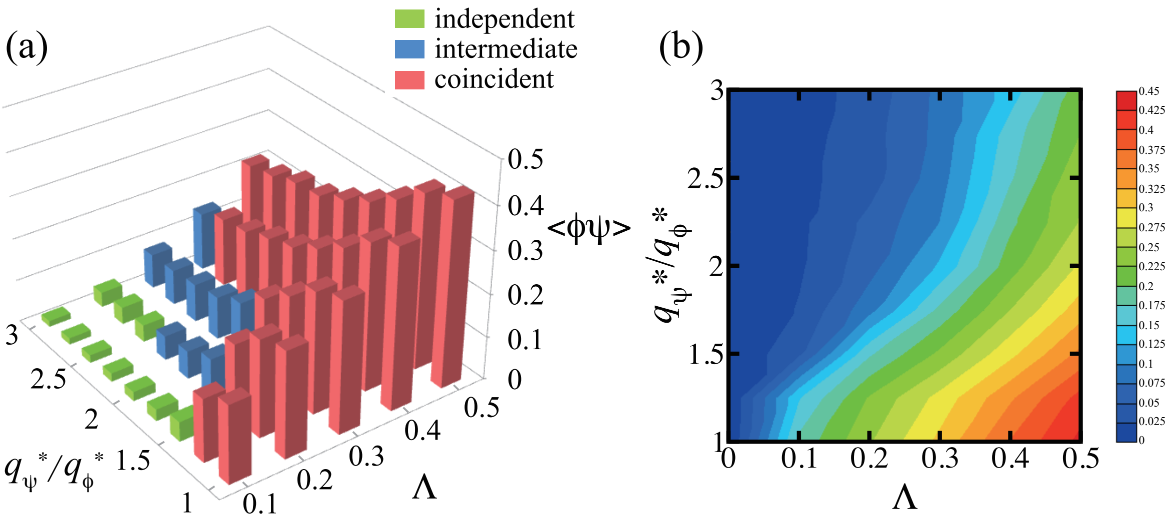

Figure 4.17: (a) Spatially averaged correlation of the compositions between the monolayers $\langle\phi\psi\rangle$ at $t = 1000$ for the two stripe coupled bilayer ($\phi_0 = \psi_0 = 0, \tau_\phi = \tau_\psi = 0.8, B = A = 1$, $C^2/D = 1$). (b) Contour plot of $\langle\phi\psi\rangle$.

In Fig. 4.18, we show the phase separated patterns of the bilayers when the stripe and the hexagonal structures are coupled. The latter structure has a smaller periodicity than the former one in the decoupled case. The patterns in Fig. 4.18(a) are the "independent" case in which the two monolayers independently exhibit the hexagonal and the stripe morphologies. In Fig. 4.18(b) and (d), the spots in the ψ-monolayer are aligned with the stripes in the ϕ-monolayer, and we call these as "aligned" patterns. In Fig. 4.18(c) and (e), the spots merged to produce the coinciding stripe structures. The pattern in Fig. 4.18(c) has a finger-like pattern similar to Fig. 4.16(b). The corresponding quantity Δ is plotted in Fig. 4.19. As explained above, the phase separated patterns are classified into three types; "independent", "aligned", "coincident". The intermediate "aligned" structure is obtained for the parameters between the "independent" and "coincident" regions.

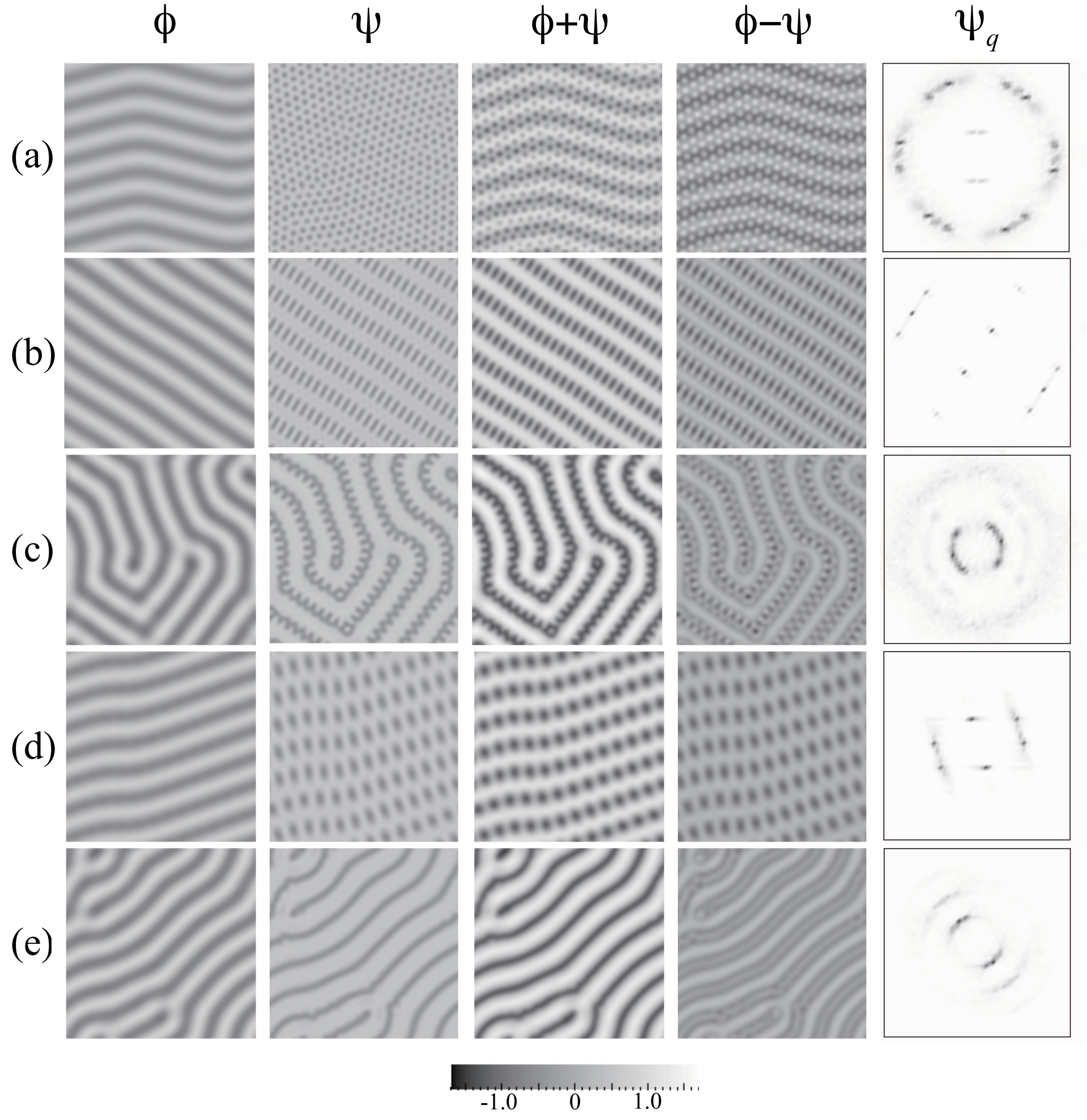

Figure 4.18: Patterns of the coupled bilayers consisting of stripe and hexagonal monolayers with different periodicity ($\phi = 0, \psi = 0.2, \tau_\phi = \tau_\psi = 0.8$, $B = A = 1$). (a) $D = 0.0123, C = 0.1111$ $(q^*_\psi/q^*_\phi = 3), \Lambda = 0.1$, (b) $D = 0.0123, C = 0.1111$ $(q^*_\psi/q^*_\phi = 3), \Lambda = 0.3$, (c) $D = 0.0123, C = 0.1111$ $(q^*_\psi/q^*_\phi = 3), \Lambda = 0.5$, (d) $D = 0.1066, C = 0.3265$ $(q^*_\psi/q^*_\phi = 1.75), \Lambda = 0.2$, (e) $D = 0.0256, C = 0.16$ $(q^*_\psi/q^*_\phi = 2.5), \Lambda = 0.4$.

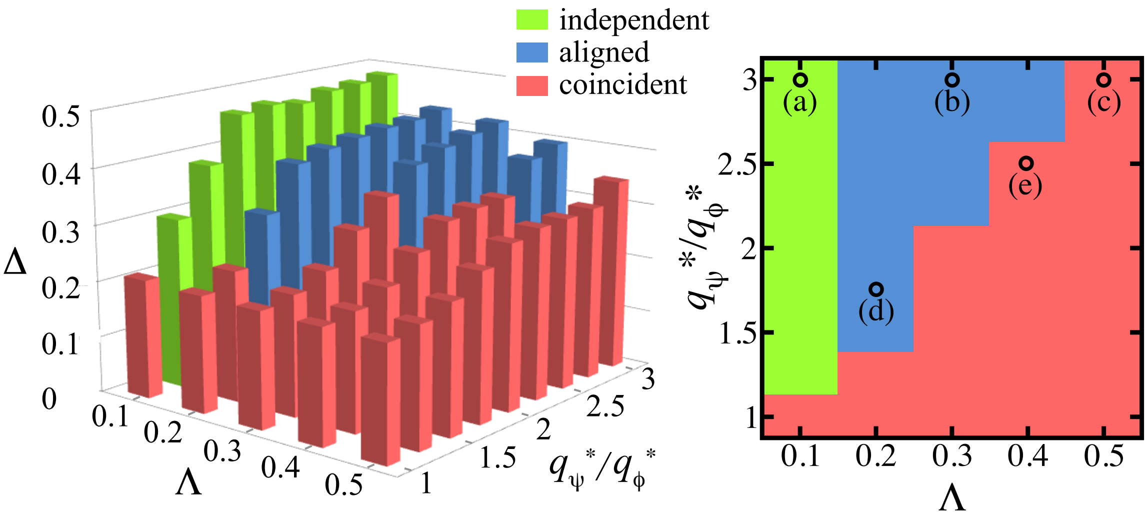

Figure 4.19: Averaged degree of the overlap of the compositions between the monolayers $\Delta(t = 1000)$ for stripe-hexagonal coupled bilayers ($\phi = 0, \psi = 0.2, \tau_\phi = \tau_\psi = 0.8$, $B = A = 1$). The categories are "independent", "intermediate", "coincident". Circle symbols in the right figure represent the parameters of the results as shown in Fig. 4.18(a,b,c,d,e).

When the periodicity of the stripe morphology is smaller than that of the hexagonal, the resulting morphology of the bilayers changes as shown in Fig. 4.20. The pattern in Fig. 4.20(a) is the "independent" case in which the two monolayers independently exhibit the hexagonal and the stripe morphologies. In Fig. 4.20(b), the stripe morphology in the ψ-monolayer is disturbed by the hexagonal spots in the ϕ-monolayer to yield the "chopped stripe" pattern. The pattern in Fig. 4.20(c) is termed as "spikes". In Fig. 4.20(d), the two coinciding "hexagonal" structures are obtained. The patterns in Fig. 4.20(e) and (f) are termed as "hexagonal-stripe" and "stripe", respectively. The quantity Δ is plotted in Fig. 4.21. As explained above, the phase separated patterns are classified into six types; "independent", "chopped stripe", "spikes", "hexagonal", "hexagonal-stripe" and "stripe". The last three patterns are the cases when the structures in the two monolayers coincide with each other. The intermediate structures such as "chopped stripe" and "spikes" are obtained for the parameters between the independent and the coincident regions.

For the "spike" case, an interesting sequence of the morphologies can be obtained as shown in Fig. 4.22(a), (b), (c). As the coupling strength and the wavenumber ratio increase, the number of spikes on the hexagonal spots also increase from three (a) to six (c). Such different spike domains are indeed observed in lipid monolayers both experimentally and theoretically [53], but the alignment of these spikes have not been observed. In the Fourier pattern of Fig. 4.22(c), there are spots at the intermediate wavenumbers between q^*_ϕ and q^*_ψ.

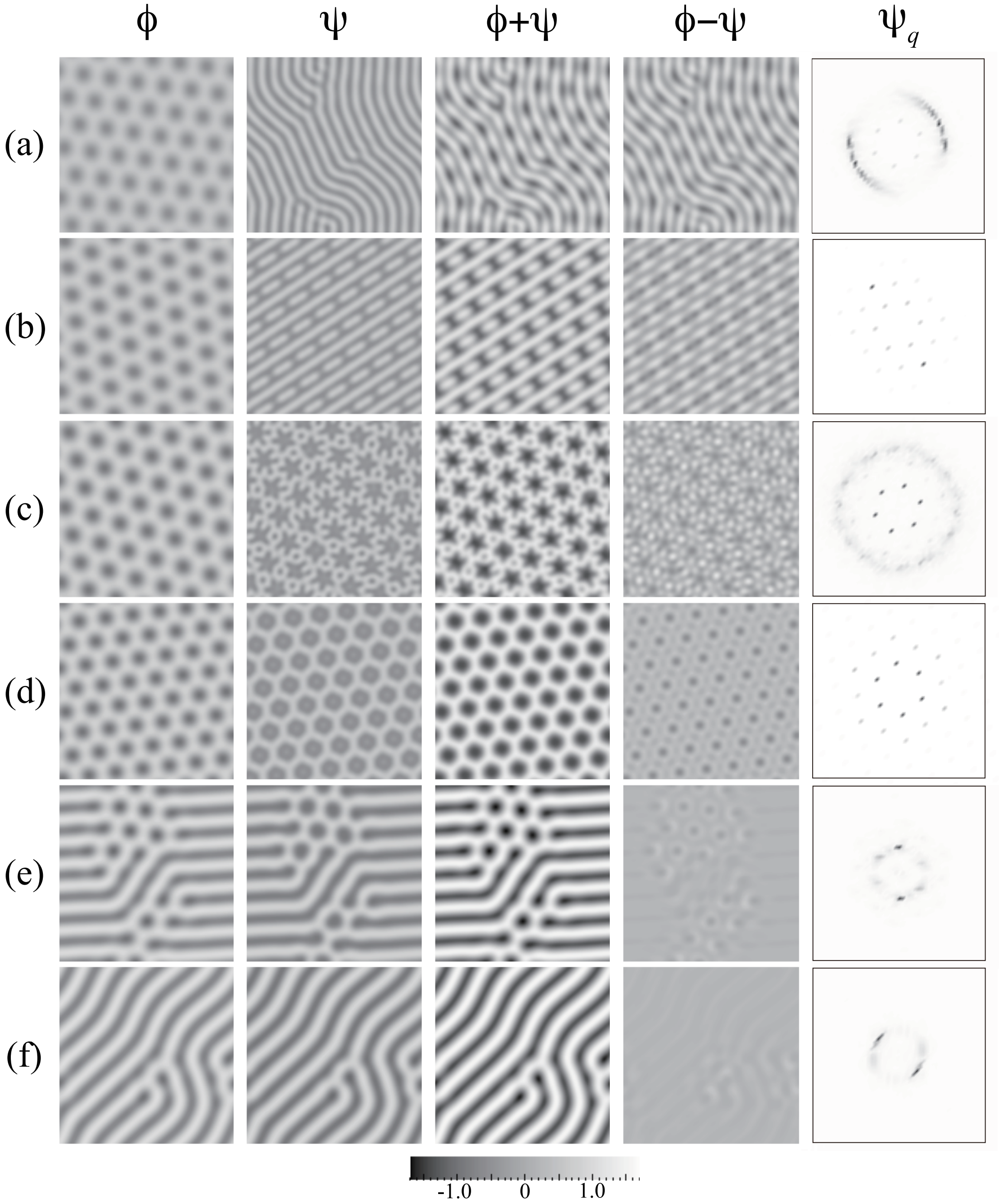

Figure 4.20: Patterns of the coupled bilayers consisting of hexagonal and striped monolayers with different periodicity ($\phi = 0.2, \psi = 0, \tau_\phi = \tau_\psi = 0.8$, $B = A = 1$, $t = 5000$). (a) $D = 0.0625, C = 0.25$ $(q^*_\psi/q^*_\phi = 2), \Lambda = 0.1$, (b) $D = 0.0625, C = 0.25$ $(q^*_\psi/q^*_\phi = 2), \Lambda = 0.25$, (c) $D = 0.0256, C = 0.16$ $(q^*_\psi/q^*_\phi = 2.5), \Lambda = 0.4$, (d) $D = 0.0625, C = 0.25$ $(q^*_\psi/q^*_\phi = 2), \Lambda = 0.4$, (e) $D = 0.0625, C = 0.25$ $(q^*_\psi/q^*_\phi = 2), \Lambda = 0.5$, (f) $D = 0.1975, C = 0.4444$ $(q^*_\psi/q^*_\phi = 1.5), \Lambda = 0.5$.

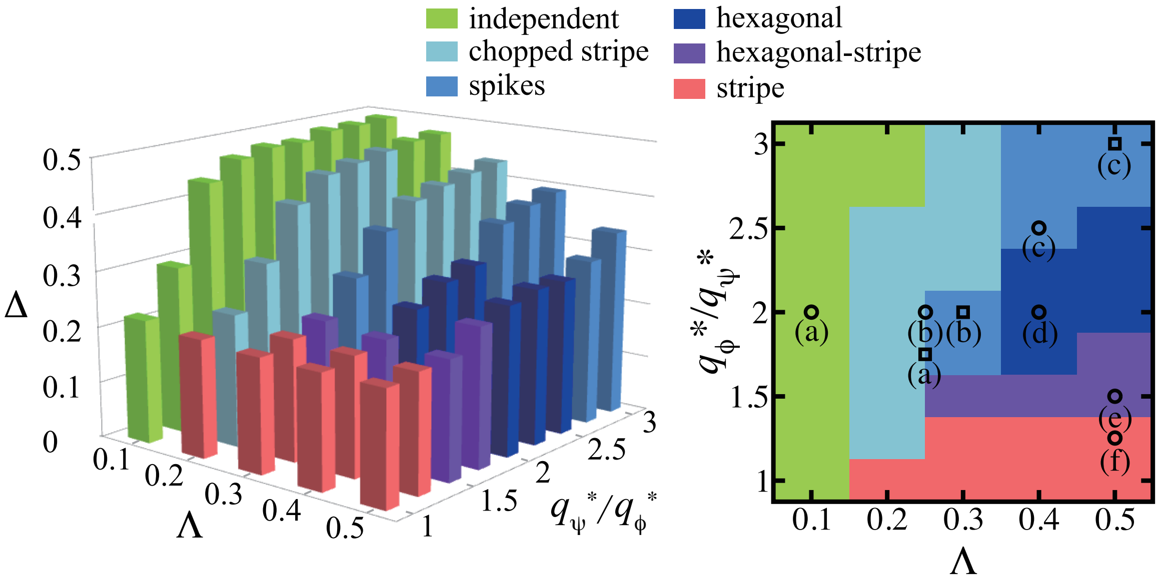

Figure 4.21: Averaged degree of the overlap of the compositions between the monolayers $\Delta(t = 1000)$ for the hexagonal-stripe coupled bilayers ($\phi = 0.2, \psi = 0, \tau_\phi = \tau_\psi = 0.8$, $B = A = 1$). The categories are “independent”, “chopped stripe”, “spikes”, “hexagonal”, “hexagonal-stripe”, “stripe”. Circle and square symbols in the right figure represent the parameters of the results as shown in Fig. 4.20(a,b,c,d,e,f) and Fig. 4.22(a,b,c), respectively.

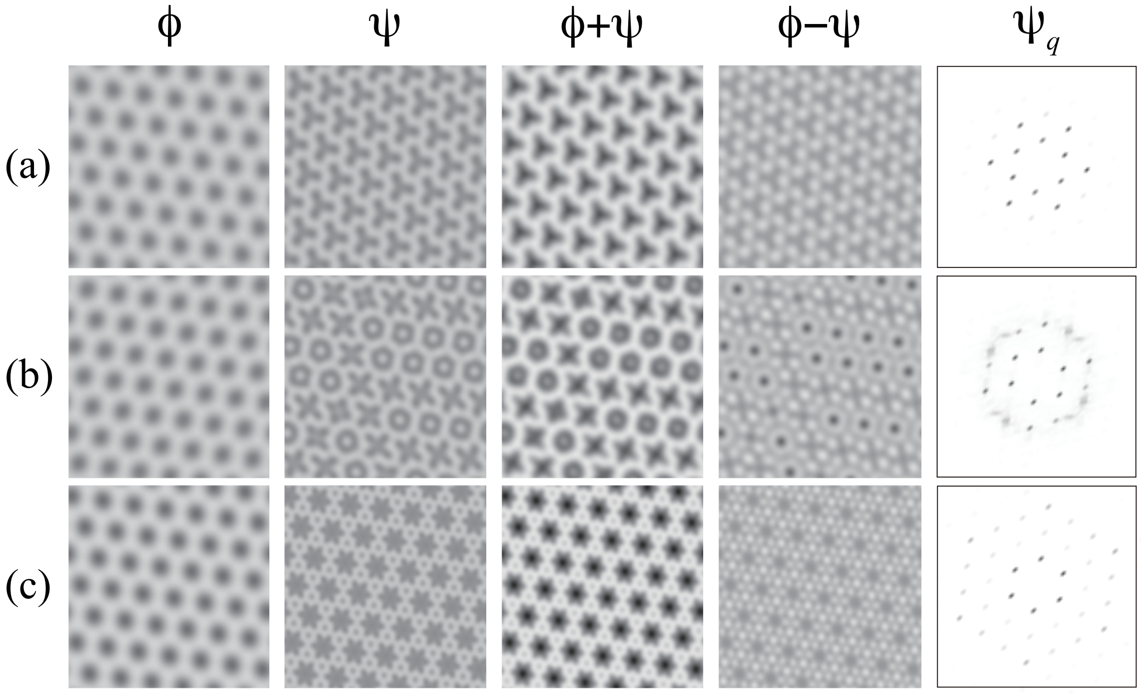

Figure 4.22: Patterns of the coupled bilayers consisting of hexagonal and striped monolayers ($\phi_0 = 0.2, \psi_0 = 0$, $\tau_\phi = \tau_\psi = 0.8$, $B = A = 1$, $t = 5000$). (a) $D = 0.1066, C = 0.3265$ ($q^*_\psi/q^*_\phi = 1.75$), $\Lambda = 0.25$, (b) $D = 0.0625, C = 0.25$ ($q^*_\psi/q^*_\phi = 2$), $\Lambda = 0.3$, (c) $D = 0.0123, C = 0.1111$ ($q^*_\psi/q^*_\phi = 3$), $\Lambda = 0.5$.

In Fig. 4.23, we show the phase separated patterns of the bilayers having two hexagonal structures with different periodicities in the decoupled case. The pattern in Fig. 4.23(a) is the "independent" case in which the two monolayers independently exhibit the two hexagonal morphologies. In Fig. 4.23(b) and (e), the hexagonal spots in the ψ-monolayer coalesce due to the hexagonal spots with larger periodicities in the ϕ-monolayer. This pattern is called as the "merged" case. In Fig. 4.23(c), the two coincident hexagonal structures are obtained. In the pattern of Fig. 4.23(d), the two coincident "stripe-hexagonal" structures are obtained. In Fig. 4.23(f), the "white eyes" structure emerges. In the study of the coupled diffusion reaction systems, the authors found a similar pattern originating from the "resonance" of the two interacting different wavelength modes [54].

The corresponding quantity Δ is plotted in Fig. 4.24. As explained above, the phase separated patterns are classified into five types; "independent", "merged", "coincident", "stripe-hexagonal" and "white eyes". The intermediate structures such as "merged" and "white eyes" are obtained between the "independent" and the "coincident" regions.

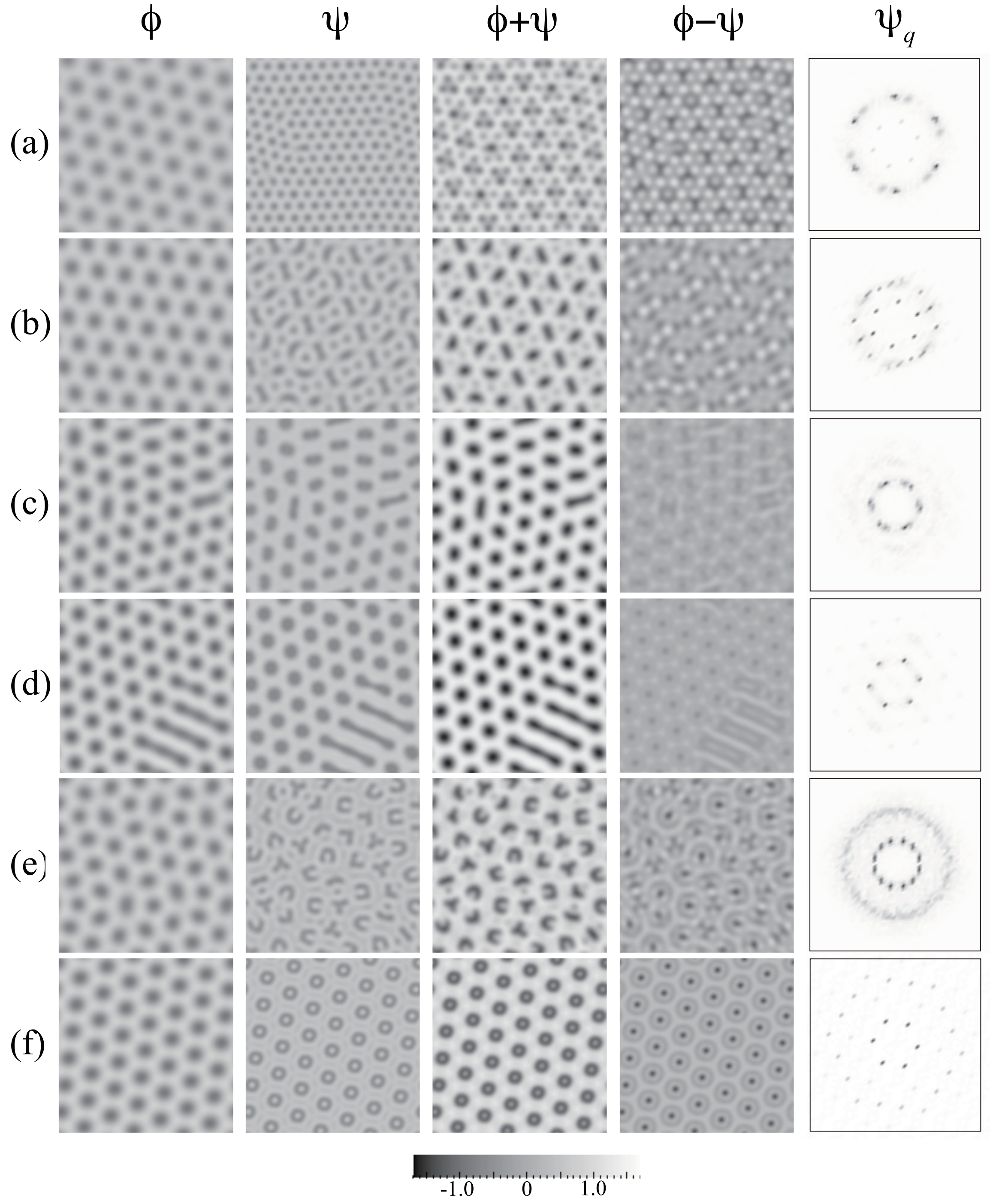

Figure 4.23: Patterns of the coupled bilayers consisting of two hexagonal monolayers with different periodicity ($\phi = 0.2, \psi = 0.2, \tau_\phi = \tau_\psi = 0.8$, $B = A = 1$). (a) $D = 0.0625, C = 0.25$ $(q^*_\psi/q^*_\phi = 2), \Lambda = 0.1$, (b) $D = 0.1066, C = 0.3265$ $(q^*_\psi/q^*_\phi = 1.75), \Lambda = 0.2$, (c) $D = 0.0625, C = 0.25$ $(q^*_\psi/q^*_\phi = 2), \Lambda = 0.4$, (d) $D = 0.0625, C = 0.25$ $(q^*_\psi/q^*_\phi = 2), \Lambda = 0.5$, (e) $D = 0.039, C = 0.1975$ $(q^*_\psi/q^*_\phi = 2.25), \Lambda = 0.3$, (f) $D = 0.0175, C = 0.1322$ $(q^*_\psi/q^*_\phi = 2.75), \Lambda = 0.4$.

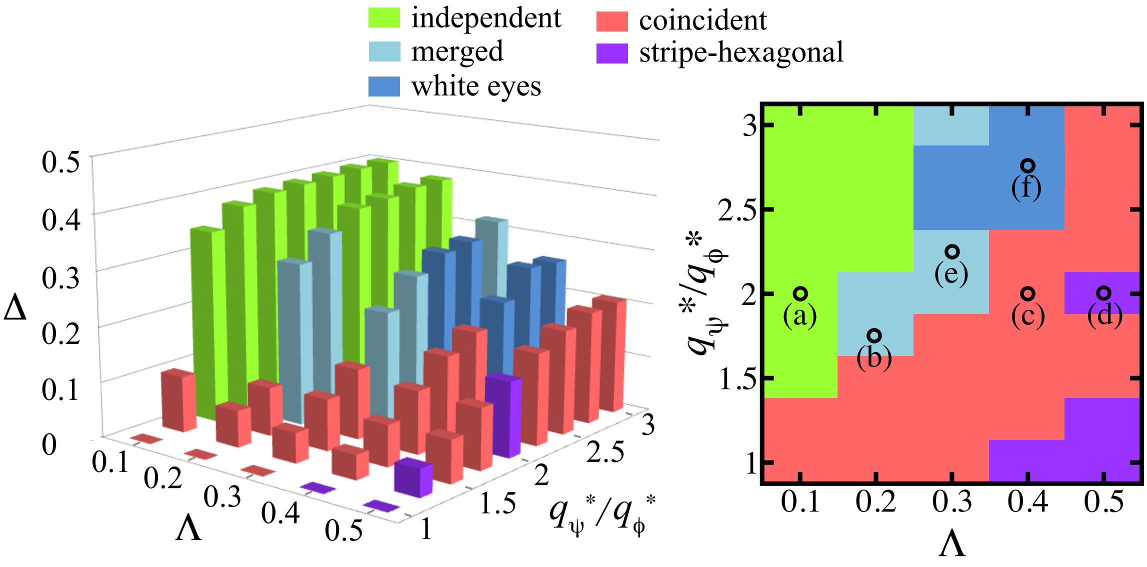

Figure 4.24: Averaged degree of the overlap of the compositions between the monolayers $\Delta(t = 1000)$ of the two hexagonal coupled bilayers ($\phi = 0.2, \psi = 0.2, \tau_\phi = \tau_\psi = 0.8$, $B = A = 1$). The categories are "independent", "merged", "white eyes", "stripe-hexagonal", "coincident". Circle symbols in the right figure represent the parameters of the results as shown in Fig. 4.23(a,b,c,d,e,f).

When the hexagonal and the inverted hexagonal are coupled, four different patterns appear, i.e., “independent”, “tiled”, “hexagonal-stripe” and “stripe”. Figure 4.25(a) is the “independent” case where the two hexagonal structures are independently superimposed. Figure 4.25(b) shows the “tiled” case in which the hexagonal spots with a smaller periodicity fill the gaps between the other hexagonal spots with a larger periodicity. In Fig. 4.25(c), a more complicated but ordered structure is obtained. In Fig. 4.25(d), we see that the pattern of the ϕ-monolayer corresponds to the “hexagonal-stripe” case. In Fig. 4.25(e), the two hexagonal structures merge to form the “stripe” morphology. The calculated Δ is presented in Fig. 4.26. The appearance of the “stripe” structure with the same parameter of the composition can be also seen in the phase diagram of the modulated bilayers (see Fig. 4.10).

It should be noted that although all of the above patterns are obtained after long time of simulations, we do not know whether these structures are in equilibrium or metastable. Many metastable states should exist because of the complexity of the frustrated bilayer systems. More detailed study on the stability of the structures is required.

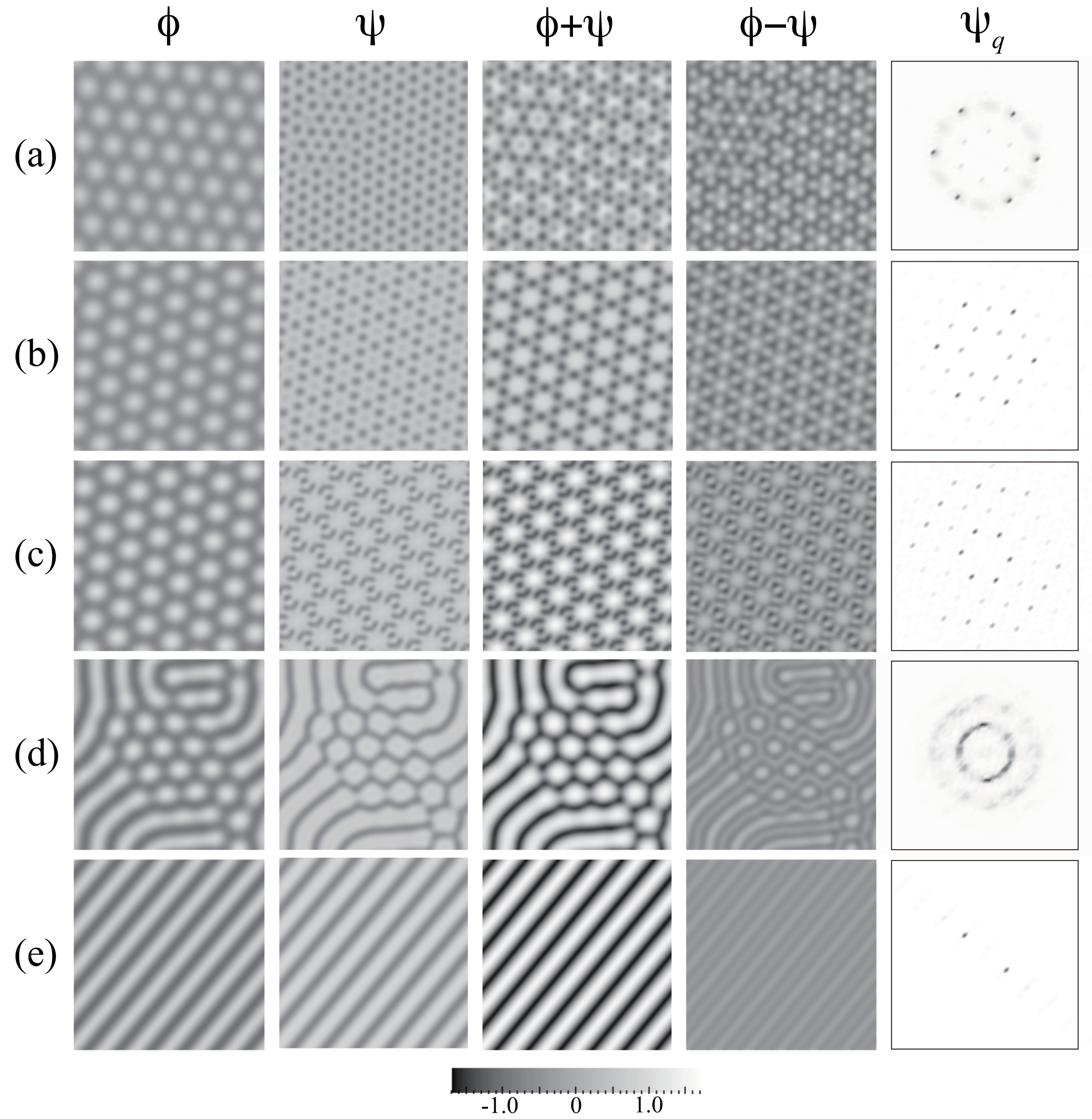

Figure 4.25: Patterns of the coupled bilayers consisting of two phase shifted hexagonal monolayers with different periodicity ($\phi = -0.2, \psi = 0.2$, $\tau_\phi = \tau_\psi = 0.8$, $B = A = 1$, $t = 5000$). (a) $D = 0.0625, C = 0.25$ $(q^*_\psi/q^*_\phi = 2), \Lambda = 0.1$, (b) $D = 0.0625, C = 0.25$ $(q^*_\psi/q^*_\phi = 2), \Lambda = 0.2$, (c) $D = 0.0175, C = 0.1322$ $(q^*_\psi/q^*_\phi = 2.75), \Lambda = 0.47$, (d) $D = 0.0625, C = 0.25$ $(q^*_\psi/q^*_\phi = 2), \Lambda = 0.5$, (e) $D = 0.1975, C = 0.4444$ $(q^*_\psi/q^*_\phi = 1.5), \Lambda = 0.5$.

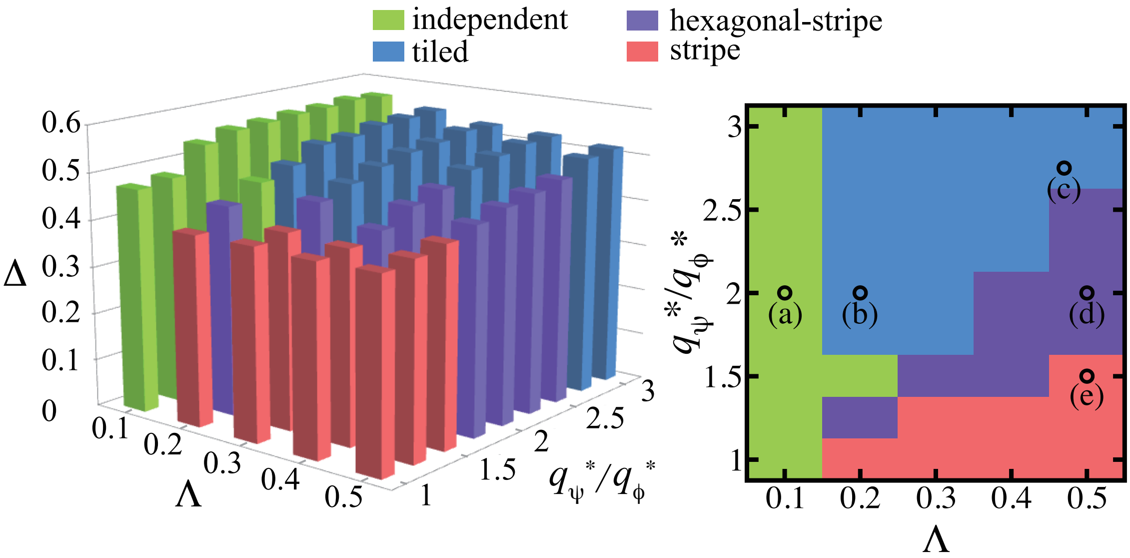

Figure 4.26: Averaged degree of the overlap of the compositions between the monolayers $\Delta(t = 1000)$ for the phase shifted hexagonal coupled case ($\phi = -0.2, \psi = 0.2$, $\tau_\phi = \tau_\psi = 0.8$, $B = A = 1$). The categories are "independent", "tiled", "hexagonal-stripe", "stripe". Circle symbols in the right figure represent the parameters of the results as shown in Fig. 4.25(a,b,c,d,e).

4.2.2 Dynamics

In Fig. 4.27, the time course of Δ is plotted for the cases presented in Fig. 4.16 (a)-(c). As a reference, Δ for the symmetric bilayer is also plotted. The value increases around $t = 50$ and decreases to zero. Finally these two stripes coincide completely (see Fig. 4.13(d)). In the case of the different wavenumber ratio, Δ ($t > 1000$) of the equibrated bilayers remains finite. As the coupling Λ increases, Δ decreases. Up to $t = 20$, the three lines of Δ increase similarly, but they evolve differently for $t > 20$.

Next we plot in Fig. 4.28(a) the time evolutions following quantities

$$\langle\phi^2\rangle^{1/2} = \left[\frac{1}{L^2}\int \mathrm{d}\mathbf{r}\phi^2\right]^{1/2}, \ \langle\psi^2\rangle^{1/2} = \left[\frac{1}{L^2}\int \mathrm{d}\mathbf{r}\psi^2\right]^{1/2}. \tag{4.40}$$

The parameters are the same as used in Fig. 4.16 (a)-(c). We see that, in all the cases, the modulation with larger wavenumber in the ψ-monolayer grows faster than that with smaller wavenumber in the ϕ-monolayer. We also see that the structure formation occurs in the ϕ-monolayers around $t = 20$. This corresponds to the time when the value of Δ begins to exhibit the difference mentioned in Fig. 4.27. This result can be understood within the linear stability analysis of the bilayer. By linearizing Eqs. (4.36) and (4.37) of the concentration evolution, the initial growth of the concentration is expressed as $\phi_q \sim \exp[\kappa_\pm t]$, where $\kappa_\pm$ are the growth rates obtained analytically (see Appendix C for details). The initial growth rates of the unstable modes are essentially given by $\omega_\pm$ in Eq. (3.63) which are the decay rates of the concentration fluctuations. We plot the growth rates as a function of the wavenumber q in Fig. 4.28(b) in which there are two peaks. The growth rate at the peak of larger q is larger than that of smaller q. A similar feature also exists in Fig. 3.12 showing the decay rate of the concentration fluctuations (see Fig. 3.12). We have mentioned that fluctuations of smaller wavenumber persist longer than those of larger wavenumber. When Λ is increased, the growth rate at smaller q increases. This is because the coupling effectively reduces the temperature so that the driving force for the phase separation becomes stronger. In accord with the linear stability analysis, we see in Fig. 4.28(a) that the onset time for the phase separation becomes shorter in the ϕ-monolayer as the coupling parameter is increased. In summary, the properties of concentration fluctuations above the transition temperature reflect those of the phase separation below the transition temperature.

Finally, the phase separated patterns when the two monolayers have different temperatures are shown in Fig. 4.29. In the ψ-monolayer, a spot like structure emerges along the stripe of the upper monolayer. The appearance of the spot structure may reflect the higher temperature in the ψ-monolayer. For a monolayer in the stripe phase with $\phi_0 \neq 0$, a phase transition to the hexagonal phase occurs by increasing the temperature (see Fig. 4.3).

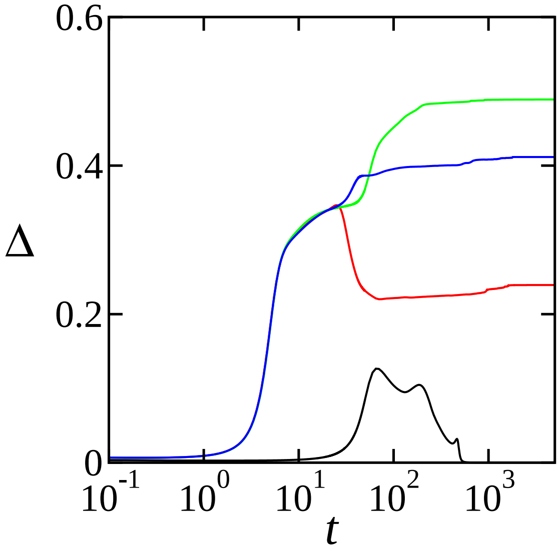

Figure 4.27: Time evolution of the difference of the composition Δ for $\Lambda = 0.1$ (green), $\Lambda = 0.3$ (blue) and $\Lambda = 0.5$ (red). Other parameters are $\tau_\phi = \tau_\psi = 0.8, \phi_0 = \psi_0 = 0$, $B = A = 1, D = 0.0123, C = 0.1111$ $(q^*_\psi/q^*_\phi = 3)$. The parameter for the black line is $\Lambda = 0.02$, $B = A = D = C = 1$ $(q^*_\psi/q^*_\phi = 1)$.

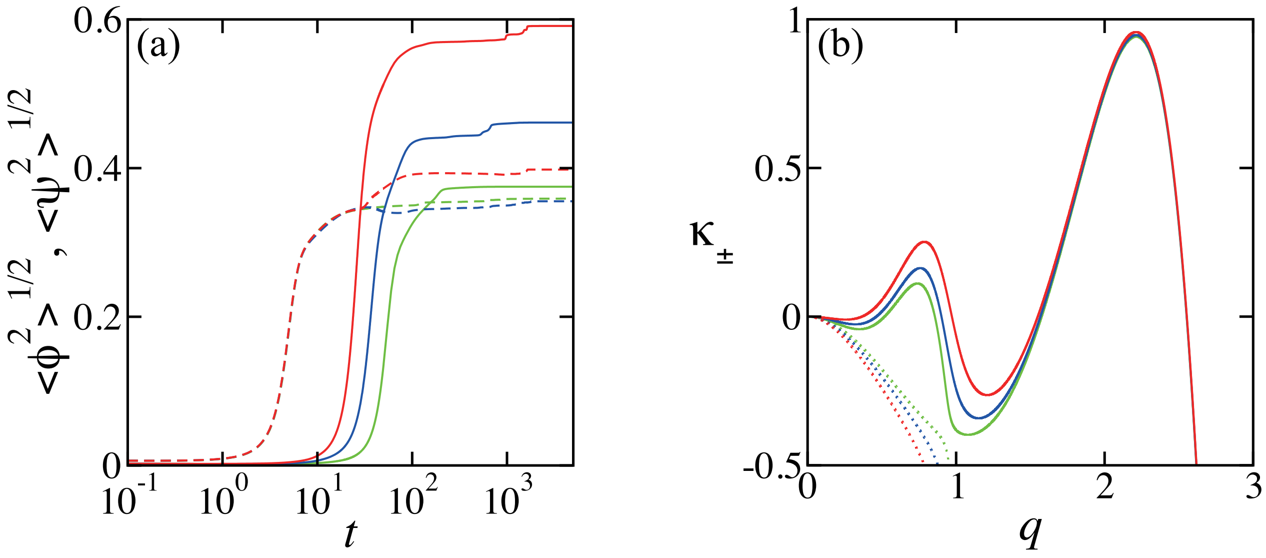

Figure 4.28: (a) Time evolution of the modulation amplitudes in each monolayers, $\langle\phi^2\rangle^{1/2}$ (solid line) and $\langle\psi^2\rangle^{1/2}$ (broken line) for $\Lambda = 0.1$ (green), $\Lambda = 0.3$ (blue), $\Lambda = 0.5$ (red). Other parameters are $\tau_\phi = \tau_\psi = 0.8, \phi_0 = \psi_0 = 0, B = A = 1, D = 0.0123, C = 0.1111$ $(q^*_\psi/q^*_\phi = 3)$. (b) Growth exponents of the concentration. κ_+ and κ_- are drawn with solid and dotted lines respectively. For the derivation see Appendix C.

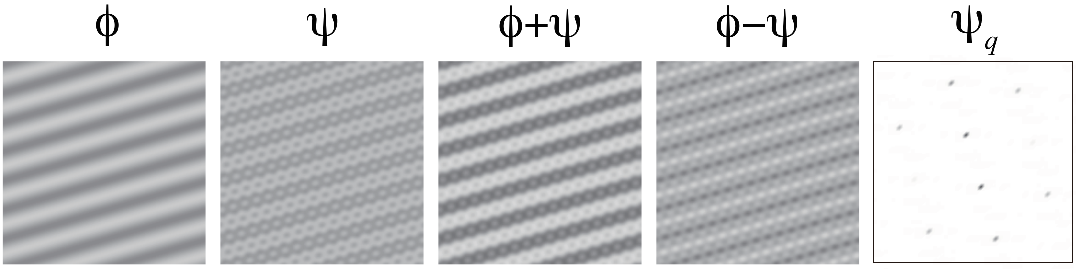

Figure 4.29: Patterns of coupled bilayers of with different temperatures and characteristic wavenumbers. ($\phi_0 = \psi_0 = 0, \tau_\phi = 0.8, \tau_\psi = 0.9, \Lambda = 0.3$). The patterns of ϕ, ψ, $\phi + \psi$, $\phi - \psi$ and ψ_q obtained after long time simulation ($t = 5000$) are presented. The parameters chosen here are $B = A = 1, D = 0.0123, C = 0.1111$ ($q^*_\psi / q^*_\phi = 3$).

Chapter 5

Discussions

5.1 Emergence of the characteristic length scale

We shall call the structure of the bilayers as “2D micelles” because finite sized structures emerge for binary lipid mixtures. Notice that the term “2D micelles” was introduced to explain the submicron sized domain formations in Langmuir monolayers, similar to the aggregates in the 3D surfactant solutions [55]. It should be pointed out that the structure of the 2D micelles is different from that presented here, since their formulation is based on the thermodynamics of aggregates of solute molecules in 2D. In our approach, the mechanism for the finite sized domain formation originates from the coupling between the chain orientational field and the composition field in a monolayer. Hence the characteristic size of the domains is different. Yamamoto *et.al.* considered the phase behavior of the membranes consisting of saturated lipid, hybrid lipid and cholesterol (SHC membrane) [31]. They showed that the line tension between domains becomes negative at temperatures close to the critical point. This effect is more enhanced for higher cholesterol concentration although the presence of cholesterol is implicitly taken into account by the effective membrane pressure.

When the two chains of the hybrid lipid are different and the saturated tail has a similar chain packing property with that of the saturated lipid, we can expect that the orientational coupling effect is large. In addition, when the saturated lipids are asymmetric in terms of the chain length, the degree of the orientational effects can be altered. We believe that the 2D micelles emerge when both the immiscibility and the orientational effect of these lipids are strong. The situation can be realized when one of the saturated chains of the saturated lipid is long (ordered), while the length of the other saturated chain in the saturated lipid is short. In short, whether 2D micelles are observed or not is dependent on the choice of the lipids used for the investigation.

A self consistent mean-field theoretical model was proposed to study domain formations in membranes containing saturated lipid, hybrid lipid, and cholesterol [56]. Phase separated patterns are calculated by taking into account the chain order and orientations in the membranes. The feasibility of the orientational effect discussed here can be verified with their model.

It is important to detect the existence of the orientational coupling effect experimentally. By labeling only one of the chains with deuterium and with the use of NMR spectroscopy, one can detect averaged orientation of the lipid. By comparing the degree of the orientation in the membranes between the homogeneous state and the phase separated state, one can check the existence of the orientational field.

It is suggested that the 2D micelles can be observed in the two-phase region with a large amount of cholesterol. The domain size could be smaller than the resolution of the fluorescent microscope. In order to detect the domains of submicron size, small angle neutron scattering (SANS) and neutron spin echo (NSE) experiments are suitable for studying the structure and dynamics of the lipid membrane systems.

Although we presented a phenomenological free energy of the lipid monolayers, it is possible to obtain this free energy from a microscopic lattice model. For example, we can regard the monolayer as a coupled spin system; Ising model and XY model. The latter model describes the Kosterlitz-Thouless transition in which the binding and the unbinding of pairs of vortices of the vector field is related to the superfluidity or superconductivity. It may be possible to obtain the Ginzburg-Landau free energy functional from the Hamiltonian within the mean field approximations.

5.2 Concentration fluctuations of 2D micelles

According to the experimental study of the single lipid molecule observation in biomembranes using STED, the lipid molecules repeatedly assemble and disassemble [11]. When the temperature is below the transition temperature, phase separated domains appear from the homogeneous state and coarsen irreversibly towards the macroscopically phase separated state. Once the equilibrium state is reached, the structure of the domains does not change. This picture contradicts with the dynamical assembly of lipid molecule shown by the experiments.

Our "2D micelles" model with concentration fluctuations can be one of the possibilities to explain the finite sized domain formation in biological membranes. Our model describes dynamical assembly and disassembly of lipid molecules. The structure and the lifetime of lipid domains can be determined by the physical chemistry properties of the lipid molecules. For critical fluctuations in binary mixtures, the correlation length being a function of the temperature gives the only length scale. For 2D micelles above the transition temperature, there is a characteristic length for the modulation of the concentration fluctuation (see Eq. (3.25)) in addition to the correlation length. These typical length scales depend on the properties of the hybrid lipid, e.g., the chemical structure of the lipid, the position of the double bond in the unsaturated tail or the asymmetry of the chain lengths (through the parameters such as σ, a, K_1, g). We note that the main transition temperature of the unsaturated lecithins having one saturated tail and one unsaturated tail is strongly dependent on the position of the double bond in the acyl chain [57]. The decay time of concentration fluctuations at a particular length scale also depends on the properties of the hybrid lipid. It should be mentioned that the critical point is also dependent on the parameters such as A and B. The 2D micelles model uniquely describes the size and the lifetime of the finite sized domain in terms of the physical chemistry properties of the lipid molecules.

It is worthwhile to imagine that the cells are utilizing the nature of the 2D micelles which control the size and lifetime of fluctuations in the bilayers by synthesizing and transporting the particular hybrid lipids. In addition, if such lipids were transported to every organ in the cell, the properties of the raft domains in these membranes can be synchronized in time. In other words, the coupling of the 2D micelles in the membranes and the lipid transports can be the language of the intracellular recognition in cells. Such a scenario might be important for various bio-functions acting harmonically in the cell.

We can also regard our model as "coupled 2D microemulsions" when the monolayers are composed of saturated lipid, hybrid lipid, unsaturated lipid (both tails have a double bond). For 3D microemulsions, we need a surface active agent which locates at the interface of immiscible components. In monolayers, the line active molecules play the same role as the surface active molecule. Recently, it is reported that a molecule consisting of a hydrocarbon block and a fluorocarbon block acts as a linactant in 2D mixed Langmuir monolayers composed of pentadecanoic acid and perfluoroundecanoic acid [58]. The molecule locates at the domain boundary reducing the line tension. As a result, bubble like domains of submicron size were observed. This result implies that the amphiphilic nature also exists in 2D monolayer systems.

The characteristic wavelength of modulation is dependent on the coefficients A, B, C, D. Using the analogy with 3D microemulsions, these quantities are related to the concentration of the hybrid lipid. According to the lattice model of 3D microemulsions, the structure factor such as Eq. (3.22) was analytically obtained by Gompper and Schick [47]. As a different approach for 3D microemulsions, a variational method based on the bending elasticity of membranes composed of surfactant molecules was reported before [59].

Within this approach the same functional form of the structure factor was obtained, while the prefactors are related to the bending rigidity and the concentration of the amphiphilic molecule.

Brewster *et al.* considered four component systems composed of saturated lipid, hybrid lipid, unsaturated lipid and cholesterol [29]. They investigated the decrease of the line tension due to the presence of the hybrid lipid. For four component systems, however, the hybrid lipids are localized at the interface only when the saturated and the unsaturated lipids are strongly segregated in the low temperature because of the entropic reason.

The dynamics of 3D microemulsions are investigated based on Ginzburg-Landau theory for both concentrations and velocity field [60]. The coupling effects between the bulk (water, oil) and the surfactant film were considered [61]. In the latter study, double exponential decay of the concentration fluctuations is predicted because of the coupling between the concentration and velocity field. The relaxation of the membranes fluctuation in 3D microemulsions or sponge phase in surfactant solutions is predicted to be a stretched exponential of $\exp[-(\Gamma t)^{\beta}]$ with the exponent of $\beta = 2/3$ [62], while the experimental value is obtained for the sponge phase [63]. It is interesting to consider whether the stretched exponential decay can be obtained from the fluctuation of the domain boundary within 2D plane of lipid membranes.

The non-equilibrium lipid transport between the cell interior and the membrane may also influence the domain formation. Such an effect was taken into account in the kinetic aggregation model of the lipid clusters [64], or in the phase separation of binary lipid mixtures [65, 66]. These models explain the existence of the finite sized domains which do not coarsen in time. Recently a general model which takes into account the lipid transport, interface pinning by proteins, and critical fluctuations has been proposed [67]. The authors suggested some criteria to elucidate the domain formation mechanism by comparing the spatial and time correlations of the domains between the theory and experimental results.

5.3 Coupling of different modulations

We showed that the large coupling parameter results in the lower transition temperature. This is because the coupling effectively decreases the free energy through the term $-\Lambda\phi\psi$. Similar results are obtained in the study of bilayers using Monte Carlo simulation [68]. If we rewrite the coupling term as $\Lambda(\phi - \psi)^2$, the terms $\Lambda\phi^2$ and $\Lambda\psi^2$ compensate the energy decrease due to the $-2\Lambda\phi\psi$ term. In this case, the transition temperature is not altered.

When the bilayers have different characteristic length scales, another interesting fact is that the temperature in the monolayer with a larger characteristic length dominates the transition temperature of the coupled bilayer. Because biomembranes typically have asymmetric compositions, such an effect may be important.

In order to have asymmetric bilayers with different characteristic wavenumbers, the lipid species in each monolayer should be different. Otherwise the gradient terms would be the same between the upper and the lower monolayers in Eq. 2.18. We note that the characteristic wavenumber is given by $q^* = \sqrt{a(1 - a\sigma/g^2)/2K_1}$ (see Eq. (2.16)). Hence if K_1 and g are different between the two monolayers, the two different characteristic wavenumbers emerge.

We also point out that there are some similarities between the coupled modulated structures and the problem of atoms adsorbed on a periodic solid substrate. The latter problem has been extensively studied within the Frenkel-Kontorova (FK) model which provides a simple description of the commensurate-incommensurate transition [69]. Our model and the FK model are analogous in the sense that there are two natural length scales whose ratio changes as a function of the model parameters. In the FK model, however, these length scales are quenched, whereas in our result they are annealed. Modulated structure discussed in this thesis is only weakly segregated since the temperature is close to the critical point. The frustration generated by the coupling is compensated by the coexistence of two different characteristic wavenumbers in one of the monolayers. When the contribution of the modulation is smaller than that of the phase separation, the natural length scales may be disturbed by the coupling and the commensurate-incommensurate transition can be observed. Then we can anticipate the existence of the transition in the strong segregation regime.

5.4 Non-equilibrium nature of asymmetrical bilayers

Biomembranes of living cells are known to have asymmetric compositions between two monolayers. In the case of flat model membranes, a compositionally asymmetric bilayers will eventually become a symmetric one after a long time. This is because the asymmetric membranes are not in equilibrium. In order to reduce the free energy, flipping of the lipids takes place in bilayers although such process is not allowed in our model, i.e., the lipid composition is conserved in each monolayer. The energy barrier for flipping from one monolayer to the other is relatively high because the hydrophilic part of the lipid should contact with the hydrophobic chains during the flipping process. Since the flipping rate is low, the metastable asymmetric states persist for a long time. Some years ago, the dynamics of lipid exchange in a single component vesicle is performed using time resolved small angle neutron scattering [70]. The half-life of the lipid composition due to flip-flop motion was estimated to be several hours at physiological temperatures. In the case of living cells, the asymmetry in the lipid composition is maintained by the enzymes called "flippase" which actively transport the lipids [71]. More importantly, the compositional asymmetry between the two leaflets is closely related to the biological functions. For instance, the breakdown of the compositional asymmetry has to do with the programed death (apoptosis) of the cell [72]. Hence it is important to consider the effects of asymmetry on the properties of lipid domains.

Chapter 6

Conclusion

In this thesis, we proposed a model for lipid bilayers, and discussed the mechanism of the finite-sized domain formation together with the effects of coupling of the two monolayers.

A lipid monolayer consisting of saturated lipid, hybrid lipid and cholesterol was considered. We proposed a phenomenological Ginzburg-Landau model in which the coupling of the lipid composition and chain orientational vector field is considered.

This coupling arises from the liquid crystalline nature of the hybrid lipid which adjusts its orientational order in the tails to reduce the line tension. As a result, finite-sized domains can be formed. The minimization of the free energy with respect to the vector field yields an effective free energy which is analogous to that of 3D microemulsions (above the transition temperature) and modulated structures (below the transition temperature). Then we considered the model for lipid bilayers comprised of two modulated monolayers which are coupled via interleaflet interactions. The structure and the dynamics of the coupled modulated bilayer are investigated theoretically.

We first studied concentration fluctuations in bilayers occurring above the transition temperature. We have calculated the static structure factors, and obtained the bilayer phase diagrams close to the critical temperature. The coupling effect expands the regions of the ordered phase and the structured-disorder phase. In both monolayers, fluctuations are induced due to the coupling, and the spectrum of the induced fluctuations is determined by the cross correlation of the structure factor. When the two monolayers having different preferred wavenumbers are coupled, the peak height at smaller wavenumber becomes larger, whereas that at a larger wavenumber remains the same. Similarly, the temperature in the monolayer with a smaller wavenumber dominates the behavior of the critical temperature of the bilayer. We studied the dynamics of concentration fluctuations by using the coupled TDGL equations, and calculated the intermediate structure factors of the bilayer. In general, concentration fluctuations exhibit a double-exponential decay. Due to the coupling, the time for the cross over of the two concentration fluctuations appears when the characteristic length scale of each monolayer is different.

Then we discussed the phase separation of the coupled modulated bilayers. We constructed various phase diagrams of the bilayer when the two monolayers have the same wavenumber of the modulations. The phase behavior of the bilayers is described by the combinations of the stripe and the hexagonal morphologies. Due to the coupling effect, one of the monolayers induces micro-phase separation in the other monolayer. As the coupling strength increases, the asymmetric phases tend to disappear. By performing numerical simulations, we obtained various phase separated patterns when the two monolayers have different modulations. The obtained patterns are approximately classified into “independent”, ‘intermediate” and “coincident” cases. The degree of the overlap between the two monolayers is characterized by the quantity Δ as defined in Eq. (4.38). We showed that the initial growth rates of the most unstable mode are essentially identical to the decay rates of the concentration fluctuations.

Although the signal transduction on membranes are important for various biological functions, its dynamical properties such as the characteristic time scale are still under investigation. Even the relations between biological functions and protein structures have been investigated extensively, it is still difficult to observe the dynamical communication processes between proteins. Since our theory explains the size and the dynamics of lipid domains, it could be a scaffold for understanding the functional processes in membranes. We hope that this work has made a useful contribution to this direction of the research.

Appendix A

Here we consider the other possibility of the coupling terms between the monolayers. The free energy including the higher order coupling and non-local coupling terms is

$$\begin{aligned} F_{\mathrm{b}}[\phi,\psi] = \int \mathrm{d}\mathbf{r} \Big[& 2B(\nabla^2\phi)^2 - 2A(\nabla\phi)^2 + \frac{\tau_\phi}{2}\phi^2 + \frac{1}{4}\phi^4 - \mu_\phi\phi \\ & + 2D(\nabla^2\psi)^2 - 2C(\nabla\psi)^2 + \frac{\tau_\psi}{2}\psi^2 + \frac{1}{4}\psi^4 - \mu_\psi\psi - \Lambda\phi\psi \\ & - \nu\phi^2\psi^2 - \upsilon(\phi\psi^3 + \phi^3\psi) \\ & - \zeta(\nabla\phi)(\nabla\psi) - \epsilon(\nabla^2\phi)(\nabla^2\psi) - \eta((\nabla^2\phi)\psi + \phi(\nabla^2\psi)) \Big]. \end{aligned} \tag{6.1}$$

Where Λ, ν, υ are the local and ζ, ϵ, η are the nonlocal coupling coefficients. If we write the order parameters ϕ and ψ as $\phi = \phi_0 + \delta\phi$, $\psi = \psi_0 + \delta\psi$, and $\delta\phi(\mathbf{q}) = \int \mathrm{d}\mathbf{r}\,\delta\phi(\mathbf{r}\,)\exp(-i\mathbf{q}\cdot\mathbf{r}\,)$, $\delta\psi(\mathbf{q}) = \int \mathrm{d}\mathbf{r}\,\delta\psi(\mathbf{r}\,)\exp(-i\mathbf{q}\cdot\mathbf{r}\,)$. The free energy in Fourier space is written as

$$\begin{aligned} F_{\mathrm{b}}[\phi,\psi] = \int \mathrm{d}\mathbf{q} \Bigg[& \left(2Bq^4 - 2Aq^2 + \frac{\tau'_\phi}{2}\right)\delta\phi(\mathbf{q})\delta\phi(-\mathbf{q}) \\ & + \left(2Dq^4 - 2Cq^2 + \frac{\tau'_\psi}{2}\right)\delta\psi(\mathbf{q})\delta\psi(-\mathbf{q}) \\ & - \left(\Lambda_l + \zeta q^2 + \epsilon q^4 - 2\eta q^2\right)\delta\phi(\mathbf{q})\delta\psi(-\mathbf{q}) \Bigg], \end{aligned} \tag{6.2}$$

Where

$$\tau'_\phi = \tau_\phi + 3\phi_0^2/2 - 3\upsilon\phi_0\psi_0 - \nu\psi_0^2, \tag{6.3}$$

$$\tau'_\psi = \tau_\psi + 3\psi_0^2/2 - 3\upsilon\phi_0\psi_0 - \nu\phi_0^2, \tag{6.4}$$

$$\Lambda_l = \Lambda + 3\upsilon(\phi_0^2 + \psi_0^2) + 2\nu\phi_0\psi_0. \tag{6.5}$$

By defining

$$\Gamma'_\phi(q) = 2Bq^4 - 2Aq^2 + \tau'_\phi/2, \tag{6.6}$$

$$\Gamma'_\psi(q) = 2Dq^4 - 2Cq^2 + \tau'_\psi/2, \tag{6.7}$$

$$\Lambda' = \Lambda_l + \zeta q^2 + \epsilon q^4 - 2\eta q^2, \tag{6.8}$$

and repeating the same procedure to obtain the structure factors, we obtain the static structure factors as

$$S_{\phi\phi}(\mathbf{q}) = \frac{2\Gamma'_\psi(q)}{4\Gamma'_\phi(q)\Gamma'_\psi(q) - \Lambda'^2}, \tag{6.9}$$

$$S_{\psi\psi}(\mathbf{q}) = \frac{2\Gamma'_\phi(q)}{4\Gamma'_\phi(q)\Gamma'_\psi(q) - \Lambda'^2}, \tag{6.10}$$

$$S_{\phi\psi}(\mathbf{q}) = \frac{\Lambda}{4\Gamma'_\phi(q)\Gamma'_\psi(q) - \Lambda'^2}. \tag{6.11}$$

Notice that these equations can be obtained by changing $\Gamma_\phi \rightarrow \Gamma'_\phi$, $\Gamma_\psi \rightarrow \Gamma'_\psi$ and $\Lambda \rightarrow \Lambda'$ in Eqs. (3.14), (3.15), (3.16).

Similarly, by defining

$$\omega'^2_\phi = 4L^2_\phi q^4[\Gamma'_\phi(q)]^2 + L_\phi L_\psi q^4 \Lambda'^2, \tag{6.12}$$

$$\omega'^2_\psi = 4L^2_\psi q^4[\Gamma'_\psi(q)]^2 + L_\phi L_\psi q^4 \Lambda'^2, \tag{6.13}$$

$$\omega'_{\phi\psi} = 2q^2[L_\phi \Gamma'_\phi(q) + L_\psi \Gamma'_\psi(q)], \tag{6.14}$$

we can obtain intermediate structure factors by exchanging $\omega_\phi \rightarrow \omega'_\phi$, $\omega_\psi \rightarrow \omega'_\psi$ and $\omega_{\phi\psi} \rightarrow \omega'_{\phi\psi}$ in Eqs. (3.51), (3.52), (3.53) and (3.62).

Appendix B

We show the derivation of the real space correlation function of a 2D monolayer. The scattering functions of the monolayer is given as

$$S(q) = \frac{1}{4Bq^4 - 4Aq^2 + \tilde{\tau}_\phi}. \tag{B.15}$$

The real space correlation function in the monolayer is given by the inverse Fourier transform of the above scattering function in 2D.

$$\begin{aligned} G_\phi(r) &= \frac{1}{(2\pi)^2} \int \mathrm{d}\mathbf{r}\, S(q) \exp(i\mathbf{q}\cdot\mathbf{r}) \\ &= \frac{1}{(2\pi)^2} \frac{1}{B} \int_0^\infty \mathrm{d}q\, qS(q) \int_0^{2\pi} \mathrm{d}\theta\, \exp(iqr\cos\theta) \\ &= \frac{1}{4\pi B} \int_0^\infty \mathrm{d}q\, \frac{qJ_0(qr)}{q^4 - (A/B)q^2 + \tilde{\tau}_\phi/4B} \\ &= \frac{1}{4\pi B} I. \end{aligned} \tag{B.16}$$

Here θ and r are the angle and the distance in the polar coordinate, $J_n(qr)$ is the spherical Bessel function of the first kind. Using the relation $J_0(qr) = (H_0^{(1)}(qr) + H_0^{(2)}(qr))/2$, where $H_0^{(1)}(qr)$ and $H_0^{(2)}(qr)$ are the Hankel functions of the first and second kind, we can write $I = (I_1 + I_2)/2$ where

$$\begin{aligned} I_1 &= \int_0^\infty \mathrm{d}q\, \frac{qH_0^{(1)}(qr)}{q^4 - (A/B)q^2 + \tilde{\tau}_\phi/4B}, \\ I_2 &= \int_0^\infty \mathrm{d}q\, \frac{qH_0^{(2)}(qr)}{q^4 - (A/B)q^2 + \tilde{\tau}_\phi/4B}. \end{aligned} \tag{B.17}$$

Now we consider the integral in the complex plane by replacing q with the complex variable $z = x + iy$

$$I_i = \int_0^\infty \mathrm{d}z\, \frac{zH_0^{(i)}(zr)}{z^4 - (A/B)z^2 + \tilde{\tau}_\phi/4B}. \tag{B.18}$$

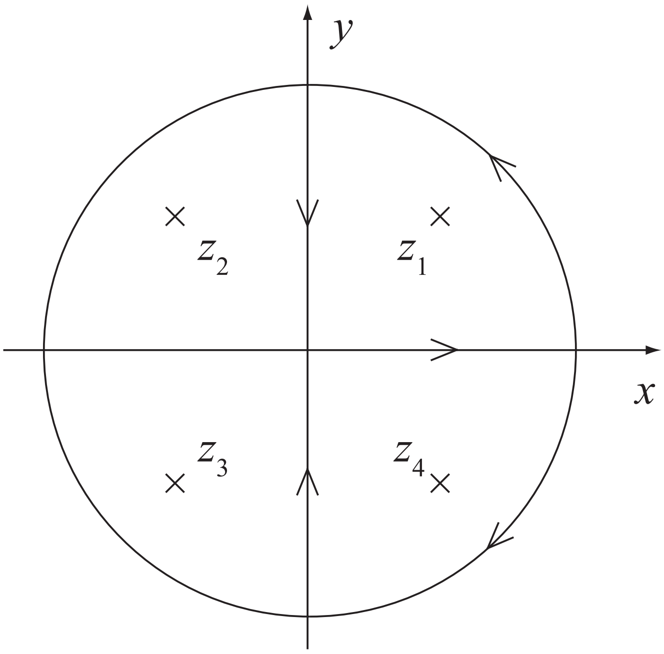

Figure B.1: Complex plane with 4 poles of Eq. (B.19) and the paths of the integrals.

The integrand has poles at

$$\begin{aligned} z_1 &= \frac{(\tilde{\tau}_\phi/B)^{1/4}}{2}\left(\sqrt{1-\gamma_\phi}+i\sqrt{1+\gamma_\phi}\right), \\ z_2 &= \frac{(\tilde{\tau}_\phi/B)^{1/4}}{2}\left(-\sqrt{1-\gamma_\phi}+i\sqrt{1+\gamma_\phi}\right), \\ z_3 &= \frac{(\tilde{\tau}_\phi/B)^{1/4}}{2}\left(-\sqrt{1-\gamma_\phi}-i\sqrt{1+\gamma_\phi}\right), \\ z_4 &= \frac{(\tilde{\tau}_\phi/B)^{1/4}}{2}\left(\sqrt{1-\gamma_\phi}-i\sqrt{1+\gamma_\phi}\right). \end{aligned} \tag{B.19}$$

These poles are located in quadrants 1,2,3 and 4 off the x-axis. For the integral I_1, we integrate along the contour of the quarter-circle of infinite radius in the first quadrant in anti-clock wise direction. Using Cauchy's integral theorem, we obtain

$$\int_0^\infty \mathrm{d}x\,\frac{xH_0^{(1)}(xr)}{x^4-(A/B)x^2+\tilde{\tau}_\phi/4B}+\int_\infty^0 \mathrm{d}y\,\frac{iyH_0^{(1)}(iyr)}{y^4+(A/B)y^2+\tilde{\tau}_\phi/4B}=2\pi i\,\mathrm{res}(z=z_1), \tag{B.20}$$

where the residue is given by

$$\mathrm{res}(z=z_1)=\frac{H_0^{(1)}(z_1 r)}{2i\sqrt{\tilde{\tau}_\phi/B}\sqrt{1-\gamma_\phi^2}}. \tag{B.21}$$

For the integral I_2, we set the contour of the quarter-circle of infinite radius in the 4th quadrant in clock wise direction. Then

$$\int_0^\infty \mathrm{d}x\, \frac{xH_0^{(2)}(xr)}{x^4 - (A/B)x^2 + \tilde{\tau}_\phi/4B} + \int_{-\infty}^0 \mathrm{d}y\, \frac{iyH_0^{(2)}(iyr)}{y^4 + (A/B)y^2 + \tilde{\tau}_\phi/4B} = -2\pi i \,\mathrm{res}(z = z_4), \tag{B.22}$$

where the residue is given by

$$\mathrm{res}(z = z_4) = -\frac{H_0^{(2)}\left(z_4 r\right)}{2i\sqrt{\tilde{\tau}_\phi/B}\sqrt{1-\gamma_\phi^2}}. \tag{B.23}$$

Combining Eqs. (B.20) and (B.22), and with the use of $H_0^{(1)}(-z) = -H_0^{(2)}(z)$, we obtain

$$\begin{aligned} I =& \frac{\pi}{2\sqrt{\tilde{\tau}_\phi/B}\sqrt{1-\gamma_\phi^2}}\left[H_0^{(1)}\left(\left(\frac{\tilde{\tau}_\phi}{B}\right)^{1/4}\frac{\sqrt{1-\gamma_\phi}+i\sqrt{1+\gamma_\phi}}{2}r\right)\right.\\ &\left. + H_0^{(2)}\left(\left(\frac{\tilde{\tau}_\phi}{B}\right)^{1/4}\frac{\sqrt{1-\gamma_\phi}-i\sqrt{1+\gamma_\phi}}{2}r\right)\right]. \end{aligned} \tag{B.24}$$

By defining

$$\frac{\lambda_\phi}{2\pi} = \left(\frac{B}{\tilde{\tau}_\phi}\right)^{1/4}\frac{2}{\sqrt{1-\gamma_\phi}}, \tag{B.25}$$

$$\xi_\phi = \left(\frac{B}{\tilde{\tau}_\phi}\right)^{1/4}\frac{2}{\sqrt{1+\gamma_\phi}}, \tag{B.26}$$

we finally obtain

$$\begin{aligned} G_\phi(r) &= \frac{\xi_\phi\lambda_\phi}{64\pi B}\left[H_0^{(1)}\left(\frac{2\pi r}{\lambda_\phi}+i\frac{r}{\xi_\phi}\right) + H_0^{(2)}\left(\frac{2\pi r}{\lambda_\phi}-i\frac{r}{\xi_\phi}\right)\right] \\ &= \frac{\xi_\phi\lambda_\phi}{64\pi B}\left[H_0^{(1)}\left(\frac{2\pi r}{\lambda_\phi}+i\frac{r}{\xi_\phi}\right) + \overline{H_0^{(1)}\left(\frac{2\pi r}{\lambda_\phi}+i\frac{r}{\xi_\phi}\right)}\right] \\ &= \frac{\xi_\phi\lambda_\phi}{32\pi B}\mathrm{Re}\left[H_0^{(1)}\left(\frac{2\pi r}{\lambda_\phi}+i\frac{r}{\xi_\phi}\right)\right]. \end{aligned} \tag{B.27}$$

In the above, the overline represents the complex conjugate. We have also used the relation $H_0^{(2)}(\overline{z}) = \overline{H_0^{(1)}(z)}$.

Appendix C

We consider the phase separation dynamics in the early stage by linear stability analysis. We assume that ϕ and ψ are small, and neglect the higher order term of ϕ and ψ, the time evolution equations for the order parameters in Fourier space is obtained from Eq. (4.36, 4.37)

$$\begin{aligned}\frac{\partial\phi(\mathbf{q},t)}{\partial t} &= -2q^2L_\phi\Gamma_\phi\phi(\mathbf{q},t)+\Lambda\psi(\mathbf{q},t),\\ \frac{\partial\psi(\mathbf{q},t)}{\partial t} &= -2q^2L_\psi\Gamma_\psi\psi(\mathbf{q},t)+\Lambda\phi(\mathbf{q},t).\end{aligned} \tag{C.28}$$

Here we can rewrite these equations as

$$\begin{pmatrix}\partial\phi(\mathbf{q},t)/\partial t\\ \partial\psi(\mathbf{q},t)/\partial t\end{pmatrix}=\begin{pmatrix}-2q^2L\Gamma_\phi & L\Lambda q^2\\ L\Lambda q^2 & -2q^2L\Gamma_\psi\end{pmatrix}\begin{pmatrix}\phi(\mathbf{q},t)\\ \psi(\mathbf{q},t)\end{pmatrix}. \tag{C.29}$$

By diagonalizing the matrix, the solution is written as $\mathbf{x}=c_+\exp[\kappa_+t]\mathbf{v}_++c_-\exp[\kappa_-t]\mathbf{v}_-$, where $\mathbf{x}=(\phi(\mathbf{q},t),\psi(\mathbf{q},t))$, $c_\pm$ are coefficients, $\mathbf{v}_\pm$ are the eigen vectors and the eigenvalues, and $\kappa_\pm$ are expressed as

$$\kappa_\pm=Lq^2\left[-(\Gamma_\phi+\Gamma_\psi)\pm\sqrt{(\Gamma_\phi-\Gamma_\psi)^2+\Lambda^2}\right]. \tag{C.30}$$

Appendix D

For obtaining the phase diagram, the energy of SS, SH, HS, HH, HH* and QQ phases are calculated, via programs str-str.f, str-hex.f, hex-str.f, hex-hex.f, hex-hex-phase.f and squ.squ.f respectively. It should be noted that distributions of amplitudes of the modulation is also calculated via these programs. By comparing the lowest energy phase by the program min-energy3.f, we get the phase diagram.

```
      program str-str.f
      implicit none
c     written on 2008/11/06

      double precision fl,fh,fdis
      double precision ta1,ta2,g1,g2,PH,PS,mh,ms,la
      double precision tau1,tau2,gn1,gn2,phi,psi,lam
      double precision ampl,mhh,fmin,mps1,mps2,inmps,inmph,mps,mph
      integer i,ii,iii


      fl(ta1,ta2,g1,g2,PH,PS,mh,ms,la)
     &=ta1/2.0*(PH**(2.0))+g1/4.0*(PH**(4.0))
     &           +(ta1-1.0+3.0*g1*(PH**(2.0)))*(mh**(2.0))
     &           +3.0/2.0*g1*(mh**(4.0))
     &+ta2/2.0*(PS**(2.0))+g2/4.0*(PS**(4.0))
     &           +(ta2-1.0+3.0*g2*(PS**(2.0)))*(ms**(2.0))
     &           +3.0/2.0*g2*(ms**(4.0))
     &           -la*(PH*PS+2.0*mh*ms)

      ampl(ta1,ta2,g1,g2,PH,PS,ms,la)
     &=(ta1-1.0+3.0*g1*(PH**(2.0)))
     &*((ta2-1.0+3.0*g2*(PS**(2.0)))*ms+3.0*g2*(ms**(3.0)))/la
     &+3.0*g1*((
     &((ta2-1.0+3.0*g2*(PS**(2.0)))*ms+3.0*g2*(ms**(3.0)))/la)**(3.0))
     &-la*ms

      mhh(ta2,g2,PS,ms,la)
     &=((ta2-1.0+3.0*g2*(PS**(2.0)))*ms+3.0*g2*(ms**(3.0)))/la

      open(1,file='str_str_min_energy_tau08_g1_la02.dat')
      open(5,file='str_str_mh_tau08_g1_la02.dat')
      open(6,file='str_str_ms_tau08_g1_la02.dat')

      tau1=0.8
      tau2=0.8
      gn1=1.0
      gn2=1.0
      lam=0.2

      do i=1,2000
         phi=-1.0+i/1000.0
         do ii=1,2000
            psi=-1.0+ii/1000.0
            fmin=100001.0
            do iii=1,1000000
               mps1=-1.0+iii/500000.0
               mps2=-1.0+(iii+1.0)/500000.0
               if ((((ampl(tau1,tau2,gn1,gn2,phi,psi,mps1,lam).lt.0.0)
     &          .and.(ampl(tau1,tau2,gn1,gn2,phi,psi,mps2,lam).gt.0.0))
     &          .or.((ampl(tau1,tau2,gn1,gn2,phi,psi,mps1,lam).gt.0.0)
     &          .and.(ampl(tau1,tau2,gn1,gn2,phi,psi,mps2,lam).lt.0.0)))
     &           .or.(ampl(tau1,tau2,gn1,gn2,phi,psi,mps1,lam).eq.0.0))
     &    then
```

```
                inmps=mps1
                inmph=mhh(tau2,gn2,psi,inmps,lam)
                if (inmps.eq.0.0) then
                   goto 100
                end if
          if (fl(tau1,tau2,gn1,gn2,phi,psi,inmph,inmps,lam).lt.fmin) then
                fmin=fl(tau1,tau2,gn1,gn2,phi,psi,inmph,inmps,lam)
                mps=inmps
                mph=inmph
             end if
          end if
100     end do
          write(1,930) fmin
          write(5,900) phi,psi,mph
          write(6,900) phi,psi,mps
        end do
        end do

        close(1)

900     format(f14.7,' ',f14.7,' ',f14.7)
910     format(f14.7,' ',f14.7,' ',f14.7,' ',f14.7,' ',f14.7)
920     format(f14.7,' ',f14.7)
930     format(f14.7)
        stop
        end
```

```
      program str-hex.f
      implicit none
c     revised 2010/11/11

      double precision fl,fh,fdis
      double precision ta1,ta2,g1,g2,PH,PS,mh,ms,la
      double precision tau1,tau2,gn1,gn2,phi,psi,lam
      double precision ampl,mhh,fmin,mps1,mps2,inmps,inmph,mps,mph
      integer i,ii,iii


      fl(ta1,ta2,g1,g2,PH,PS,mh,ms,la)
     &=ta1/2.0*(PH**(2.0))+g1/4.0*(PH**(4.0))
     &           +(ta1-1.0+3.0*g1*(PH**(2.0)))*(mh**(2.0))
     &           +3.0/2.0*g1*(mh**(4.0))
     &+ta2/2.0*(PS**(2.0))+g2/4.0*(PS**(4.0))
     &           +(ta2-1.0+3.0*g2*(PS**(2.0)))*(ms**(2.0))
     &           +5.0/2.0*g2*(ms**(4.0))
     &           +4.0/(3.0**(1.0/2.0))*g2*PS*(ms**(3.0))
     &           -la*(PH*PS+2.0/(3.0**(1.0/2.0))*mh*ms)

      ampl(ta1,ta2,g1,g2,PH,PS,ms,la)
     &=(ta1-1.0+3.0*g1*(PH**(2.0)))
     &*((ta2-1.0+3.0*g2*(PS**(2.0)))*ms+5.0*g2*(ms**(3.0))
     &+2.0*(3.0**(1.0/2.0))*g2*PS*(ms**2.0))*(3.0**(1.0/2.0))/la
     &+3.0*g1*((((ta2-1.0+3.0*g2*(PS**(2.0)))*ms+5.0*g2*(ms**(3.0))
     &+2.0*(3.0**(1.0/2.0))*g2*PS*(ms**2.0))*(3.0**(1.0/2.0))/la)**3.0)
     &-la*ms/(3.0**(1.0/2.0))

      mhh(ta2,g2,PS,ms,la)
     &=((ta2-1.0+3.0*g2*(PS**(2.0)))*ms+5.0*g2*(ms**(3.0))
     &+2.0*(3.0**(1.0/2.0))*g2*PS*(ms**2.0))*(3.0**(1.0/2.0))/la

      open(1,file='str_hex_min_energy_tau08_g1_la02.dat')
      open(6,file='str_hex_mh_tau08_g1_la02.dat')
      open(7,file='str_hex_ms_tau08_g1_la02.dat')

      tau1=0.8
      tau2=0.8
      gn1=1.0
      gn2=1.0
      lam=0.2

      do i=1,2000
         phi=-1.0+i/1000.0
         do ii=1,2000
            psi=-1.0+ii/1000.0
            fmin=100002.0
            do iii=1,1000000
               mps1=-1.0+iii/500000.0
               mps2=-1.0+(iii+1.0)/500000.0
               if ((((ampl(tau1,tau2,gn1,gn2,phi,psi,mps1,lam).lt.0.0)
     &          .and.(ampl(tau1,tau2,gn1,gn2,phi,psi,mps2,lam).gt.0.0))
     &          .or.((ampl(tau1,tau2,gn1,gn2,phi,psi,mps1,lam).gt.0.0)
```

```
    &          .and.(ampl(tau1,tau2,gn1,gn2,phi,psi,mps2,lam).lt.0.0)))
    &           .or.(ampl(tau1,tau2,gn1,gn2,phi,psi,mps1,lam).eq.0.0))
    &    then
             inmps=mps1
             inmph=mhh(tau2,gn2,psi,inmps,lam)
             if (inmps.eq.0.0) then
                goto 100
             end if
       if (fl(tau1,tau2,gn1,gn2,phi,psi,inmph,inmps,lam).lt.fmin) then
             fmin=fl(tau1,tau2,gn1,gn2,phi,psi,inmph,inmps,lam)
             mps=inmps
             mph=inmph
          end if
       end if
100  end do
       write(1,930) fmin
       write(6,900) phi,psi,mph
       write(7,900) phi,psi,mps
     end do
     end do

     close(1)

900  format(f14.7,' ',f14.7,' ',f14.7)
910  format(f14.7,' ',f14.7,' ',f14.7,' ',f14.7,' ',f14.7)
920  format(f14.7,' ',f14.7)
930  format(f14.7)
     stop
     end
```

```
      program hex-hex.f
      implicit none
c     written on 2008/11/06

      double precision fl,fh,fdis
      double precision ta1,ta2,g1,g2,PH,PS,mh,ms,la
      double precision tau1,tau2,gn1,gn2,phi,psi,lam,mss
      double precision ampl,fmin,mph1,mph2,inmps,inmph,mps,mph
      integer i,ii,iii


      fl(ta1,ta2,g1,g2,PH,PS,mh,ms,la)
     &=ta2/2.0*(PS**(2.0))+g2/4.0*(PS**(4.0))
     &           +(ta2-1.0+3.0*g2*(PS**(2.0)))*(ms**(2.0))
     &           +3.0/2.0*g2*(ms**(4.0))
     &+ta1/2.0*(PH**(2.0))+g1/4.0*(PH**(4.0))
     &           +(ta1-1.0+3.0*g1*(PH**(2.0)))*(mh**(2.0))
     &           +5.0/2.0*g1*(mh**(4.0))
     &           +4.0/(3.0**(1.0/2.0))*g1*PH*(mh**(3.0))
     &           -la*(PS*PH+2.0/(3.0**(1.0/2.0))*ms*mh)

      ampl(ta1,ta2,g1,g2,PH,PS,mh,la)
     &=(ta2-1.0+3.0*g2*(PS**(2.0)))
     &*((ta1-1.0+3.0*g1*(PH**(2.0)))*mh+5.0*g1*(mh**(3.0))
     &+2.0*(3.0**(1.0/2.0))*g1*PH*(mh**2.0))*(3.0**(1.0/2.0))/la
     &+3.0*g2*((((ta1-1.0+3.0*g1*(PH**(2.0)))*mh+5.0*g1*(mh**(3.0))
     &+2.0*(3.0**(1.0/2.0))*g1*PH*(mh**2.0))*(3.0**(1.0/2.0))/la)**3.0)
     &-la*mh/(3.0**(1.0/2.0))

      mss(ta1,g1,PH,mh,la)
     &=((ta1-1.0+3.0*g1*(PH**(2.0)))*mh+5.0*g1*(mh**(3.0))
     &+2.0*(3.0**(1.0/2.0))*g1*PH*(mh**2.0))*(3.0**(1.0/2.0))/la

      open(1,file='hex_str_min_energy_tau08_g1_la02.dat')
      open(6,file='hex_str_mh_tau08_g1_la02.dat')
      open(7,file='hex_str_ms_tau08_g1_la02.dat')

      tau1=0.8
      tau2=0.8
      gn1=1.0
      gn2=1.0
      lam=0.2

      do i=1,2000
         phi=-1.0+i/1000.0
         do ii=1,2000
            psi=-1.0+ii/1000.0
            fmin=100002.0
            do iii=1,1000000
               mph1=-1.0+iii/500000.0
               mph2=-1.0+(iii+1.0)/500000.0
               if ((((ampl(tau1,tau2,gn1,gn2,phi,psi,mph1,lam).lt.0.0)
     &          .and.(ampl(tau1,tau2,gn1,gn2,phi,psi,mph2,lam).gt.0.0))
     &          .or.((ampl(tau1,tau2,gn1,gn2,phi,psi,mph1,lam).gt.0.0)
```

```
    &          .and.(ampl(tau1,tau2,gn1,gn2,phi,psi,mph2,lam).lt.0.0)))
    &           .or.(ampl(tau1,tau2,gn1,gn2,phi,psi,mph1,lam).eq.0.0))
    &         then
                 inmph=mph1
                 inmps=mss(tau1,gn1,phi,inmph,lam)
             if (inmph.eq.0.0) then
                goto 100
             end if
       if (fl(tau1,tau2,gn1,gn2,phi,psi,inmph,inmps,lam).lt.fmin) then
             fmin=fl(tau1,tau2,gn1,gn2,phi,psi,inmph,inmps,lam)
             mps=inmps
             mph=inmph
          end if
       end if
100  end do
       write(1,930) fmin
       write(6,900) phi,psi,mph
       write(7,900) phi,psi,mps
     end do
     end do


     close(1)

900  format(f14.7,’ ’,f14.7,’ ’,f14.7)
910  format(f14.7,’ ’,f14.7,’ ’,f14.7,’ ’,f14.7,’ ’,f14.7)
920  format(f14.7,’ ’,f14.7)
930  format(f14.7)
     stop
     end
```

```
      program hex-hex.f
      implicit none
c     written on 2008/11/06
c     rivised on 2008/11/10
c     adding contour on 2008/11/12

      double precision fl,fh,fdis
      double precision ta1,ta2,g1,g2,PH,PS,mh,ms,la
      double precision tau1,tau2,gn1,gn2,phi,psi,lam
      double precision ampl,mhh,fmin,mps1,mps2,inmps,inmph,mps,mph
      integer i,ii,iii


      fl(ta1,ta2,g1,g2,PH,PS,mh,ms,la)
     &=ta1/2.0*(PH**(2.0))+g1/4.0*(PH**(4.0))
     &           +(ta1-1.0+3.0*g1*(PH**(2.0)))*(mh**(2.0))
     &           +5.0/2.0*g1*(mh**(4.0))
     &           +4.0/(3.0**(1.0/2.0))*g1*PH*(mh**(3.0))
     &+ta2/2.0*(PS**(2.0))+g2/4.0*(PS**(4.0))
     &           +(ta2-1.0+3.0*g2*(PS**(2.0)))*(ms**(2.0))
     &           +5.0/2.0*g2*(ms**(4.0))
     &           +4.0/(3.0**(1.0/2.0))*g2*PS*(ms**(3.0))
     &           -la*(PH*PS+2.0*mh*ms)

      ampl(ta1,ta2,g1,g2,PH,PS,ms,la)
     &=(ta1-1.0+3.0*g1*(PH**(2.0)))
     &*((ta2-1.0+3.0*g2*(PS**(2.0)))*ms+5.0*g2*(ms**(3.0))
     &+2.0*(3.0**(1.0/2.0))*g2*PS*(ms**2.0))/la
     &+5.0*g1*((((ta2-1.0+3.0*g2*(PS**(2.0)))*ms+5.0*g2*(ms**(3.0))
     &+2.0*(3.0**(1.0/2.0))*g2*PS*(ms**2.0))/la)**(3.0))
     &+2.0*(3.0**(1.0/2.0))*g1*PH
     &*((((ta2-1.0+3.0*g2*(PS**(2.0)))*ms+5.0*g2*(ms**(3.0))
     &+2.0*(3.0**(1.0/2.0))*g2*PS*(ms**2.0))/la)**(2.0))
     &-la*ms

      mhh(ta2,g2,PS,ms,la)
     &=((ta2-1.0+3.0*g2*(PS**(2.0)))*ms+5.0*g2*(ms**(3.0))
     &+2.0*(3.0**(1.0/2.0))*g2*PS*(ms**2.0))/la

      open(1,file='hex_hex_min_energy_tau08_g1_la02.dat')
      open(5,file='hex_hex_mh_tau08_g1_la02.dat')
      open(6,file='hex_hex_ms_tau08_g1_la02.dat')

      tau1=0.8
      tau2=0.8
      gn1=1.0
      gn2=1.0
      lam=0.2

      do i=1,2000
         phi=-1.0+i/1000.0
         do ii=1,2000
            psi=-1.0+ii/1000.0
            fmin=100000.0
```

```
          do iii=1,1000000
             mps1=-1.0+iii/500000.0
             mps2=-1.0+(iii+1.0)/500000.0
             if ((((ampl(tau1,tau2,gn1,gn2,phi,psi,mps1,lam).lt.0.0)
     &          .and.(ampl(tau1,tau2,gn1,gn2,phi,psi,mps2,lam).gt.0.0))
     &          .or.((ampl(tau1,tau2,gn1,gn2,phi,psi,mps1,lam).gt.0.0)
     &          .and.(ampl(tau1,tau2,gn1,gn2,phi,psi,mps2,lam).lt.0.0)))
     &           .or.(ampl(tau1,tau2,gn1,gn2,phi,psi,mps1,lam).eq.0.0))
     &    then
            inmps=mps1
            inmph=mhh(tau2,gn2,psi,inmps,lam)
            if (inmps.eq.0.0) then
               goto 100
            end if
      if (fl(tau1,tau2,gn1,gn2,phi,psi,inmph,inmps,lam).lt.fmin) then
            fmin=fl(tau1,tau2,gn1,gn2,phi,psi,inmph,inmps,lam)
            mps=inmps
            mph=inmph
         end if
      end if
100   end do
      write(1,930) fmin
      write(5,900) phi,psi,mph
      write(6,900) phi,psi,mps
    end do
    end do

    close(1)

900 format(f14.7,' ',f14.7,' ',f14.7)
910 format(f14.7,' ',f14.7,' ',f14.7,' ',f14.7,' ',f14.7)
920 format(f14.7,' ',f14.7)
930 format(f14.7)
    stop
    end
```

```
      program hex-hex-phase.f
      implicit none
c     written on 2008/11/06
c     rivised on 2008/11/10
c     adding contour on 2008/11/12
c     revised on 2008/11/21
c     adding phase shift on 2008/11/27
c     revised the energy  2008/11/29

      double precision fl,fh,fdis
      double precision ta1,ta2,g1,g2,PH,PS,mh,ms,la
      double precision tau1,tau2,gn1,gn2,phi,psi,lam,pii,pi
      double precision ampl,mhh,fmin,mps1,mps2,inmps,inmph,mps,mph
      integer i,ii,iii

      fl(ta1,ta2,g1,g2,PH,PS,mh,ms,la)
     &=ta1/2.0*(PH**(2.0))+g1/4.0*(PH**(4.0))
     &           +(ta1-1.0+3.0*g1*(PH**(2.0)))*(mh**(2.0))
     &           +5.0/2.0*g1*(mh**(4.0))
     &           +4.0/(3.0**(1.0/2.0))*g1*PH*(mh**(3.0))
     &+ta2/2.0*(PS**(2.0))+g2/4.0*(PS**(4.0))
     &           +(ta2-1.0+3.0*g2*(PS**(2.0)))*(ms**(2.0))
     &           +5.0/2.0*g2*(ms**(4.0))
     &           +4.0/(3.0**(1.0/2.0))*g2*PS*(ms**(3.0))
     &           -la*(PH*PS-mh*ms)

      ampl(ta1,ta2,g1,g2,PH,PS,ms,la)
     &=2.0*(ta1-1.0+3.0*g1*(PH**(2.0)))
     &*(-(2.0*(ta2-1.0+3.0*g2*(PS**(2.0)))*ms+10.0*g2*(ms**(3.0))
     &+4.0*(3.0**(1.0/2.0))*g2*PS*(ms**2.0))/la)
     &+10.0*g1
     &*((-(2.0*(ta2-1.0+3.0*g2*(PS**(2.0)))*ms+10.0*g2*(ms**(3.0))
     &+4.0*(3.0**(1.0/2.0))*g2*PS*(ms**2.0))/la)**(3.0))
     &+4.0*(3.0**(1.0/2.0))*g1*PH
     &*((-(2.0*(ta2-1.0+3.0*g2*(PS**(2.0)))*ms+10.0*g2*(ms**(3.0))
     &+4.0*(3.0**(1.0/2.0))*g2*PS*(ms**2.0))/la)**(2.0))
     &+la*ms

      mhh(ta2,g2,PS,ms,la)
     &=-(2.0*(ta2-1.0+3.0*g2*(PS**(2.0)))*ms+10.0*g2*(ms**(3.0))
     &+4.0*(3.0**(1.0/2.0))*g2*PS*(ms**2.0))/la

      open(1,file='hex_hex_phase_min_energy_tau08_g1_la02.dat')
      open(2,file='hex_hex_phase_msmh_tau08_g1_la02.dat')
      open(5,file='hex_hex_phase_mh_tau08_g1_la02.dat')
      open(6,file='hex_hex_phase_ms_tau08_g1_la02.dat')

      tau1=0.8
      tau2=0.8
      gn1=1.0
      gn2=1.0
      lam=0.2

      do i=1,2000
```

```
        phi=-1.0+i/1000.0
        do ii=1,2000
           psi=-1.0+ii/1000.0
           fmin=100000.0
           do iii=1,1000000
              mps1=-1.0+iii/500000.0
              mps2=-1.0+(iii+1.0)/500000.0
            if ((((ampl(tau1,tau2,gn1,gn2,phi,psi,mps1,lam).lt.0.0)
    &        .and.(ampl(tau1,tau2,gn1,gn2,phi,psi,mps2,lam).gt.0.0))
    &        .or.((ampl(tau1,tau2,gn1,gn2,phi,psi,mps1,lam).gt.0.0)
    &        .and.(ampl(tau1,tau2,gn1,gn2,phi,psi,mps2,lam).lt.0.0)))
    &         .or.(ampl(tau1,tau2,gn1,gn2,phi,psi,mps1,lam).eq.0.0))
    &       then
             inmps=mps1
             inmph=mhh(tau2,gn2,psi,inmps,lam)
             if (inmps.eq.0.0) then
                goto 100
             end if
     if (fl(tau1,tau2,gn1,gn2,phi,psi,inmph,inmps,lam)
    &.lt.fmin) then
             fmin=fl(tau1,tau2,gn1,gn2,phi,psi,inmph,inmps,lam)
             mps=inmps
             mph=inmph
          end if
       end if
100  end do
       write(1,930) fmin
       if (fmin.eq.100000.0) then
          mph=0.0
          mps=0.0
       end if
     write(5,900) phi,psi,mph
     write(6,900) phi,psi,mps
     write(2,910) phi,psi,mps,mph,mps*mph
     end do
     end do

     close(1)

900  format(f14.7,' ',f14.7,' ',f14.7)
910  format(f14.7,' ',f14.7,' ',f14.7,' ',f14.7,' ',f14.7)
920  format(f14.7,' ',f14.7)
930  format(f14.7)
     stop
     end
```

```
      program squ-squ.f
      implicit none
c     written on 2008/11/25

      double precision fl,fh,fdis
      double precision ta1,ta2,g1,g2,PH,PS,mh,ms,la
      double precision tau1,tau2,gn1,gn2,phi,psi,lam,css,cs,csr
      double precision ampl,mhh,fmin,mps1,mps2,inmps,inmph,mps,mph
      integer i,ii,iii,iiiii

      fl(ta1,ta2,g1,g2,PH,PS,mh,ms,la,cs)
     &=ta1/2.0*(PH**(2.0))+g1/4.0*(PH**(4.0))
     &           +(ta1-1.0+3.0*g1*(PH**(2.0)))*(mh**(2.0))
     &           +9.0/4.0*g1*(mh**(4.0))
     &+ta2/2.0*(PS**(2.0))+g2/4.0*(PS**(4.0))
     &           +(ta2-1.0+3.0*g2*(PS**(2.0)))*(ms**(2.0))
     &           +9.0/4.0*g2*(ms**(4.0))
     &           -la*(PH*PS+2.0*mh*ms*cs)

      ampl(ta1,ta2,g1,g2,PH,PS,ms,la,cs)
     &=2.0*(ta1-1.0+3.0*g1*(PH**(2.0)))
     &*((ta2-1.0+3.0*g2*(PS**(2.0)))*ms+9.0/2.0*g2*(ms**(3.0)))/(la*cs)
     &+9.0*g1*((
     &((ta2-1.0+3.0*g2*(PS**(2.0)))*ms+9.0/2.0*g2*(ms**(3.0)))/(la*cs)
     &)**(3.0))
     &-2.0*la*ms*cs

      mhh(ta2,g2,PS,ms,la,cs)
     &=((ta2-1.0+3.0*g2*(PS**(2.0)))*ms+9.0/2.0*g2*(ms**(3.0)))/(la*cs)

      open(1,file='squ_squ_min_energy_tau08_g1_la02.dat')
      open(2,file='squ_squ_msmhal_tau08_g1_la02.dat')
      open(5,file='squ_squ_mh_tau08_g1_la02.dat')
      open(6,file='squ_squ_ms_tau08_g1_la02.dat')
      open(12,file='test_cos_squ_squ_tau08_g1_la02.dat')

      tau1=0.8
      tau2=0.8
      gn1=1.0
      gn2=1.0
      lam=0.2

      do i=1,2000
         phi=-1.0+i/1000.0
         do ii=1,2000
            psi=-1.0+ii/1000.0
            fmin=100001.0
            do iii=1,1000000
               do iiiii=1,2
                  css=-1.0+2.0*(iiiii-1)
                  mps1=-1.0+iii/500000.0
                  mps2=-1.0+(iii+1.0)/500000.0
           if ((((ampl(tau1,tau2,gn1,gn2,phi,psi,mps1,lam,css).lt.0.0)
     &      .and.(ampl(tau1,tau2,gn1,gn2,phi,psi,mps2,lam,css).gt.0.0))
```

```
    &      .or.((ampl(tau1,tau2,gn1,gn2,phi,psi,mps1,lam,css).gt.0.0)
    &      .and.(ampl(tau1,tau2,gn1,gn2,phi,psi,mps2,lam,css).lt.0.0)))
    &       .or.(ampl(tau1,tau2,gn1,gn2,phi,psi,mps1,lam,css).eq.0.0))
    &    then
             inmps=mps1
             inmph=mhh(tau2,gn2,psi,inmps,lam,css)
             write(12,*) phi,psi,inmps,inmph,css,inmps*inmph*css,
    &fl(tau1,tau2,gn1,gn2,phi,psi,inmph,inmps,lam,css)
             if (inmps.eq.0.0) then
                goto 100
             end if
       if (fl(tau1,tau2,gn1,gn2,phi,psi,inmph,inmps,lam,css)
    &.lt.fmin) then
             fmin=fl(tau1,tau2,gn1,gn2,phi,psi,inmph,inmps,lam,css)
             mps=inmps
             mph=inmph
             csr=css
          end if
        end if
      end do
100   end do
        write(1,930) fmin
        if (fmin.eq.100001.0) then
           mph=0.0
           mps=0.0
        end if
        write(5,900) phi,psi,mph
        write(6,900) phi,psi,mps
        write(2,950) phi,psi,mps,mph,csr,mps*mph*csr
      end do
      end do

      close(1)

900   format(f14.7,' ',f14.7,' ',f14.7)
910   format(f14.7,' ',f14.7,' ',f14.7,' ',f14.7,' ',f14.7)
920   format(f14.7,' ',f14.7)
930   format(f14.7)
950   format(f14.7,' ',f14.7,' ',f14.7,' ',f14.7,' ',f14.7,' ',f14.7
    &,' ',f14.7)
      stop
      end
```

```
      program min-energy3.f
c     written on 2008/11/06
c     adding square-square, hexagonal-phaseshift on 2008/11/27
c     adding hexagonal_phaseshift2 on 2008/12/17
      implicit none

      double precision ta1,ta2,g1,g2,la,PH,PS,mh,ms,Fsd,Fhd,Fdd
      double precision tau1,tau2,gn1,gn2,lam,phi,psi,mhh,mss
      double precision strstr,hexhex,strhex,strdis,hexdis,disdis
      double precision squsqu,hexphase,hexphase2
      double precision hexstr,disstr,dishex,Fds,Fdh,l10(0:2000,0:2000)
      double precision l1,l2,l3,l4,l5,l6,l7,l8,l9,mss1,l11
      integer i,ii,tal1,tal2,tal3,tal4,tal5,tal6,tal7,tal8,tal9,tal11
      integer tal10(0:2000,0:2000),diff

      Fsd(ta1,ta2,g1,g2,PH,PS,mh,la)
     &=ta1/2.0*(PH**(2.0))+g1/4.0*(PH**(4.0))
     &           +(ta1-1.0+3.0*g1*(PH**(2.0)))*(mh**(1.0))
     &           +3.0/2.0*g1*(mh**(2.0))
     &+ta2/2.0*(PS**(2.0))+g2/4.0*(PS**(4.0))
     &           -la*PH*PS

      Fds(ta1,ta2,g1,g2,PH,PS,ms,la)
     &=ta2/2.0*(PS**(2.0))+g2/4.0*(PS**(4.0))
     &           +(ta2-1.0+3.0*g2*(PS**(2.0)))*(ms**(1.0))
     &           +3.0/2.0*g2*(ms**(2.0))
     &+ta1/2.0*(PH**(2.0))+g1/4.0*(PH**(4.0))
     &           -la*PH*PS

      Fhd(ta1,ta2,g1,g2,PH,PS,mh,la)
     &=ta1/2.0*(PH**(2.0))+g1/4.0*(PH**(4.0))
     &           +(ta1-1.0+3.0*g1*(PH**(2.0)))*(mh**(2.0))
     &           +5.0/2.0*g1*(mh**(4.0))
     &           +4.0/(3.0**(1.0/2.0))*g1*PH*(mh**(3.0))
     &+ta2/2.0*(PS**(2.0))+g2/4.0*(PS**(4.0))
     &           -la*PH*PS

      Fdh(ta1,ta2,g1,g2,PH,PS,ms,la)
     &=ta2/2.0*(PS**(2.0))+g2/4.0*(PS**(4.0))
     &           +(ta2-1.0+3.0*g2*(PS**(2.0)))*(ms**(2.0))
     &           +5.0/2.0*g2*(ms**(4.0))
     &           +4.0/(3.0**(1.0/2.0))*g2*PS*(ms**(3.0))
     &+ta1/2.0*(PH**(2.0))+g1/4.0*(PH**(4.0))
     &           -la*PH*PS

      Fdd(ta1,ta2,g1,g2,PH,PS,la)
     &=ta1/2.0*(PH**(2.0))+g1/4.0*(PH**(4.0))
     &+ta2/2.0*(PS**(2.0))+g2/4.0*(PS**(4.0))
     &-la*PH*PS

      tau1=0.8
      tau2=0.8
      gn1=1.0
      gn2=1.0
```

```
      lam=0.02

      open(1,file='str_str_min_energy_tau08_g1_la002.dat'
     &,STATUS='OLD')
      open(2,file='hex_hex_min_energy_tau08_g1_la002.dat'
     &,STATUS='OLD')
      open(3,file='str_hex_min_energy_tau08_g1_la002.dat'
     &,STATUS='OLD')
      open(7,file='hex_str_min_energy_tau08_g1_la002.dat'
     &,STATUS='OLD')
      open(10,file='squ_squ_min_energy_tau08_g1_la002.dat'
     &,STATUS='OLD')
      open(11,file='hex_hex_phase_min_energy_tau08_g1_la002.dat
     &',STATUS='OLD')
      open(12,file='hex_hex_2phase_min_energy_tau08_g1_la002.dat
     &',STATUS='OLD')
      open(4,file='phase_sort_tau08_g1_la002.dat')
      open(5,file='phase_diagram_tau08_g1_la002.dat')
      open(20,file='phase_sort_strstr_tau08_g1_la002.dat')
c      open(6,file='test.dat')
c      open(8,file='energy_tau08_g1_la002.dat')
c      open(11,file='hexdis.dat')
c      open(12,file='dishex.dat')
c      open(13,file='strdis.dat')
c      open(14,file='disstr.dat')

      do i=1,2000
         phi=-1.0+i/1000.0
         do ii=1,2000
            psi=-1.0+ii/1000.0
            read(1,*) strstr
            read(2,*) hexhex
            read(3,*) strhex
            read(7,*) hexstr
            read(10,*) squsqu
            read(11,*) hexphase
            read(12,*) hexphase2
c            hexstr=1000.0
c            write(6,900) strstr, hexhex

            if (12.0/5.0*gn1*(phi**(2.0)).lt.1.0-tau1) then
               if (phi.lt.0.0) then
                  mss=(-(3.0**(1.0/2.0))*phi
     &                 +(5.0-5.0*tau1-12.0*(phi**2.0))**(1.0/2.0))/5.0
                  hexdis=Fhd(tau1,tau2,gn1,gn2,phi,psi,mss,lam)
               else
                  mss=(-(3.0**(1.0/2.0))*phi
     &                 -(5.0-5.0*tau1-12.0*(phi**2.0))**(1.0/2.0))/5.0
                  hexdis=Fhd(tau1,tau2,gn1,gn2,phi,psi,mss,lam)
               end if
            else
               hexdis=10000.0
            end if
```

```
            if (12.0/5.0*gn2*(psi**(2.0)).lt.1.0-tau2) then
               if (psi.lt.0.0) then
                  mss1=(-(3.0**(1.0/2.0))*psi
     &                 +(5.0-5.0*tau2-12.0*(psi**2.0))**(1.0/2.0))/5.0
                  dishex=Fdh(tau1,tau2,gn1,gn2,phi,psi,mss1,lam)
               else
                  mss1=(-(3.0**(1.0/2.0))*psi
     &                 -(5.0-5.0*tau2-12.0*(psi**2.0))**(1.0/2.0))/5.0
                  dishex=Fdh(tau1,tau2,gn1,gn2,phi,psi,mss1,lam)
               end if
            else
             dishex=10004.0
            end if

            if (3.0*gn1*(phi**(2.0)).lt.1.0-tau1) then
               mhh=-(tau1-1.0+3.0*gn1*(phi**(2.0)))/(3.0*gn1)
               strdis=Fsd(tau1,tau2,gn1,gn2,phi,psi,mhh,lam)
            else
               strdis=10002.0
            end if

            if (3.0*gn2*(psi**(2.0)).lt.1.0-tau2) then
               mhh=-(tau2-1.0+3.0*gn2*(psi**(2.0)))/(3.0*gn2)
               disstr=Fds(tau1,tau2,gn1,gn2,phi,psi,mhh,lam)
            else
               disstr=10003.0
            end if

            disdis=Fdd(tau1,tau2,gn1,gn2,phi,psi,lam)

c            write(11,*) phi,psi, hexdis
c            write(12,*) phi,psi, dishex
c            write(13,*) phi,psi, strdis
c            write(14,*) phi,psi, disstr

c     sort!

            if (strstr.lt.squsqu) then
               l1=strstr
               tal1=1
            else
               l1=squsqu
               tal1=2
            end if

            if (hexhex.lt.hexphase) then
               l2=hexhex
               tal2=3
            else if (hexhex.gt.hexphase) then
               l2=hexphase
               tal2=4
            else if (hexhex.eq.hexphase) then
               l2=hexphase
               tal2=4
```

```
            end if

            if (strhex.lt.hexstr) then
               l3=strhex
               tal3=5
            else
cif (strhex.gt.hexstr) then
               l3=hexstr
               tal3=6
c            else
c               l2=hexstr
c               tal2=10
           end if

            if (strdis.lt.disstr) then
               l4=strdis
               tal4=7
            else
               l4=disstr
               tal4=8
            end if

            if (hexdis.lt.dishex) then
               l5=hexdis
               tal5=9
            else
cif (hexdis.gt.dishex) then
               l5=dishex
               tal5=10
c            else
c               l4=dishex
c               tal4=11
            end if

            if (hexphase2.lt.disdis) then
               l11=hexphase2
               tal11=12
            else
               l11=disdis
               tal11=11
            end if

            if (l5.lt.l11) then
               l6=l5
               tal6=tal5
            else
               l6=l11
               tal6=tal11
            end if

c     semifinal
            if (l1.lt.l2) then
               l7=l1
               tal7=tal1
```

```
            else
               l7=l2
               tal7=tal2
            end if

            if (l4.lt.l6) then
               l8=l4
               tal8=tal4
            else
               l8=l6
               tal8=tal6
            end if

            if (l3.lt.l8) then
               l9=l3
               tal9=tal3
            else
               l9=l8
               tal9=tal8
            end if

c     final
            if (l7.lt.l9) then
               l10(i,ii)=l7
               tal10(i,ii)=tal7
            else
               l10(i,ii)=l9
               tal10(i,ii)=tal9
            end if
         end do
      end do

      do i=1,2000
         do ii=2,2000
            diff=tal10(i,ii-1)-tal10(i,ii)
            if (diff.ne.0) then
               write(5,900) -1.0+i/1000.0, -1.0+ii/1000.0
            end if
         end do
      end do

      do ii=1,2000
         do i=2,2000
            diff=tal10(i-1,ii)-tal10(i,ii)
            if (diff.ne.0) then
               write(5,900) -1.0+i/1000.0, -1.0+ii/1000.0
            end if
         end do
      end do

      do i=1,2000,15
         do ii=2,2000,15
            write(4,*) -1.0+i/1000.0, -1.0+ii/1000.0, tal10(i,ii)
            write(8,*) -1.0+i/1000.0, -1.0+ii/1000.0, l10(i,ii)
```

```
            if (tal10(i,ii).eq.1) then
               write(20,900) -1.0+i/1000.0, -1.0+ii/1000.0
            end if
         end do
      end do

      close(1)
 900  format(f14.7,' ',f14.7)
 910  format(f14.7,' ',f14.7,' ',f14.7)
      stop
      end
```

The phase separation dynamics is simulated by solving Eqs. ((4.36, 4.37). Here the program for solving these equations numerically (modulate-modulate.f) is shown.

```
      program modulate_modulate.f
c     written on 08/11/15
c     revised on 08/11/16
c     revised on 08/11/17
c     modified on 09/3/11
c     small changes 09/6/13 (C and D)
      implicit none

      double precision phi(0:260,0:260),psi(0:260,0:260)
      double precision lapphi(0:260,0:260),lappsi(0:260,0:260)
      double precision lap2phi(0:260,0:260),lap2psi(0:260,0:260)
      double precision upot(0:260,0:260),ulappot(0:260,0:260)
      double precision lpot(0:260,0:260),llappot(0:260,0:260),psis,L2
      double precision sum(0:513,0:513),sumph,sumps,diffh,diffs,phih
      double precision fl,ph,ps,a,b,e,dh,dt,L1,lam,ph0,ps0,seed1,seed2
      double precision Dh1,Dh2,Ds1,Ds2,C,D,tau1,tau2,g1,g2,r1,r2,s1,s2
      double precision dif(0:260,0:260),qsdivqh
      integer nmax,xii,yii,x,y,t,lt,i,tt
      character(4) fnam

      fl(a,b,e)=a*e+b*(e**(3.0))

      call srand(1)

      nmax=128
      lt=1000
      lam=0.3
      ph0=0.0
      ps0=0.0
      tau1=0.8
      tau2=0.8
      g1=1.0
      g2=1.0
      dh=0.5
      dt=0.00001
      L1=1.0
      L2=1.0
      Dh1=2.0
      Dh2=2.0
      qsdivqh=3.0
      C=1.0/(qsdivqh**2.0)
      D=1.0/(qsdivqh**4.0)
      Ds1=2.0*D
      Ds2=2.0*C

c     output log
      open(9,file='calc.log')
      write(9,*) '2dimension'
      write(9,*) 'nmax=',nmax
      write(9,*) 'lt=',lt
```

```
      write(9,*) 'lam=',lam
      write(9,*) 'ph0=',ph0
      write(9,*) 'ps0=',ps0
      write(9,*) 'tau1=',tau1
      write(9,*) 'tau2=',tau2
      write(9,*) 'g1=',g1
      write(9,*) 'g2=',g2
      write(9,*) 'dh=',dh
      write(9,*) 'dt=',dt
      write(9,*) 'L1=',L1
      write(9,*) 'L2=',L2
      write(9,*) 'alh=',Dh1
      write(9,*) 'beh=',Dh2
      write(9,*) 'qhc=',(Dh2/(2.0*Dh1))**(1.0/2.0)
      write(9,*) 'C=',C
      write(9,*) 'D=',D
      write(9,*) 'qsc=',(Ds2/(2.0*Ds1))**(1.0/2.0)
      write(9,*) '1 output for 200000 steps '
c     initial condition

      call RANDOM_SEED()

      sumph=0.0
      sumps=0.0
      open(1,file='1000_up.data')
      do x=2,nmax+1
         do y=2,nmax+1
            call RANDOM_NUMBER(seed1)
            phi(x,y)=ph0+(seed1-0.5)*0.05
            sumph=sumph+phi(x,y)
         end do
      end do
      diffh=sumph/(nmax*nmax)-ph0
      do x=2,nmax+1
         do y=2,nmax+1
            phih=phi(x,y)
            phi(x,y)=phih-diffh
            write(1,900) phi(x,y)
         end do
      end do

      call RANDOM_SEED()

      open(2,file='1000_lw.data')
      open(3,file='1000_sum.data')
      open(4,file='1000_dif.data')
      do x=2,nmax+1
         do y=2,nmax+1
           call RANDOM_NUMBER(seed2)
           psi(x,y)=ps0+(seed2-0.5)*0.05
           sumps=sumps+psi(x,y)
         end do
      end do
      diffs=sumps/(nmax*nmax)-ps0
```

```
      do x=2,nmax+1
         do y=2,nmax+1
            psis=psi(x,y)
            psi(x,y)=psis-diffs
            write(2,900) psi(x,y)
            write(3,900) phi(x,y)+psi(x,y)
            write(4,900) phi(x,y)-psi(x,y)
         end do
      end do

c     time evolution

      do t=1,lt
         write(fnam,'(i4.4)') 1000+t
         open(1,file=fnam//'_up.data')
         open(2,file=fnam//'_lw.data')
         open(3,file=fnam//'_sum.data')
         open(4,file=fnam//'_dif.data')
         do tt=1,200000
c     potential calculation
            call bndry(phi,nmax)
            call lap(phi,lapphi,nmax)
            call bndry(lapphi,nmax)
            call lap2(phi,lap2phi,nmax)
            call bndry(lap2phi,nmax)
            call bndry(psi,nmax)
            call lap(psi,lappsi,nmax)
            call bndry(lappsi,nmax)
            call lap2(psi,lap2psi,nmax)
            call bndry(lap2psi,nmax)
            do x=2,nmax+1
               do y=2,nmax+1
                  ph=phi(x,y)
                  ps=psi(x,y)
             upot(x,y)=2.0*Dh1*lap2phi(x,y)/(dh*dh*dh*dh)
     &                +2.0*Dh2*lapphi(x,y)/(dh*dh)
     &                +fl(tau1,g1,ph)-lam*ps

             lpot(x,y)=2.0*Ds1*lap2psi(x,y)/(dh*dh*dh*dh)
     &                +2.0*Ds2*lappsi(x,y)/(dh*dh)
     &                +fl(tau2,g2,ps)-lam*ph
               end do
            end do

c     time evolution
            call bndry(upot,nmax)
            call lap(upot,ulappot,nmax)
            call bndry(ulappot,nmax)
            call bndry(lpot,nmax)
            call lap(lpot,llappot,nmax)
            call bndry(llappot,nmax)
            do x=2,nmax+1
               do y=2,nmax+1
                  ph=phi(x,y)
```

```
                  ps=psi(x,y)
                  phi(x,y)=ph+L1*dt/(dh*dh)*ulappot(x,y)
                  psi(x,y)=ps+L2*dt/(dh*dh)*llappot(x,y)
                  sum(x,y)=phi(x,y)+psi(x,y)
                  dif(x,y)=phi(x,y)-psi(x,y)
               end do
            end do
         end do

c     make data file
         do xii=2,nmax+1
            do yii=2,nmax+1
               write(1,900) phi(xii,yii)
               write(2,900) psi(xii,yii)
               write(3,900) sum(xii,yii)
               write(4,900) dif(xii,yii)
            end do
         end do

      end do

      close(1)
 900  format(f14.10)
      stop
      end
c----------------------------------------------
c     boundary condition

      subroutine bndry(p,nmax)
      double precision p(0:260,0:260)
      integer ii

      do ii=2,nmax+1
         p(     1,     ii)=p(nmax+1,    ii)
         p(nmax+2,     ii)=p(     2,    ii)
         p(    ii,      1)=p(    ii,nmax+1)
         p(    ii, nmax+2)=p(    ii,     2)
         p(     0,     ii)=p(  nmax,    ii)
         p(nmax+3,     ii)=p(     3,    ii)
         p(    ii,      0)=p(    ii,  nmax)
         p(    ii, nmax+3)=p(    ii,     3)
      end do
      p(     1,     1)=p(nmax+1,nmax+1)
      p(     1,nmax+2)=p(nmax+1,     2)
      p(nmax+2,     1)=p(     2,nmax+1)
      p(nmax+2,nmax+2)=p(     2,     2)

      return
      end
c----------------------------------------------
c     isotropized laplacian

      subroutine lap(p,dd,nmax)
      double precision p(0:260,0:260),dd(0:260,0:260)
```

```
      integer xi,yi

      do xi=2,nmax+1
         do yi=2,nmax+1
            dd(xi,yi)=p(xi+1,yi)+p(xi-1,yi)+p(xi,yi+1)+p(xi,yi-1)
     &        -4.0*p(xi,yi)
c     &       +(p(xi+1,yi+1)+p(xi-1,yi-1)+p(xi-1,yi+1)+p(xi+1,yi-1))/4.0

         end do
      end do

      return
      end
c-----------------------------------------------
c     laplacian^2

      subroutine lap2(p,dd,nmax)
      double precision p(0:260,0:260),dd(0:260,0:260)
      integer xi,yi

      do xi=2,nmax+1
         do yi=2,nmax+1
            dd(xi,yi)=p(xi+2,yi)+p(xi-2,yi)+p(xi,yi+2)+p(xi,yi-2)
     &             -(p(xi+1,yi)+p(xi-1,yi)+p(xi,yi+1)+p(xi,yi-1))*8.0
     &     +((p(xi+1,yi+1)+p(xi-1,yi-1)+p(xi-1,yi+1)+p(xi+1,yi-1)))*2.0
     &     +20.0*p(xi,yi)
         end do
      end do

      return
      end
```

References

[1] *Micelles, Membranes, Microemulsions, and Monolayers*, (Eds. W.Gelbart, D.Roux, A.Ben Shaul), Springer, NY, 1994.

[2] A-S. Smith, *Nature Physics* **2010**, *6*, 726-729.

[3] S. J. Singer and G. L. Nicolson, *Science* **1972**, *175*, 720-731

[4] K. Simons and E. Ikonen, *Nature* **1997**, *387*, 569-572.

[5] D. A. Brown and J. K. Rose, *Cell* **1992**, *68*, 533-544.

[6] I. A. Prior, C. Muncke, P. G. Parton and J. F. Hancock, *J. Cell Biol.* **2003**, *160*, 165-170.

[7] A. Fujita, J. Cheng, M. Hirakawa, K. Furukawa, S. Kusunoki and T. Fujimoto, *Mol. Biol. Cell* **2007**, *18*, 2112-2122.

[8] P. Sharma, R. Varma, R. C. Sarasij, Ira, K. Gousset, G. Krishnamoorthy, M. Rao, S. Mayor, *Cell* **2004**, *116*, 577-589.

[9] K. Jacobson, O. G. Mouritsen and R. G. W. Anderson, *Nat. Cell. Biol.* **2007**, *9*, 7-14.

[10] A. Kusumi, I. Koyama-Honda and K. Suzuki, *Traffic* **2004**, *5*, 213.

[11] C. Eggeling, C. Ringemann, R. Medda, G. Schwarzmann, K. Sandhoff, S. Polyakova, V. N. Belov, B. Hein, C. v. Middendorff, A. Schönle and S. W. Hell, *Nature* **2009**, *457*, 1159-1163.

[12] G. van Meer, *Embo J.* **2005**, *24*, 3159-3165.

[13] C. Dietrich, L. A. Bagatolli, Z. N. Volovyk, N. L. Thompson, M. Levi, K. Jacobson and E. Gratton, *Biophys. J.* **2001**, *80*, 1417-1428.

[14] S. L. Veatch and S. L. Keller, *Phys. Rev. Lett.* **2002**, *89*, 268101.

[15] S. L. Veatch and S. L. Keller, *Biophys. J.* **2003**, *85*, 3074-3082.

[16] R. F. M. de Almeida, A. Fedorov and M. Prieto, *Biophys. J.* **2003**, *85*, 2406-2416.

[17] S. L. Veatch and S. L. Keller, *Phys. Rev. Lett.* **2005**, *94*, 148101.

[18] S. Komura, H. Shirotori, P. Olmsted and D. Andelman, *Europhys. Lett.* **2004**, *67*, 321-327.

[19] R. Elliott, I. Szleifer and M. Schick, *Phys. Rev. Lett.* **2006**, *96*, 098101.

[20] H. J. Risselada and S. J. Marrink, *Proc. Natl. Acad. Sci. USA* **2008**, *105*, 17367-17372.

[21] T. Baumgart, S. T. Hess, and W. W. Webb, *Nature* **2003**, *425*, 821-824.

[22] S. Rozovsky, Y. Kaizuka, and J. T. Groves, *J. Am. Chem. Soc.* **2005**, *127*, 36-37.

[23] S. Komura, N, Shimokawa and D. Andelman, *Langmuir* **2006**, *21*, 6771-6774.

[24] Y. Kaizuka and J. T. Groves, *New J. Phys.* **2010**, *12*, 095001.

[25] A. R. Honerkamp-Smith, S. L. Veatch and S. L. Keller, *Biochim. Biophys. Acta - Biomembranes* **2009**, *1788*, 53-63.

[26] S. L. Veatch, O. Soubias, S. L. Keller and K. Gawrisch, *Proc. Natl. Acad. Sci. USA* **2007**, *104*, 17650-17655.

[27] A. R. Honerkamp-Smith, P. Cicuta, M. D. Collins, S. L. Veatch, M. den Nijs, M. Schick and S. L. Keller, *Biophys. J.* **2008**, *95*, 236-246.

[28] S. L. Veatch, P. Cicuta, P. Sengupta, A. R. Honerkamp-Smith, D. Holowka and B. Baird, *ACS Chem. Bio.* **2008**, *3*, 287-293.

[29] R. Brewster, P. A. Pincus and S. A. Safran, *Biophys. J.* **2009**, *97*, 1087-1094.

[30] R. Brewster and S. A. Safran, *Biophys. J.* **2010**, *98*, L21-L23.

[31] T. Yamamoto, R. Brewster and S. A. Safran, *Europhys. Lett.* **2010**, *91*, 28002.

[32] G. Van Meer, D. Voelker and G. Feigenson, *Nat. Rev. Mol. Cell. Biol.* **2008**, *112*, 112.

[33] L. L. M. Van Deenen, *Pure. Appl. Chem.* **1971**, *25*, 25.

[34] K. Simons and W. L. C. Vas, *Ann. Rev. Biophys. Biomol. Struct.* **2004**, *33*, 269-295.

[35] A. Zachowski, *Biochem. J.* **1993**, *294*, 1-14.

[36] M. D. Collins and S. L. Keller, *Proc. Natl. Acad. Sci. USA* **2008**, *105*, 124-128.

[37] S. May, *Soft Matter* **2009**, *5*, 3148-3156.

[38] A. J. Wagner, S. Loew, and S. May, *Biophys. J.* **2007** *93*, 4268-4277.

[39] G. G. Putzel and M. Schick, *Biophys. J.* **2008**, *94*, 869-877.

[40] M. Ouarch, M. Benhamou, M. Chahid and H. Kaidi, *Eur. Phys. J. E* **2009**, *29*, 319-327.

[41] T. Garel and S. Doniach, *Phys. Rev. B* **1982**, *26*, 325-329.

[42] D. Andelman, F. Brochard, and J.-F. Joanny, *J. Chem. Phys.* **1987**, *86*, 3673-3681.

[43] S. Leibler and D. Andelman, *J. Phys.* (*France*) **1987**, *48*, 2013-2018.

[44] L. Leibler, *Macromolecules* **1980**, *13*, 1602-1617.

[45] I. W. Hamley, *The Physics of Block Copolymers*, Oxford University, Oxford, **1998**.

[46] M. Teubner and R. Strey, *J. Chem. Phys.* **1987**, *87*, 3195-3200.

[47] G. Gompper and M. Schick, *Phys. Rev. B* **1990**, *41*, 9148-9162.

[48] K. Chen, C. Jayaprakash, R. Pandit and W. Wenzel, *Phys. Rev. Lett.* **1990**, *65*, 2736-2739.

[49] R. Holyst and M. Schick, *J. Chem. Phys.* **1992**, *96*, 7728-7737.

[50] K. Yamada and S. Komura, *J. Phys.: Condens. Matter* **2008**, *20*, 155107.

[51] P. C. Hohenberg and B. I. Halperin, *Rev. Mod. Phys.* **1977**, *49*, 435-479.

[52] C. Tang, E. M. Lennon, G. H. Fredrickson, E. J. Kramer, and C. J. Hawker, *Science* **2008**, *322*, 429-432.

[53] Hao Wu and Z. C. Tu, *J. Chem. Phys.* **2009**, *130*, 045103.

[54] L. Yang, M. Dolnik, A. M. Zhabotinsky, and I. R. Epstein, *Phys. Rev. Lett.* **2002**, *88*, 208303.

[55] J. Israelachvili, *Langmuir* **1994**, *10*, 3774-3781.

[56] P. W. Tumaneng, S. A. Pandit, G. Zhao and H. L. Scott, arXiv:1008.5142.

[57] P. G. Barton and F. D. Gunstone, *J. Biol. Chem.* **1975**, *250*, 4470-4476.

[58] S. Trabelsi, S. Zhang, T. R. Lee and D. K. Schwartz, *Phys. Rev. Lett.* **2008**, *100*, 037802.

[59] P. Pieruschka and A. A. Safran, *Europhys. Lett.* **1993**, *22*, 625-630.

[60] M. Hennes and G. Gompper, *Phys. Rev. E* **1996**, *54*, 3811-3831.

[61] M. Nonomura and T. Ohta, *J. Chem. Phys.* **1999**, *110*, 7516-7523.

[62] A. G. Zilman and R. Granek, *Phys. Rev. Lett.* **1996**, *77*, 4788-4791.

[63] E. Freyssingeas, D. Roux and F. Nallet, *J. Phys. II.* **1997**, *7*, 913-929.

[64] M. S. Turner, P. Sens and N. D. Socci, *Phys. Rev. Lett.* **2005**, *95*, 168301.

[65] L. Foret, *Europhys. Lett.* **2005**, *71*, 508-514.

[66] J. Fun, M. Sammalkorpi and M. Haataja, *Phys. Rev. Lett.* **2008**, *100*, 178102.

[67] J. Fun, M. Sammalkorpi and M. Haataja, *Phys. Rev. Lett.* **2010**, *104*, 118101.

[68] Z. Zhang, M. J. Zuckermann and O. G. Mouritsen, *Phys. Rev. A.* **1992**, *46*, 6707-6713.

[69] P. M. Chaikin and T. C. Lubensky, *Principles of Condensed Matter Physics*, Cambridge University, Cambridge, **1995**.

[70] M. Nakano, M. Fukuda, T. Kudo, H. Endo and T. Handa, *Phys. Rev. Lett.* **2007**, *98*, 238101.

[71] D. L. Daleke, *J. Bio. Chem.* **2007**, *282*, 821-825.

[72] L. McEvoy, P. Williamson and R. A. Schlegel, *Proc. Natl. Acad. Sci. USA* **1986**, *83*, 3311-3315.

List of Publications

1. S. Komura, Y. Hirose and Y. Nonomura, "Adsorption of Colloidal Particles to Curved Interfaces", *J. Chem. Phys.* **2006**, *124*, 241104.
2. Y. Hirose, S. Komura and Y. Nonomura, "Adsorption of Janus Particles to Curved Interfaces", *J. Chem. Phys.* **2007**, *127*, 054707.
3. Y. Hirose, S. Komura and T. Kato, "Adsorption Dynamics in Pickering Emulsions", *Prog. Theor. Phys.* **2008**, *175*, 81.
4. Y. Hirose, S. Komura and D. Andelman "Coupled Modulated Bilayers: A Phenomenological Model", *ChemPhysChem* **2009**, *10*, 2839.

Acknowledgments

My deepest gratitude for accomplishing the study is dedicated to Professor Shigeyuki Komura. I am grateful for his warmest and coolest advice, I am indebted to him for everything that I learnt during my stay at TMU.

I greatly appreciate the support given by Professor Tadashi Kato for his critical suggestions and kindest support. I would like to thank Professor David Andelman for his kind hospitality and warm support both in academics and otherwise. I am grateful to Professor Kenro Hashimoto and Professor Haruo Shiromaru for careful reading of this thesis and useful suggestions. I am also grateful to Dr. Youhei Kawabata, Dr. Kohtaro Yamada, and Dr. Sanoop Ramachandran for fruitful comments and warm encouragements. I would like to thank all the members of the laboratory of physical chemistry of molecular assembly for the support through the days.

Finally, I would like to thank my family. Without their supports, this study would have never accomplished.